Non-isotropic distributions of stellar rotational velocities

MARTÍN SOLAR

Supervisor: Dr. Michel Curé

Co-supervisor: Dr. Catalina Arcos

Instituto de Física y Astronomía

Facultad de Ciencias

Universidad de Valparaíso

Magíster en Astrofísica

March 2021

Valparaíso. Chile.

Look again at that dot. That's here. That's home. That's us. On it, everyone you love, everyone you know, everyone you ever heard of, every human being who ever was, lived out their lives. The aggregate of our joy and suffering, thousands of confident religions, ideologies, and economic doctrines, every hunter and forager, every hero and coward, every creator and destroyer of civilization, every king and peasant, every young couple in love, every mother and father, hopeful child, inventor and explorer, every teacher of morals, every corrupt politician, every "superstar," every "supreme leader," every saint and sinner in the history of our species lived there–on a mote of dust suspended in a sunbeam.

(...)

Pale Blue Dot - Carl Sagan (1934 - 1996)

This thesis is solely my own composition,
except where specifically indicated in the text.

Martín Solar
March 2021.
Valparaíso. Chile.

Acknowledgments

I want to start by thanking Prof. Dr. Michel Curé, who was the main motivation to carry out this thesis. His determination for science, infinite tolerance and great sense of humor are things that have inspired me to continue my studies in astrophysics. I also acknowledge Prof. Dr. Catalina Arcos for her thoughtful and pleasant way of teaching. A special mention to the group of massive stars of the IFA-UV, in which they gave me constant feedback on my work and I learned a lot from their different investigations.

A particular distinction is for the academic and administrative body of the IFA-UV that without knowing all of them I realized that it is vital to create a pleasant and friendly work environment for the day to day. Another very important thanks is to the postdocs and graduate students of this institute, especially to my fellow Masters: Ramsés, Erick, Catalina, Daniela, Santiago and Greco. I also want to refer to my office colleagues who endured all my eccentricities during work hours.

This work is dedicated to my dear family and friends who have been with me throughout the years.

This thesis is funding from the European Union's Framework Programme for Research and Innovation Horizon 2020 (2019-2021) under the Marie Sklodowska-Curie grant Agreement No. 823734.

Abstract

Stellar rotation is defined from the angular motion of a star about its own rotational axis and study this phenomenon is useful to constrain models of stellar formation and evolution. The equatorial velocity v is defined as the surface angular speed at latitude 0^o, however, the projected rotational velocity $v \sin i$ value is one of the most straightforward and cheapest (from an observational point of view) ways to obtain the rotational velocity of a star, where i is the inclination angle between the axis of rotation with respect to the observer. This research is separated in two parts; obtain this $v \sin i$ value via Fourier Transform in an automated procedure and apply a non-isotropic distribution model for the axes on the unit sphere of observation:

1) Obtaining $v \sin i$: There are several methods to infer $v \sin i$ data, in the case of Fourier Transform, this method consists in obtain the first zero of the Fourier Transform domain from a rotational kernel for the observed absorption line profile. First, an automated procedure to obtain $v \sin i$ via Fourier Transform is constructed, for multiple absorption lines at different epochs. The method consists in fit a Gaussian profile to the respective line and select the signal from the curve. Monte Carlo simulations are performed where theoretical lines are constructed for specific rotational velocities. Then, the noise is added and multiple repetitions are computed to analyze the consistence of the method. Later, our automatized Fourier Transform method is used in the BeSOS database to obtain their $v \sin i$ values. Results are in global agreement with the literature.

2) How is distributed $v \sin i$: An integral equation that governs the two distributions v and $v \sin i$ (true and apparent rotational speed distributions respectively) is given by a Fredholm integral in which an α parameter is added into the kernel of the equation to model a non-isotropic distribution, where $\alpha < 0$ yields inclination angles close to the polar axis, $\alpha > 0$ a non-isotropic near to the equator and $\alpha = 0$ is the typical isotropic axes distribution. The true distribution is calculated via Tikhonov regularization method from the observed distribution which is estimated by a kernel density estimator. As α parameter is unknown, we made a grid of α to compute the

Fredholm integral. To obtain the best α value, we minimized the mean square error of the projected kernel density estimator distribution with respect to the new grid of solutions for the Fredholm integral equation. The Monte Carlo random sampling repetitions ensures that the method, in general terms, is reliable until $\alpha \sim 1$. The procedure is applied to several open stellar clusters and field stars to see the behavior of the non-isotropy finding effectively that the different databases of stars are not isotropic rotating with respect to Earth.

In summary, we have developed two novel methods; measures the $v \sin i$ values from any stellar spectrum for multiple absorption lines at different epochs where the line is broadening mainly by rotation (high rotators); the second, obtains the non-isotropy from a sample of $v \sin i$ data without any convergence criteria. As future works we want to implement this last method to binary systems (star-star or exoplanet-star) discovered by transit and also an extra parameter β can be introduced into the Fredholm integral to compute more complex distribution of axes.

Contents

List of Figures

List of Tables

CHAPTER 1

Introduction

Rotation is present in all celestial bodies, e.g., asteroids, satellites, planets, and stars, and also in astronomical objects, e.g., planetary systems, star clusters, nebulae, and galaxies. In stars, the rotation is defined from the angular motion about its own rotational axis and stars take birth in the core of a molecular cloud from the infall of spinning matter driven by self-gravity. Stellar rotation can vary in time, being fast or slow, but persist along all stellar life. Because of stars are not solid bodies, regions at different latitude rotate at different scales and rates. The shape and magnitude of rotation impact the evolution of fast rotating stars, since it is known that they present changes during their lifetime, in the evolutionary tracks of the Hertzsprung-Russell diagram, surface abundances, etc, in comparison with the non-rotating ones, as equatorial rotational velocity $v = 0$ (Maeder & Meynet, 2010). To construct a model for rotating stars, Huang (2004) assures that two effects must be taken into account: the centrifugal force and the meridian circulation. There is an enigmatic type of stars, called Be stars, discovered by Secchi (1866) and firstly defined as non-supergiant B stars that posses a spectrum that has or had at some time, one or more Balmer lines in emission (Collins, 1987) and these stars are among the fastest rotators in main sequence (Zorec et al., 2016). Porter & Rivinius (2003) defined the broader astrophysical context in Be stars, as they rotate closest to their critical speed limit, among others. There are several works about this type of stars and for a general review visit Rivinius et al. (2013).

The equatorial rotational velocity v is defined as the surface angular speed at latitude 0^o, however, observations only brings their projected $v \sin i$ value, where i is the inclination angle between the axis of rotation with respect to the observer/line of sight. Fig. 1.1 shows this simplified geometry.

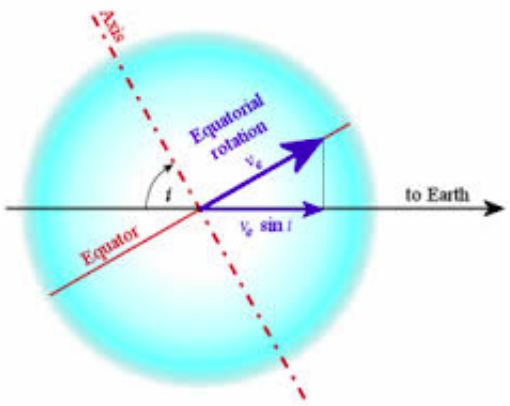

Figure 1.1: Geometrical point of view of an observer with respect to the axis of stellar rotation, denominated $v \sin i$, where v is the equatorial rotational velocity ($v_{eq} \equiv v$ for our notation) and i is the angle between the axis of rotation and the line of sight. *Credit*: Wikipedia (`https://en.wikipedia.org/wiki/Stellar_rotation`).

There are several methods to measure this $v \sin i$ value but mainly two spectroscopic techniques are used in fast rotators: models of stellar atmosphere (e.g. Kurucz, 1993; Hubeny & Lanz, 1995) and Fourier Transform (FT) technique (Carroll, 1933; Carroll & Ingram, 1933). In general terms, the first consists in using Local Thermodynamic Equilibrium (LTE) or Non-Local Thermodynamic Equilibrium (non-LTE), plane-parallel, hydrostatic model atmosphere for a grid of metallicities, effective temperatures and gravities. The standard process is the following: stellar parameters extracted from, e.g., Vizier[1] (Ochsenbein et al., 2000), are introduced into these stellar atmospheres models to create a synthetic spectrum that reproduce the observations in a wavelength region of interest for an arbitrary stellar rotation and an arbitrary instrumental profile, and the absorption line profile it is convolve with rotation (in our case HeI lines) to find the best fit between theoretical and observational spectrum. The FT method used in this thesis, lies in obtaining the first zero (Carroll, 1933; Carroll & Ingram, 1933) of the FT domain from a rotational kernel. This powerful mathematical tool is used in several works (Ilin & Ivanov, 1979; Jankov, 1995; Reiners & Schmitt, 2002; Reiners, 2003; Royer, 2005; Simón-Díaz et al., 2006; Simón-Díaz & Herrero, 2007;

[1] `https://vizier.u-strasbg.fr/`

Díaz et al., 2011; Ramírez-Agudelo et al., 2013; Simón-Díaz & Herrero, 2014). For a general review visit Gray (2005).

If we only have access to $v \sin i$ data, which is the value of v? To answer this inquiry it is necessary to know the value of the inclination angle i, which is not trivial to measure (e.g., one way is through interferometry technique, Domiciano de Souza et al., 2004; Meilland et al., 2012; Cochetti et al., 2019). Because of interferometric observations are competitive and expensives, and only offers a single target, we are motivated to look for other methods to obtain the inclination angle such as telescopes equipped with high-resolution spectrograph which are more common. An interpretation of the point of view for an observer is represented in Fig. 1.2 and Fig. 1.3 for a stellar cluster as well as field stars, respectively.

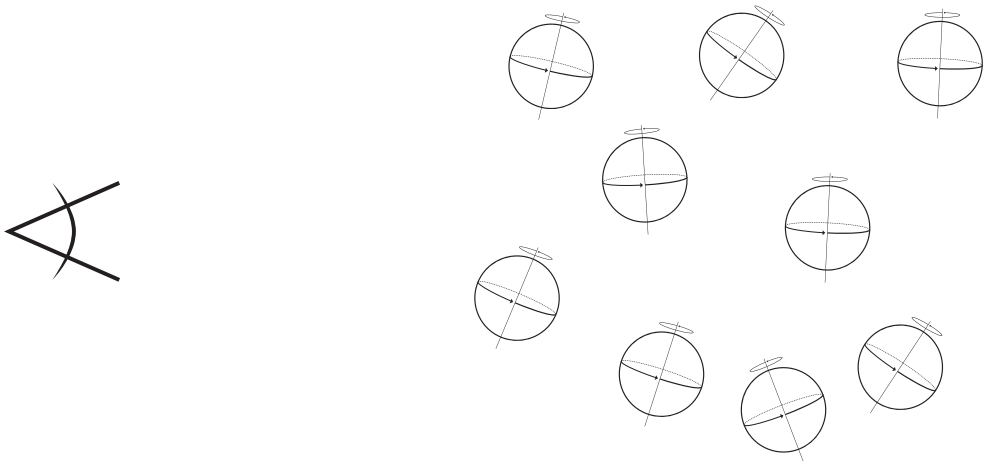

Figure 1.2: Observer point of view for a stellar cluster (small length sample example). The distribution of axes are non-isotropic with a tendency of a spin alignment.

To relate the distributions of $v \sin i$ and v, the definitions of probability density function (PDF) and cumulative density function (CDF) are reviewed.

The PDF is the density of a continuous random variable x, whose value at any given point in the sample space can be interpreted as providing a relative likelihood that the value of the random variable would equal that sample and the CDF is the probability that the variable x takes a value less than or equal to an evaluated value. These two functions are the most important statistical functions in statistics. They also are very closely related and almost any other reliability measure of interest can be

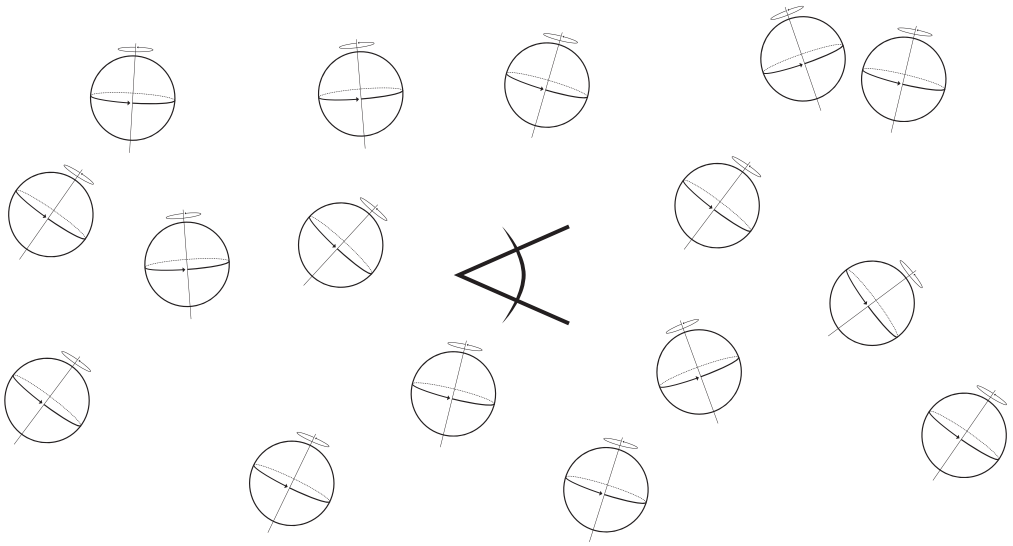

Figure 1.3: Observer point of view for field stars (small length sample example). The distribution of axes are isotropic.

derived or obtained from these ones. Fig. 1.4 shows a representation of a Gaussian (or Normal) PDF and CDF for a mean of $\mu = 5$ and a standard deviation of $\sigma = 2$.

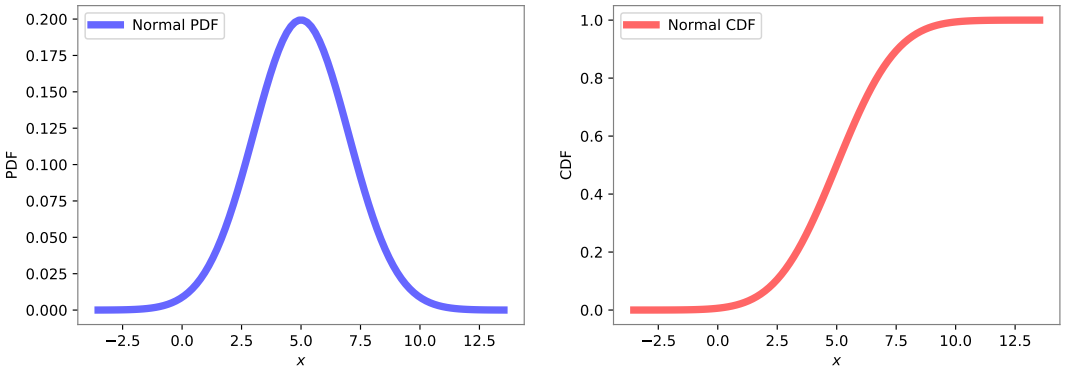

Figure 1.4: Probability density function (left panel) and cumulative density function (right function) of a Normal distribution with mean $\mu = 5$ and standard deviation of $\sigma = 2$.

The first work relating the distribution of $v \sin i$ (apparent) and v (true) was performed by Chandrasekhar & Münch (1950), where they proposed a Fredholm integral equation assuming that the inclination axes for the rotating stars are uniformly distributed over the sphere of observation. They found a method to disentangle the

true rotational velocity distribution, however, this formal solution is proportional to a differentiation of an Abel's integral, and unless the sample is of very high precision, this formal solution can lead to mislead results due to intrinsic numerical problems. Alternative to this, the Lucy-Richardson's method (Richardson, 1972; Lucy, 1974) is a Bayesian iterative routine that deconvolve a distribution function assuming a prescribed formula for the kernel of the Fredholm integral equation. Despite this method is used widely by the astronomy community, the difficulty is that there is no convergence criteria to maximize the sum of the likelihood of fitting (Bi & Boerner, 1994). Curé et al. (2014), instead of deconvolve via Lucy-Richardson's method, developed a new analytical solution to deconvolve this inverse problem in one step, being a robust method, which provides the CDF of the true rotational velocities without numerical instabilities due to the differentiation. This is also known as an "inverse problem" because of it can be accessed to the apparent rotational velocity distribution but not to the true rotational velocity distribution directly and it is an ill-posed problem.

Regularization techniques are methods that estimate the distribution of interest from the distribution of observation, in this case v from $v \sin i$. Among these methods we find: truncated singular value decomposition, selective singular value decomposition, maximum entropy and the Tikhonov regularization method (Tikhonov, 1943; Tikhonov, 1963; Tikhonov & Arsenin, 1977; Tikhonov & Goncharsky, 1987; Tikhonov et al., 1998; Hansen, 2010). For the last one, Christen et al. (2016) obtained the PDF from the Fredholm integral equation for rotating stars assuming an uniform distribution of stellar axes. The deconvolution via Tikhonov regularization method uses a regularization parameter (or Tikhonov factor) where Christen et al. (2016) developed by an iterative method with a simple criterion convergence, described in chapter 3.3. A different approach to estimate the true rotational velocity PDF is based on the maximum likelihood method, where the PDF is expressed as a sum of known distribution families (Orellana et al., 2019).

Another particular way to obtain the inclination angles is via asteroseismology techniques in red giant stars (Ballot et al., 2006; Beck et al., 2012; Huber et al., 2013; Benomar et al., 2015). Details of the mechanism are explained by Corsaro et al. (2017) and references therein, here, we show the results obtained in Fig. 1.5 for the stellar projected inclination angles for NGC 6791 (25 stars) and NGC 6819 (23 stars). The upper panel **a** of this figure represents the inclination angle ($\theta \equiv i$) of a cluster with respect to the observer. It can be appreciated that this spin forms a cone for all the values of $i = 0^o$ to $i = 90^o$. In panel **b**, the histogram shows the inclination angles

obtained for 25 stars in NGC 6791, where the global properties are: total mass of $\sim$ 5000 $(M_\odot)$, a distance modulus of $\sim$ 13.11 ± 0.06 $(m-M)_0$, size of $\sim$ 10 (pc) and with an age of 8.3 (Gyr). The orange histogram is the theoretical distribution if the inclination axes were distributed isotropically over the sphere. Same for panel **c**, but in NGC 6819 (23 stars), where the global properties are: total mass of $\sim$ 2600 $(M_\odot)$, a distance modulus of $\sim 11.85 \pm 0.05$ $(m-M)_0$, size of ~ 7 (pc) and an age of 2.4 (Gyr). In this plot it is proven that the inclination angles are not coming from an isotropical distribution of axes with respect to the observer, in NGC 6791 all the inclination angles obtained are below to 50^o and for NGC 6819 there is a bimodal distribution of angles being the first one between 0^o and 40^o, and the second one between 60^o and 80^o with a significant lower probability.

In this thesis, we propose to add an extra parameter to the Fredholm integral equation proposed by Chandrasekhar & Münch (1950) in order to model a non-isotropic distribution of axes for rotating stars.

This model was first proposed by Zorec et al. (2016) where they deconvolved the $v \sin i$ data for a list of Be stars. We reproduced this investigation and extended to other observations thanks to the Tikhonov regularization method with an iterative procedure to obtain the Tikhonov factor, proposed by Christen et al. (2016). We also add this new parameter to the one-step solution from Curé et al. (2014) to obtain the CDF for a non-isotropic distribution of axes.

Each chapter of this thesis consists in two segments; how to derive the value $v \sin i$ and how is distributed the rotational speeds from a sample of $v \sin i$. The structure is as follows:

- Chapter 2 (Mathematical foundations) $\rightarrow$ How to obtain $v \sin i$: we describe the stellar rotation mechanism and how to derive the velocity via FT method. How is distributed v: is explained the mathematics to find the best non-isotropic distribution of stellar axes for a database of rotating speeds using the Fredholm integral equation.

- Chapter 3 (Numerical procedures) $\rightarrow$ How to obtain $v \sin i$: an automated code is developed to obtain the $v \sin i$ values for multiple lines at different epochs. How is distributed v: a discretization for the continuum functions is performed to compute a Kernel Density Estimator (KDE) from a sample of the projected rotational velocities. A deconvolution via Tikhonov regularization is nextly calculated to therefore solve the Fredholm integral equation. This new solution is

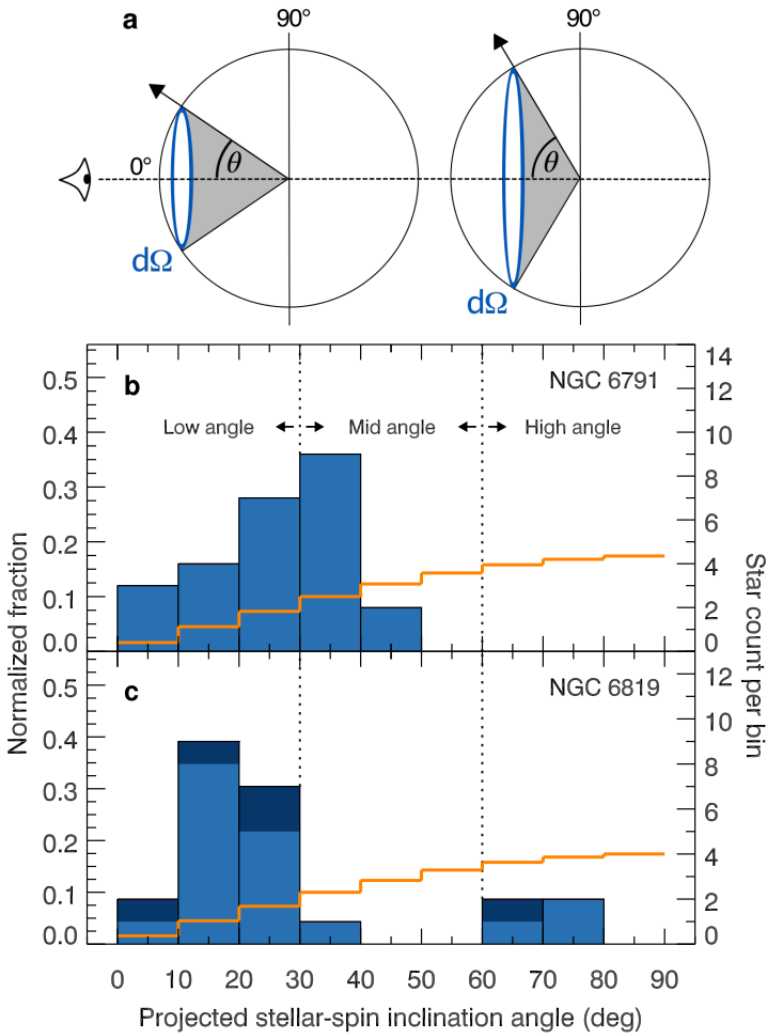

Figure 1.5: Projected stellar-spin inclinations of 48 red giants in NGC 6791 and NGC 6819. **a)**, the spin vector of the star (arrow) as seen from the line of sight can be oriented along any directions of a cone (gray shaded), with an inclination angle from $\theta = 0^o$ (pole-on) to $\theta = 90^o$ (edge-on). The infinitesimal solid angle $d\Omega$ (blue coronal shell) increases with θ. **b)**, the orange histogram shows the expected distribution for a three-dimensional uniform orientation of the spin vectors. The vertical dotted lines separate the three main configurations of stellar inclination. **c)**, same as panel **b** but for NGC 6819. The darker regions correspond to red giants that are confirmed spectroscopic single-lined binaries. *Credit*: figure and description from Corsaro et al. (2017).

compared with respect to the KDE calculating the mean square error (MSE). The result yields the best non-isotropic distribution of axes for the sample of rotating stars.

- Chapter 4 (Monte Carlo simulations) → How to obtain $v \sin i$: random sampling repetitions are done to analyze the behavior of the method to obtain $v \sin i$. How is distributed v: the numerical simulations are computed to evaluate the consistence of the method for three different samples of true rotational velocities for a grid of non-isotropic axes distribution.

- Chapter 5 (Results) → How to obtain $v \sin i$: the procedure is applied to Be Stars Observation Survey (BeSOS[2]) spectra, with results in global agreement with the literature. How is distributed v: the non-isotropic method is applied to field stars and an open clusters samples.

- Chapter 6 (Discussion) → we discuss our results and potential future works.

- Chapter 7 (Conclusion) → we conclude the final remarks of the research.

[2] http://besos.ifa.uv.cl/

CHAPTER 2

Mathematical foundations

As it was mentioned in the Introduction (Chapter 1), this Chapter is separated in two parts, both from a mathematically point-of-view. The first sections (2.1 and 2.2) are the derivation of $v \sin i$ values via FT method and the subsequent sections (2.3 to 2.6) are are devoted to the Fredholm integral equation with a non-isotropic axial distribution modeling.

2.1 Stellar rotation

Before starting to describe FT technique to obtain the projected rotational velocity from a stellar spectra line, a context of stellar rotation is necessary to explain the Doppler effect, geometry of a rotating star and the intrinsic line profile.

2.1.1 Doppler effect

Christian Doppler in 1842 proposed the Doppler effect, this is the effect produced by a moving source of waves with respect to a relative observer in which there is an apparent shift in wavelength (or frequency). The change of wavelength (or frequency) depends on the speed of the source moving toward/outward to the relative observer.

For definition, considering the electromagnetic radiation, these waves propagate in the vacuum with the following dispersion relationship

$$c = \lambda \nu, \tag{2.1}$$

where c is the speed of light, λ the wavelength and ν the frequency of the wave. Eq. 2.1 indicates the relation between wavelength and frequency, the higher the frequencies, the lower the wavelengths, and vice versa.

The relation between the wavelength emitted for a source at rest (λ_{emit}) and the wavelength measured by an observer (λ_{obs}) moving with speed $\pm\left|\vec{V}\right|$ is

$$\lambda_{obs} = \lambda_{emit}\left(\frac{c \pm \left|\vec{V}\right|}{c}\right), \tag{2.2}$$

where the positive and negative sign mean that the observed wavelength is redshifted or blueshifted, respectively, with respect to the wavelength at rest.

2.1.2 Geometry

To describe mathematically the phenomenon of stellar rotation, a geometrical shape of the star with respect to the observer has to be considered (see Fig. 2.1). As we can note, this is a 3-Dimensional extension of Fig. 1.1 (with some minor changes) and hence, more complex. The star is assumed to be a sphere rotating as a rigid body.

In Fig. 2.1, the rotation axis for the star lies over the $y-z$ plane, and the observer is standing in the $z-$axis. This conventional geometry offers simplicity since the rotation axis of the star with respect to the observer line of sight is given only by an angle i, being $\sin i$ the y component of rotation axis. The velocity vector at any point on the stellar surface ($\vec{v}$) is computed by

$$\vec{v} = \vec{\Omega} \otimes \vec{R}, \tag{2.3}$$

where $\vec{\Omega}$ $(= \Omega_x\hat{x} + \Omega_y\hat{y} + \Omega_z\hat{z})$ is the angular rotational vector and $\vec{R}$ $(= x\hat{x} + y\hat{y} + z\hat{z})$ is the position vector on the surface of the sphere, the term $\otimes$ means the vector product. Solving eq. 2.3 for the z component of the rotational velocity (v_z) gives $v_z = |y\Omega_x - x\Omega_y|$ but reminding that there is no x component in $\vec{\Omega}$ ($\Omega_x = 0$) and $\Omega_y = \Omega \sin i$, therefore

$$v_z = x\Omega \sin i. \tag{2.4}$$

An important interpretation of eq. 2.4 is that stellar surface shaving the same x coordinate can be divided into strips (as stellar disks), being the Doppler shift constant

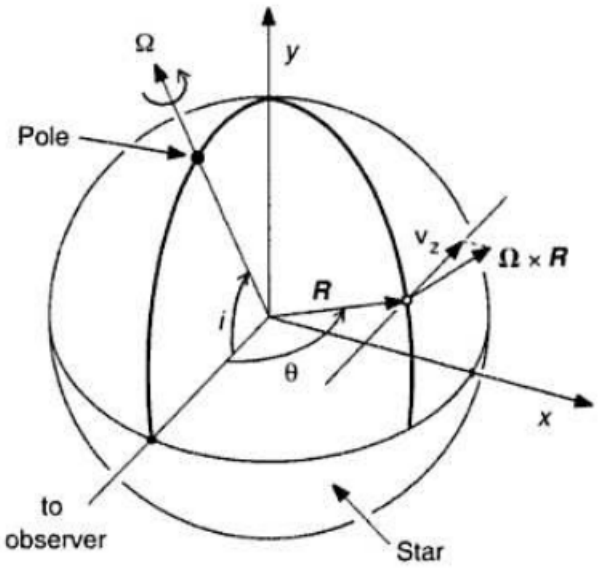

Figure 2.1: 3-Dimensional shape of rotation axis for a star with respect to the observer. *Credit*: Gray (2005), Chapter 18, Fig 18.2.

along each strip with respect to the line of sight. As it can be imagined, the largest strip, and hence, the largest velocity (v, the equatorial velocity of the star) occurs where $x = R$ described by

$$v_L = R\Omega \sin i = v \sin i, \tag{2.5}$$

where v_L can be understood as the observed (or projected) rotational velocity in the z direction (line of sight for the observer).

2.1.3 Intrinsic line profile

Now, it is necessary to describe the Doppler broadening effect with respect to the flux of a rotating star (F_λ) for a specific wavelength (Gray, 2005), namely

$$F_\lambda = \oint I_\lambda \cos\theta \, d\omega, \tag{2.6}$$

where I_λ is the specific intensity, ω the solid angle and θ the angular limb distance with respect to the equatorial latitude.

Using stellar atmosphere models, it is possible to obtain F_λ numerically, computing I_λ at many points on the disk, however, our goal is to use the FT to obtain the projected

rotational velocity. To do this, first it is necessary to define the normalized flux profile for a non-rotating star, that can be written as

$$\frac{F_\lambda}{F_c} = \frac{\oint H(v) I_c \cos\theta \, d\omega}{\oint I_c \cos\theta \, d\omega}, \tag{2.7}$$

where F_c is the continuum flux, I_c the continuum intensity and $H(v)$ $(= I_\lambda / I_c)$ is the ratio of intensity at any point in the spectrum to the continuum intensity, defined as the intrinsic line profile at any point on the disk. If $H(v)$ does not depend on the location of the disk, then

$$\frac{F_\lambda}{F_c} = H(v), \tag{2.8}$$

but usually $H(v)$ has a dependence on the disk position. In the next section a rotational case is derived for eq. 2.7.

2.2 Rotational broadening offset

The effect of rotation is not the only responsible to broad a spectral line profile. In massive stars (specifically O- and B-type), Struve (1952) suggested additional unknown mechanism that conduct to broad the lines and following studies confirm this (Slettebak, 1956; Conti & Ebbets, 1977; Penny, 1996; Howarth et al., 1997; Ryans et al., 2002; Simón-Díaz & Herrero, 2007). To solve this issue, Simón-Díaz & Herrero (2014) developed an user-friendly IDL tool (called IACOB) using FT and goodness-of-fit methodologies, which characterize the phenomenon of macroturbulence (large-scale turbulent motion), microtubulence (small-scale turbulent motion) and rotation together in OB-type stars. In this section we describe the line-broadening assuming only rotation, neglecting other mechanisms.

2.2.1 Rotational kernel

For a rotating star, $H(v)$ depends on the disk position via Doppler effect, therefore, eq. 2.6 becomes:

$$F_\lambda = \oint H(v - v_z) I_c d\omega, \tag{2.9}$$

taking $d\omega = dA/R^2$ where dA is the differential surface area on the star of radius R and $dA = dxdy$, eq. 2.9 reads as:

$$F_\lambda = \int\int H(v - v_z) I_c \frac{dxdy}{R^2}, \tag{2.10}$$

the ratio between eq. 2.4 and eq. 2.5 in term of v_z is:

$$\frac{x}{R} = \frac{v_z}{v_L}, \tag{2.11}$$

and replacing this into eq. 2.10, it is necessary to define the limits of integration for y as y_l in term of v_z as

$$y_l = \sqrt{R^2 - x^2} = R\sqrt{1 - \left(\frac{v_z}{v_L}\right)^2}, \tag{2.12}$$

thus, running x from $-R$ to R and y from $-y_l$ to y_l, eq. 2.10 divided by F_c transform to

$$\frac{F_\lambda}{F_c} = \int_{-R}^{R} H(v - v_z)\left(\int_{-y_l}^{y_l} \frac{I_c dy}{R v_z}\right) dv_z \oint I_c \cos\theta \, d\omega. \tag{2.13}$$

Now, taking into account the ratio between $\int_{-y_l}^{y_l} \frac{I_c dy}{R v_z}$ and $\oint I_c \cos\theta \, d\omega$ (evaluating only the y_l limits), we can define as the rotational profile $G(v_z)$, for $v_z < v_L$ as

$$G(v_z) = \frac{1}{v_L} \frac{\int_{-y_l}^{y_l} I_c dy / R}{\oint I_c \cos\theta \, d\omega}. \tag{2.14}$$

2.2.2 Limb darkening parameter

Stars do not bright uniformly, the intensity decrease from the center to the borders and this phenomenon is called limb darkening. The study was first proposed by a work titled "On the determination of the orbital elements of eclipsing variable stars" (Russell, 1912a,b) that contributed to be research in many fields of astrophysics such as exoplanets transit, LTE and non-LTE stellar spectral analysis, among others (Fukue & Akizuki, 2006; Howarth, 2011; Neilson & Lester, 2011, 2012, 2013; Levenhagen, 2014). The linear limb darkening (ϵ) is usually considered as a linear law (for further details visit Gray, 2005) defined as follow:

$$I_c = I_c^0((1 - \epsilon) + \epsilon \cos\theta), \tag{2.15}$$

where I_c^0 is the specific intensity at the center of the disk. The parameter ϵ takes values between 0 and 1, for $\epsilon = 0$ there is no angular limb contribution to the specific intensity and in contrast, for $\epsilon = 1$ there is an angular limb position that contribute to

describe I_c. There are also estimations of $v \sin i$ via FT under different non-linear limb darkening laws (Levenhagen, 2014) as: quadratic (Kopal, 1950), square-root (Diaz-Cordoves & Gimenez, 1992) and logarithmic limb darkening law (Klinglesmith & Sobieski, 1970). Combining eq. 2.14 with eq. 2.15, for a linear limb darkening law, this result in:

$$G(v_z) = \frac{1}{v_L} \frac{\int_{-y_l}^{y_l} I_c^0((1-\epsilon)+\epsilon\cos\theta)dy/R}{\oint I_c \cos\theta \, d\omega}, \tag{2.16}$$

$$G(v_z) = \frac{1}{v_L} \frac{\frac{I_c^0}{R}\int_{-y_l}^{y_l}((1-\epsilon)+\epsilon\cos\theta)dy}{\oint I_c \cos\theta \, d\omega}, \tag{2.17}$$

$$G(v_z) = \frac{1}{v_L} \frac{\frac{2I_c^0}{R}\int_{0}^{y_l}((1-\epsilon)+\epsilon\cos\theta)dy}{\oint I_c \cos\theta \, d\omega}, \tag{2.18}$$

where the analytical integration of $\oint I_c \cos\theta \, d\omega$ is given by

$$\oint I_c \cos\theta \, d\omega = \pi I_c^0(1-\epsilon/3), \tag{2.19}$$

and therefore eq. 2.18 result in:

$$G(v_z) = \frac{1}{v_L} \frac{\frac{2I_c^0}{R}\int_{0}^{y_l}((1-\epsilon)+\epsilon\cos\theta)dy}{\pi I_c^0(1-\epsilon/3)}, \tag{2.20}$$

$$G(v_z) = \frac{1}{v_L \pi(1-\epsilon/3)} \frac{2}{R}\int_{0}^{y_l}((1-\epsilon)+\epsilon\cos\theta)dy, \tag{2.21}$$

$$G(v_z) = \frac{1}{v_L \pi(1-\epsilon/3)} \left(\frac{2(1-\epsilon)y_l}{R} + \frac{2\epsilon}{R}\int_{0}^{y_l}\cos\theta dy\right), \tag{2.22}$$

$$G(v_z) = \frac{1}{v_L \pi(1-\epsilon/3)} \left(\frac{2(1-\epsilon)y_l}{R} + \frac{\pi\epsilon y_l^2}{2R^2}\right), \tag{2.23}$$

$$G(v_z) = \frac{1}{v_L \pi(1-\epsilon/3)} \left(2(1-\epsilon)\sqrt{1-(v_z/v_L)^2} + \frac{1}{2}\pi\epsilon\big(1-(v_z/v_L)^2\big)\right), \tag{2.24}$$

this is the form of the kernel that contributes to the broadening of the line profile via Doppler effect.

Coming back to eq. 2.14, this is defined as

$$\frac{F_\lambda}{F_c} = \int_{-\infty}^{\infty} H(v-v_z)G(v_z)dv_z, \tag{2.25}$$

the last integral equation is defined as the normalized line profile and it is a convolution between $H(v)$ and $G(v_z)$ given by

$$\frac{F_\lambda}{F_c} = H(v - v_z) * G(v_z), \tag{2.26}$$

where this point-wise product $*$ represents the convolution and the observed line profile $D(v)$ is defined as:

$$D(v) = H(v - v_z) * G(v_z), \tag{2.27}$$

this tell us that as long as $H(v)$ has the same shape over the disk of the star, we can take the flux profile, as eq. 2.8 for a non-rotating star and convolve it with the rotation profile $G(v_z)$ to obtain the rotational broadened flux profile. The larger the rotational rate, the wider $G(v_z)$ is in comparison to $H(v)$, making the flux profile looks like $G(v_z)$ (Gray, 2005).

2.2.3 Fourier Transform to the rotational convolution

Considering eq. 2.27, when the convolution theorem is applied (see eq. A.11 in Appendix A), then

$$F\{H(v - v_z) * G(v_z)\} = h(\nu)g(\nu), \tag{2.28}$$

where now ν is the domain of the "frequencies", $h(\nu)$ and $g(\nu)$ are the FT of $H(v)$ and $G(v_z)$, respectively. An analytical function for $g(\nu)$ was given by (Carroll, 1933; Carroll & Ingram, 1933) is:

$$g(\nu) = \frac{J_1(2\pi v_L \nu\lambda/c)}{2\pi v_L \nu\lambda/c} - \frac{3\cos 2\pi v_L \nu\lambda/c}{2(2\pi v_L \nu\lambda/c)^2} + \frac{3\sin 2\pi v_L \nu\lambda/c}{2(2\pi v_L \nu\lambda/c)^3}, \tag{2.29}$$

where J_1 is the first order Bessel function. To get the projected stellar rotational velocity, v_L, the first zero of the analytical form of $g(\nu)$, yields the velocity via a very important relation (Reiners & Schmitt, 2002; Gray, 2005), which is

$$v_L \nu\lambda/c = 0.610 + 0.612\epsilon + 0.027\epsilon^2 + 0.012\epsilon^3 + 0.004\epsilon^4. \tag{2.30}$$

For this work we use $\epsilon = 0.6$ (same as Carroll, 1933; Bruning, 1981; Gray, 2005) and the last expression gives $v_L \nu\lambda/c = 0.66$. Thus, when the derivative of $g(\nu)$ pass from negative to positive (first zero), and knowing the respective ν value, then dividing 0.66

by $v\lambda/c$, the observed rotational velocity is finally computed. That is the complete mathematical procedure to obtain $v \sin i$ via FT with a linear limb darkening law.

2.3 Astronomical inverse problems

In science, direct problems are classified as phenomenon that can be understood mathematically, and hence, the causative effects are hypothesized by physical models and compared with experimental data. In contrast, since most of astronomical observations reveals the consequence but not the cause in extraterrestrial objects, this is known as an inverse problem. Some specific astrophysical examples that can be treated as inverse problems are Doppler imaging of stellar surfaces, eclipse mapping of accretion disks, CO mapping of galactic disks, reverberation mapping of gas in Active Galactic Nuclei and intrinsic shapes of galaxies (see, e.g., Lucy, 1994).

2.3.1 Historical remarks

In stellar rotation context, the first paper in relate the distribution of equatorial (or true) rotational velocities $f_{true}(x = v)$ and the apparent (or projected) rotational velocities $f_{proj}(y = v \sin i)$ was performed by Chandrasekhar & Münch (1950). They assumed a random orientation of rotational axes (Struve, 1945; van Dien, 1948). The integral equation that govern these two distributions is defined by a Fredholm integral as

$$f_{proj}(y) = \int_y^\infty \frac{y}{x\sqrt{x^2 - y^2}} f_{true}(x) dx, \tag{2.31}$$

where the expression $p(y|x) = \frac{y}{x\sqrt{x^2-y^2}}$ is the kernel of the integral equation. $p(y|x)$ is derived from the isotropic distribution of stellar axes on the unit sphere of observation. They also obtained a formal solution via an Abel's integral equation for the PDF of the true rotational velocity using $f_{proj}(y)$ as an observable. This solution can lead to mislead results because requires a derivation, unless the sample is of very high precision. Later, Lucy (1974) presented an iterative technique for the rectification of observed distributions which derives from Bayes theorem on conditional probabilities and, at each iteration, increases the likelihood of the observed sample to obtain the distribution of interest.

2.3.2 Motivation

One interesting type of rotating stars are Be stars, Fig. 2.2 displays a sample of 627 field Be stars (Yudin, 2001) along the galactic plane.

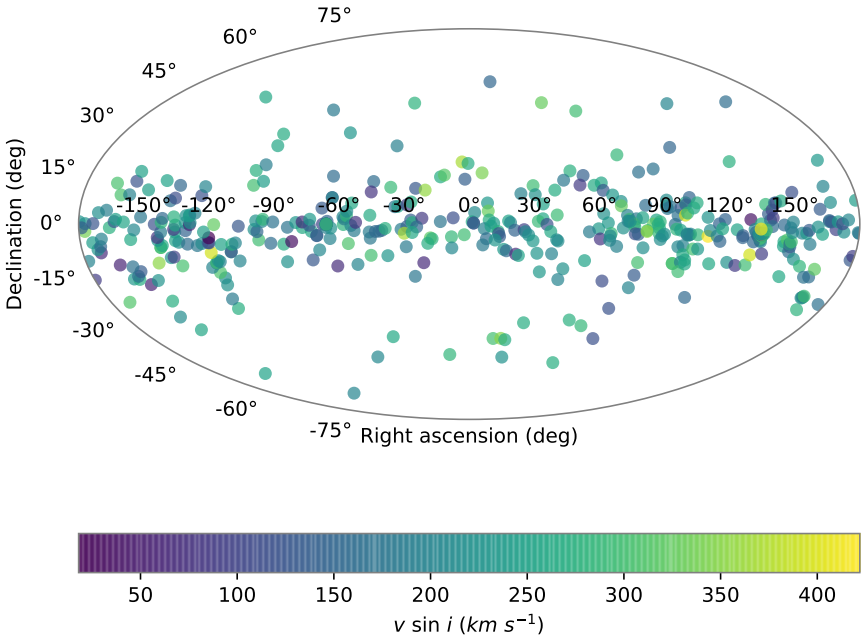

Figure 2.2: Spatial distribution of field Be stars in the galactic plane.

To these 627 field Be stars, this value of $v \sin i$ is known and using eq. 2.31, it is possible to obtain $f_{true}(x)$ via a deconvolution method called Tikhonov regularization (Tikhonov & Goncharsky, 1987; Tikhonov et al., 1998). How this method works is explained in detail in section 3.2. After Tikhonov deconvolution of Yudin (2001) is applied, Fig. 2.3 shows the behavior of the respective PDFs of true and projected rotational velocities.

In this figure, we observe for $v < 120$ $(km\ s^{-1})$, that $f_{true}(v)$ is negative, and for

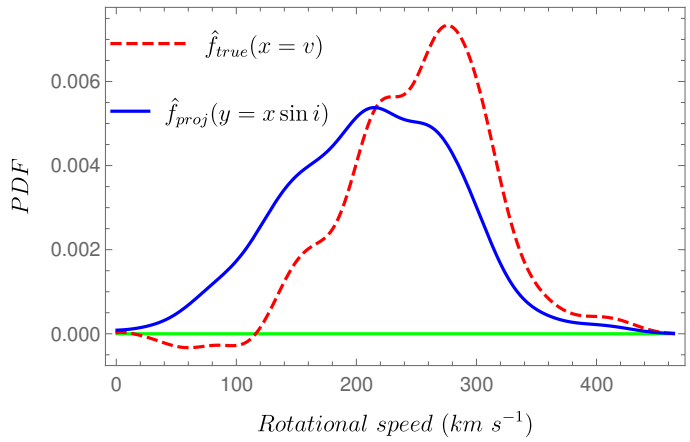

Figure 2.3: PDFs for $f_{proj}(y = x \sin i)$ in blue curve and $f_{true}(x = v)$ in red dashed curve from Yudin (2001) database. The green horizontal line is the representation for the zero probability in the whole range of rotational speeds.

definition there is not possible to have a negative PDF. We attribute this problem to the isotropic distribution of axes over the unit sphere. The first study on modify the kernel (eq. 2.31) to describe a non-spherical distribution was proposed by Zorec et al. (2016) via the next equation (adopted to our nomenclature)

$$f_{proj}(y, \alpha) = c_\alpha \int_y^\infty \frac{y^{1+2\alpha}}{x^{1+2\alpha}\sqrt{x^2 - y^2}} f_{true}(x, \alpha) dx, \tag{2.32}$$

where the α parameter is a non-isotropic description of the distribution of axes and c_α is a normalization constant. The $v \sin i$ sample used in this work has 233 Galactic classical Be stars (Chauville et al., 2001; Frémat et al., 2005; Zorec et al., 2005; Frémat et al., 2006; Levenhagen & Leister, 2006). Zorec et al. (2016) deconvolved the PDFs for true rotational velocities at three different α values (-0.25, 0 and 0.25) showed in Fig. 2.4.

Although this non-isotropic formulation is very novel, no more has been done up to date and this is one of reason for the motivation to expand the research in this framework of astrophysics and statistics.

2.3.3 Axes on the unit sphere

It was explained, the α parameter in eq. 2.32 yields the non-isotropic distribution of axes but it wasn't quantified how much affect the inclination angles with respect to

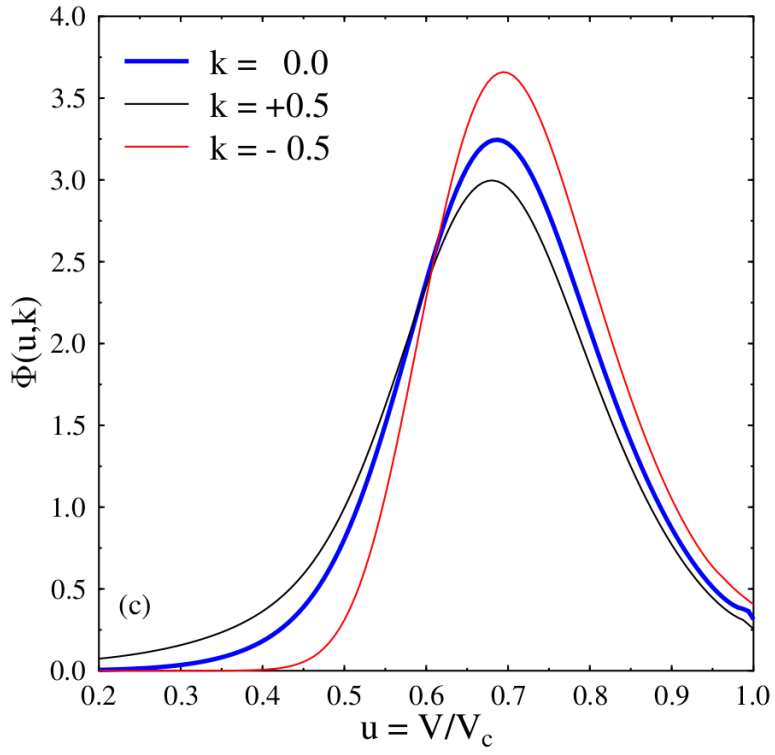

Figure 2.4: PDFs $\Phi(u,k)$ of true rotational velocities V normalized by the respective critical velocity V_c for $k = 0$ (blue curve), $k = 0.5$ (black curve) and $k = -0.5$ (red curve). $\Phi(u,k)$ is not normalized. The conversion from their notation to our is $k \to 2\alpha$, $u = V/V_c \to x = V$ and $\Phi(u,k) \to f_{true}(x,\alpha)$. *Credit*: Zorec et al. (2016), Fig. 10 (c)

the line of sight. In Fig. 2.5 black dots represent the rotational axes on the unit sphere of observation at four different α values.

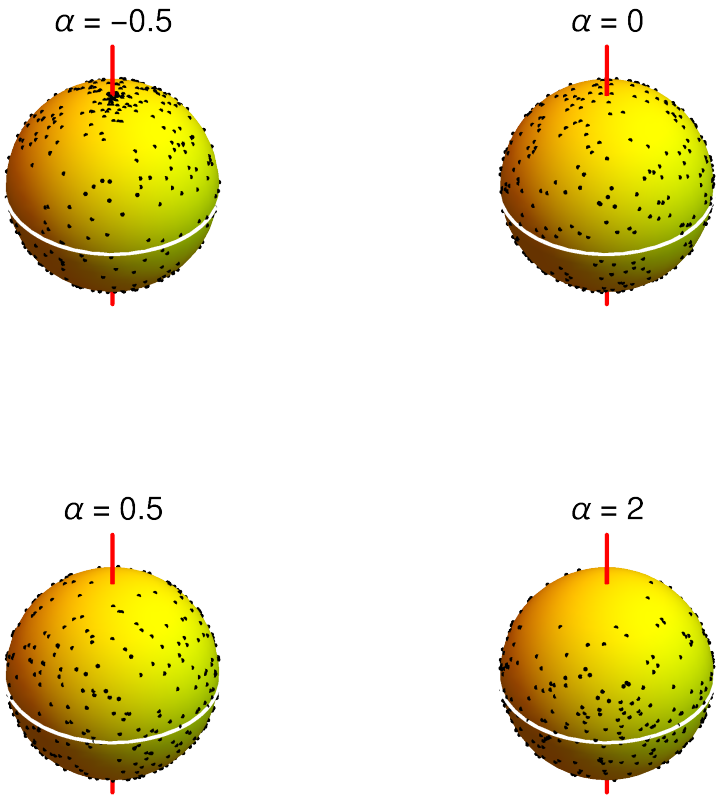

Figure 2.5: Axes distribution on the unit sphere of observation (black dots) for $\alpha = -0.5$ (top left), 0 (top right), 0.5 (bottom left) and 2 (bottom right).

For $\alpha = 0$, a spherical distribution over the unit sphere axes for rotating star is expected. Otherwise, for $\alpha < 0$ the axes are going to be more distributed near to the pole of the line of sight and the specifically case of $\alpha = -0.5$ shows this behavior. In contrast, at $\alpha > 0$ the rotational axes with respect to the line of sight of the observer is going to be more aligned to the equator.

2.4 Uniform distribution of stellar axes

To begin with the second part of the mathematical foundations, the distribution of v and $v \sin i$, we start defining the Fredholm integral equation using an isotropic distribution of stellar axes.

2.4.1 Fredholm integral

Let X and S be two random independent variables such that $0 < X < \infty$ and $S \in [0,1]$. If $Y = XS$, we want to relate the corresponding PDFs of these three variables ($f_Y(y)$, $f_X(x)$ and $f_S(s)$). Considering the transformation $T(x,y) = (x, xs)$, with PDFs $f_{XY}(x,y)$ and $f_{XS}(x,s)$, the probability contained in a differential area must be invariant under change of variables, that is

$$|f_{XY}(x,y)\partial(x,y)| = |f_{XS}(x,s)\partial(x,s)|, \tag{2.33}$$

and solving for $f_{XY}(x,y)$, then

$$f_{XY}(x,y) = f_{XS}(x,s)\left|\frac{\partial(x,s)}{\partial(x,y)}\right|. \tag{2.34}$$

Furthermore, it is verified that $T^{-1}(x,y) = (x, y/x)$ and the last equation gives

$$f_{XY}(x,y) = f_{XS}\Big(T^{-1}(x,y)\Big)\left|\frac{\partial T^{-1}(x,y)}{\partial(x,y)}\right|, \tag{2.35}$$

$$f_{XY}(x,y) = f_{XS}(x,y/x)\left|\frac{\partial(x,y/x)}{\partial(x,y)}\right|. \tag{2.36}$$

The right expression of eq. 2.36 can be rewritten by applying the determinant (*det*) to $\frac{\partial(x,y/x)}{\partial(x,y)}$ by

$$\left|\frac{\partial(x,y/x)}{\partial(x,y)}\right| = det\left(\frac{\partial(x,y/x)}{\partial(x,y)}\right), \tag{2.37}$$

$$\left|\frac{\partial(x,y/x)}{\partial(x,y)}\right| = \left|\begin{pmatrix} 1 & 0 \\ -1/x^2 & 1/x \end{pmatrix}\right|, \tag{2.38}$$

$$\left|\frac{\partial(x,y/x)}{\partial(x,y)}\right| = \frac{1}{x}, \tag{2.39}$$

from the last expression, eq. 2.36 results in:

$$f_{XY}(x,y) = f_{XS}(x, y/x)\frac{1}{x}, \tag{2.40}$$

thus the independence of variables guarantees that there is possible to separate $f_{XS}(x, y/x)$ as:

$$f_{XS}(x, y/x) = f_X(x) f_S(y/x), \tag{2.41}$$

and $f_{XY}(x, y)$ as:

$$f_{XY}(x,y) = f_X(x) f_Y(y), \tag{2.42}$$

then we obtain:

$$f_X(x) f_Y(y) = f_X(x) f_S(y/x)\frac{1}{x}. \tag{2.43}$$

Thus, to obtain the marginal distribution of Y, an integration of the variable x is performed

$$\int_0^\infty f_X(x) f_Y(y) dx = \int_0^\infty f_X(x) f_S(y/x)\frac{1}{x} dx, \tag{2.44}$$

$$f_Y(y)\int_0^\infty f_X(x) dx = \int_0^\infty f_X(x) f_S(y/x)\frac{1}{x} dx, \tag{2.45}$$

$$f_Y(y) = \int_0^\infty f_X(x) f_S(y/x)\frac{1}{x} dx, \tag{2.46}$$

$$f_Y(y) = \int_0^\infty \frac{1}{x} f_S(y/x) f_X(x) dx. \tag{2.47}$$

Remembering that $x > y$, the limit of the integral yields

$$f_Y(y) = \int_y^\infty \frac{1}{x} f_S(y/x) f_X(x) dx, \tag{2.48}$$

this relation is similar to the Fredholm integral equation in 1D, which reads

$$f_Y(y) = \int_y^\infty p(x,y) f_X(x) dx, \tag{2.49}$$

where the kernel $p(x, y)$ in the integral equation represents the unavoidable averaging operation associated with the remoteness of the observer (this is our case) or with the measurement process. In our case the projection of the distribution of stellar axes. As

the true rotational velocities v depends directly from the projected ones $v \sin i$, then the kernel is converted to a conditional distribution of the projected angles by $p(x|y)$ and finally the Fredholm integral equation reads as

$$f_Y(y) = \int_y^\infty p(x|y) f_X(x) dx, \tag{2.50}$$

in which the kernel $p(x|y)$ is an unknown function and an assumption about the distribution of stellar axes should be imposed to derive an analytical expression.

2.4.2 Projected and true rotational velocities

Let a random vector $\mathbf{x} \in \mathbb{R}^3$ and $\mathbf{y}$ the projection of $\mathbf{x}$ to the plane normal to the line of sight. If $X = ||\mathbf{x}||$, $Y = ||\mathbf{y}||$ and i is the perpendicular component of the angle between $\mathbf{x}$ and the line of sight, considering an unitary sphere where $S = |\sin i| = Y/X \in [0, 1]$, the condition $S \leq s$ is equivalent to $\hat{\mathbf{x}} = \mathbf{x}/X \in A$, where A is the region on the unit sphere showed for the polar caps, which is, the region expressed in spherical coordinates for $\theta \in [0, 2\pi]$ and $i \in [0, i_0]$ having $i = \arcsin s \in [0, \pi/2]$ (see Fig. 2.6).

We assume that the variables X and $\hat{\mathbf{x}}$ are independent and $\hat{\mathbf{x}}$ is distributed uniform over the sphere, in other words, $P(\hat{\mathbf{x}} \in A)$ is proportional to the area A and therefore

$$P(S \leq s) = \frac{A}{4\pi}, \tag{2.51}$$

$$P(S \leq s) = \frac{1}{2\pi} \int_0^{i_0} \int_0^{2\pi} \sin i \, d\theta di, \tag{2.52}$$

$$P(S \leq s) = \int_0^{i_0} \sin i \, di, \tag{2.53}$$

$$P(S \leq s) = 1 - \cos(\arcsin(s)), \tag{2.54}$$

$$P(S \leq s) = 1 - \sqrt{1 - s^2}, \tag{2.55}$$

thus, $f_S(s)$ verifies the following relation:

$$f_S(s) = \frac{d}{ds} P(S \leq s), \tag{2.56}$$

$$f_S(s) = \frac{d}{ds}\left(1 - \sqrt{1 - s^2}\right), \tag{2.57}$$

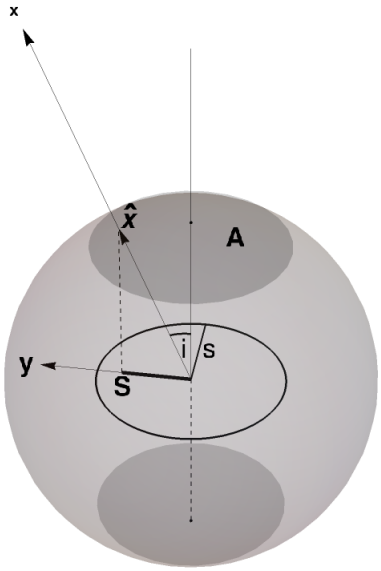

Figure 2.6: Geometry of the projection of a stellar axis. The vector **x** represent the stellar rotational velocity, $\hat{\mathbf{x}}$ its unitary vector and **y** is the projected rotational speed. Vector $\hat{\mathbf{x}}$ is inside the polar cap region A. These caps subtend an angle $\pm i_0$ (not shown here, see text for more details).

$$f_S(s) = \frac{s}{\sqrt{1-s^2}}, \tag{2.58}$$

with the change of variable $s = y/x$, we obtain

$$f_S(y/x) = \frac{y/x}{\sqrt{1-(y/x)^2}}, \tag{2.59}$$

$$f_S(y/x) = \frac{y}{\sqrt{x^2-y^2}}, \tag{2.60}$$

and substituting into eq. 2.48

$$f_Y(y) = \int_y^\infty \frac{y}{x\sqrt{x^2-y^2}} f_X(x)dx, \tag{2.61}$$

being the same eq. 2.31, where $f_Y(y) \to f_{proy}(y)$ and $f_X(x) \to f_{true}(x)$ are the projected and true rotational velocities PDFs, respectively.

2.5 Non-isotropic distribution of stellar axes

The revolutionary part of this thesis is given by the non-isotropic distribution of stellar axes, as we present a new way to study the rotational velocities using the Fredholm integral equation. This section explains this premise.

2.5.1 General case

To provide a general case of the kernel into the Fredholm integral equation, an angle distribution function $h(i,\theta)$ with two angle terms has to be supposed $i \in [0, i_0] \cup [\pi - i_0, \pi]$ where are represented by the north and south polar caps for the following relation

$$P(S \leq s) = \frac{1}{4\pi}\int_0^{i_0}\int_0^{2\pi} h(i,\theta)\sin i\, d\theta di + \frac{1}{4\pi}\int_{\pi-i_0}^{\pi}\int_0^{2\pi} h(\pi-i,\theta)\sin i\, d\theta di, \tag{2.62}$$

for symmetry with respect to the equator, we have that

$$h(i,\theta) = h(\pi - i, \theta), \tag{2.63}$$

and eq. 2.62 is

$$P(S \leq s) = \frac{2}{4\pi} \int_0^{i_0} \int_0^{2\pi} h(i,\theta) \sin i \, d\theta di, \tag{2.64}$$

$$P(S \leq s) = \int_0^{i_0} \sin i \int_0^{2\pi} \frac{1}{2\pi} h(i,\theta) \, d\theta di, \tag{2.65}$$

defining

$$\bar{h}(i) = \frac{1}{2\pi} \int_0^{2\pi} h(i,\theta) \, d\theta. \tag{2.66}$$

therefore,

$$P(S \leq s) = \int_0^{i_0} \bar{h}(i) \sin i \, di, \tag{2.67}$$

and using eq. 2.56 to obtain $f_S(s)$ then

$$f_S(s) = \bar{h}(i) \sin(i) \, \frac{di}{ds}, \tag{2.68}$$

$$f_S(s) = \bar{h}(\arcsin(s)) \sin(\arcsin(s)) \frac{d \arcsin(s)}{ds}, \tag{2.69}$$

$$f_S(s) = \bar{h}(\arcsin(s)) s \frac{d \arcsin(s)}{ds}, \tag{2.70}$$

$$f_S(s) = \bar{h}(\arcsin(s)) \frac{s}{\sqrt{1-s^2}}, \tag{2.71}$$

$$f_S(y/x) = \bar{h}(\arcsin(y/x)) \frac{y/x}{\sqrt{1-(y/x)^2}}, \tag{2.72}$$

$$f_S(y/x) = \bar{h}(\arcsin(y/x)) \frac{y}{\sqrt{x^2-y^2}}, \tag{2.73}$$

putting this last expression into the Fredholm integral equation (eq 2.48), yields

$$f_Y(y) = \int_y^{\infty} \bar{h}(\arcsin(y/x)) \frac{y}{x\sqrt{x^2-y^2}} f_X(x) dx, \tag{2.74}$$

being $\bar{h}$ defined by:

(i) domain $[0, \pi/2]$,

(ii) $\bar{h} \geq 0$,

(iii) $\int_0^{\pi/2} \bar{h}(i)di = 1$,

Note that for $\bar{h} = 1$, an uniform distribution of axes results for $f_S(y/x)$ and we want to write the conditions before mentioned in terms of a more general function that we call H. We have three variables: i, s and z related by

$$\cos i = \sqrt{1 - \sin^2 i}, \tag{2.75}$$

$$\cos i = \sqrt{1 - s^2}, \tag{2.76}$$

$$\cos i = z, \tag{2.77}$$

thus, doing the following change of variables ($\cos i = z$), eq. 2.67 becomes in:

$$\int_0^{\pi/2} \bar{h}(i) \sin i \, di = -\int_0^1 \bar{h}(\arccos(z))dz, \tag{2.78}$$

$$\int_0^{\pi/2} \bar{h}(i) \sin i \, di = \int_0^1 \bar{h}(\arccos(z))dz, \tag{2.79}$$

in that form, we call

$$H(u) = \bar{h}(\arccos(z)), \tag{2.80}$$

and the conditions for $\bar{h}$ (i), (ii) and (iii) now for $\bar{H}$ are transformed to:

(v) domain $[0, 1]$,

(vi) $H \geq 0$,

(vii) $\int_0^1 H(z)dz = 1$.

Regarding

$$H(\cos i) = \bar{h}(i), \tag{2.81}$$

$$H\left(\sqrt{1 - s^2}\right) = \bar{h}(\arcsin(s)), \tag{2.82}$$

$$H\left(\sqrt{1 - (y/x)^2}\right) = \bar{h}(\arcsin(y/x)), \tag{2.83}$$

substituting this into eq. 2.74, we finally obtain

$$f_Y(y) = \int_y^\infty H\left(\sqrt{1-(y/x)^2}\right)\frac{y}{x\sqrt{x^2-y^2}} f_X(x)dx, \tag{2.84}$$

resulting the general case for a non-isotropic distribution of stellar axes for the relation $H(z) = H\left(\sqrt{1-(y/x)^2}\right)$.

2.5.2 Angles generator

In this thesis, we propose the following form for the $H(z)$ function:

$$H(z) = c_\alpha(1-z^2)^\alpha, \tag{2.85}$$

thus, to obtain c_α, it is necessary to use the condition (vii) which reads

$$\int_0^1 c_\alpha(1-z^2)^\alpha dz = \int_0^1 H(z)dz, \tag{2.86}$$

$$\int_0^1 c_\alpha(1-z^2)^\alpha dz = 1, \tag{2.87}$$

$$c_\alpha\left(\frac{\pi\Gamma(1+\alpha)}{2\Gamma(3/2+\alpha)}\right) = 1, \tag{2.88}$$

$$c_\alpha = 1/\left(\frac{\pi\Gamma(1+\alpha)}{2\Gamma(3/2+\alpha)}\right), \tag{2.89}$$

$$c_\alpha = \frac{2\Gamma(3/2+\alpha)}{\pi\Gamma(1+\alpha)}, \tag{2.90}$$

$$c_\alpha = \frac{2}{B(1/2,\alpha+1)}, \tag{2.91}$$

for $\alpha > -1$, where Γ and B are the gamma and beta function respectively. After having c_α, eq. 2.85 reads:

$$H(z) = \frac{2}{B(1/2,\alpha+1)}(1-z^2)^\alpha, \tag{2.92}$$

changing to $z = \sqrt{1-(y/x)^2}$

$$H\left(\sqrt{1-(y/x)^2}\right) = \frac{2}{B(1/2,\alpha+1)}\left(1-\left(\sqrt{1-(y/x)^2}\right)^2\right)^\alpha, \tag{2.93}$$

$$H\left(\sqrt{1-(y/x)^2}\right) = \frac{2}{B(1/2,\alpha+1)}\left(1-\left(1-(y/x)^2\right)\right)^{\alpha}, \tag{2.94}$$

$$H\left(\sqrt{1-(y/x)^2}\right) = \frac{2}{B(1/2,\alpha+1)}(y/x)^{2\alpha}, \tag{2.95}$$

$$H\left(\sqrt{1-(y/x)^2}\right) = \frac{2}{B(1/2,\alpha+1)}\frac{y^{2\alpha}}{x^{2\alpha}}, \tag{2.96}$$

and substituting this new general function into eq. 2.84, we obtain

$$f_Y(y) = \frac{2}{B(1/2,\alpha+1)}\int_y^{\infty}\frac{y^{2\alpha}}{x^{2\alpha}}\frac{y}{x\sqrt{x^2-y^2}}\,f_X(x)dx, \tag{2.97}$$

$$\underbrace{f_Y(y)}_{f_{proj}(y,\alpha)} = \underbrace{\frac{2}{B(1/2,\alpha+1)}}_{c_\alpha}\int_y^{\infty}\underbrace{\frac{y^{1+2\alpha}}{x^{1+2\alpha}\sqrt{x^2-y^2}}}_{p(y|x;\alpha)}\underbrace{f_X(x)}_{f_{true}(x,\alpha)}\,dx, \tag{2.98}$$

resulting the same as eq. 2.32 from Zorec et al. (2016), a non-isotropic distribution of stellar axes in the kernel of the Fredholm integral equation in 1D notation.

2.6 Formal solution

Analytical solutions to obtain the distribution of v from $v\sin i$ are reviewed here as the Abel's integral solution and the CDF. Since both solutions needs $f_{proj}(v\sin i)$ and we use the KDE form $\hat{f}_{proj}(v\sin i)$ (see Chapter 3.3), therefore there are semi-analytical formal solutions.

2.6.1 Abel's integral solution

Chandrasekhar & Münch (1950) proposed a formal solution to obtain $f_{true}(x)$ from eq. 2.31 using the following substitutions

$$y^2 = \frac{1}{\eta^2}, \tag{2.99}$$

and

$$x^2 = \frac{1}{\xi^2}, \tag{2.100}$$

where the limits of integration $x = y \to \xi = \eta$ and $x = \infty \to \xi = 0$ becomes

$$f_{proj}\left(\frac{1}{\sqrt{\eta}}\right) = \int_{\eta}^{0} \frac{\left(\frac{1}{\sqrt{\eta}}\right)}{\left(\frac{1}{\sqrt{\xi}}\right)\sqrt{\left(\frac{1}{\sqrt{\xi}}\right)^2 - \left(\frac{1}{\sqrt{\eta}}\right)^2}} f_{true}\left(\frac{1}{\sqrt{\xi}}\right) d\left(\frac{1}{\sqrt{\xi}}\right), \tag{2.101}$$

$$f_{proj}\left(\frac{1}{\sqrt{\eta}}\right) = \int_{\eta}^{0} \frac{\sqrt{\xi}}{\sqrt{\eta}\sqrt{\frac{1}{\xi} - \frac{1}{\eta}}} f_{true}\left(\frac{1}{\sqrt{\xi}}\right) d\left(\frac{1}{\sqrt{\xi}}\right), \tag{2.102}$$

$$f_{proj}\left(\frac{1}{\sqrt{\eta}}\right) = \int_{\eta}^{0} \frac{\sqrt{\xi}\sqrt{\eta\xi}}{\sqrt{\eta}\sqrt{\eta - \xi}} f_{true}\left(\frac{1}{\sqrt{\xi}}\right) d\left(\frac{1}{\sqrt{\xi}}\right), \tag{2.103}$$

$$f_{proj}\left(\frac{1}{\sqrt{\eta}}\right) = \int_{\eta}^{0} \frac{\xi}{\sqrt{\eta - \xi}} f_{true}\left(\frac{1}{\sqrt{\xi}}\right) d\left(\frac{1}{\sqrt{\xi}}\right), \tag{2.104}$$

$$f_{proj}\left(\frac{1}{\sqrt{\eta}}\right) = \int_{\eta}^{0} \frac{\xi}{\sqrt{\eta - \xi}} f_{true}\left(\frac{1}{\sqrt{\xi}}\right) \left(-\frac{1}{2\xi^{3/2}}\right) d\xi, \tag{2.105}$$

$$f_{proj}\left(\frac{1}{\sqrt{\eta}}\right) = \int_{\eta}^{0} \left(-\frac{1}{2}\right) \frac{1}{\sqrt{\xi}\sqrt{\eta - \xi}} f_{true}\left(\frac{1}{\sqrt{\xi}}\right) d\xi, \tag{2.106}$$

$$f_{proj}\left(\frac{1}{\sqrt{\eta}}\right) = \int_{0}^{\eta} \left(\frac{1}{2}\right) \frac{1}{\sqrt{\xi}\sqrt{\eta - \xi}} f_{true}\left(\frac{1}{\sqrt{\xi}}\right) d\xi, \tag{2.107}$$

$$f_{proj}\left(\frac{1}{\sqrt{\eta}}\right) = \int_{0}^{\eta} \frac{f_{true}\left(\frac{1}{\sqrt{\xi}}\right)}{2\sqrt{\xi}\sqrt{\eta - \xi}} d\xi, \tag{2.108}$$

Now, defining

$$g_{proj}(\eta) = f_{proj}\left(\frac{1}{\sqrt{\eta}}\right), \tag{2.109}$$

and

$$g_{true}(\xi) = \frac{1}{2\sqrt{\xi}} f_{true}\left(\frac{1}{\sqrt{\xi}}\right), \tag{2.110}$$

which are the conditions to construct the Abel's integral as

$$g_{proj}(\eta) = \int_{0}^{\eta} \frac{g_{true}(\xi)}{\sqrt{\eta - \xi}} d\xi, \tag{2.111}$$

where it is well known that the solution (Abel, 1826) is given by

$$g_{true}(\xi) = \frac{1}{\pi} \frac{\partial}{\partial \xi} \int_{0}^{\xi} \frac{g_{proj}(\eta)}{\sqrt{\xi - \eta}} d\eta, \tag{2.112}$$

in terms of the original variables it is equivalent to

$$f_{true}(x) = -\frac{2}{\pi}x^2\frac{\partial}{\partial x}x\int_x^\infty \frac{f_{proj}(y)}{y^2\sqrt{y^2-x^2}}dy. \tag{2.113}$$

As we mentioned previously, this differentiation to the integral yields wrong results because the observations are not of perfect precision, that is why we propose a different analytical method to obtain the PDF of true rotational velocities from the apparent one. Let suppose that $\phi(y)$ and $\psi(x)$ are functions accessible to observation and interest respectively and $\tau \in [0,1]$, therefore using the following integral transformation

$$\phi(y) = \int_y^\infty \frac{x}{(x^2-y^2)^\tau}\psi(x)dx, \tag{2.114}$$

where ψ is continuously derivable and ψ' bounded, so the integration by parts is

$$\phi(y) = -\frac{1}{2(1-\tau)}\int_y^\infty (x^2-y^2)^{1-\tau}\psi'(x)dx, \tag{2.115}$$

a derivation with respect to y, we see that

$$\phi'(y) = \int_y^\infty \frac{y}{(x^2-y^2)^\tau}\psi'(x)dx, \tag{2.116}$$

dividing for $(y^2-q^2)^{1-\tau}$

$$\frac{\phi'(y)}{(y^2-q^2)^{1-\tau}} = \int_y^\infty \frac{y}{(y^2-q^2)^{1-\tau}(x^2-y^2)^\tau}\psi'(x)dx, \tag{2.117}$$

integrating over the y variable

$$\int_q^\infty \frac{\phi'(y)}{(y^2-q^2)^{1-\tau}}dy = \int_q^\infty \left(\int_y^\infty \frac{y}{(y^2-q^2)^{1-\tau}(x^2-y^2)^\tau}\psi'(x)dx\right)dy, \tag{2.118}$$

applying the Fubini's theorem (Edmonds, 1977)

$$\int_q^\infty \frac{\phi'(y)}{(y^2-q^2)^{1-\tau}}dy = \int_y^\infty \left(\int_q^\infty \frac{y}{(y^2-q^2)^{1-\tau}(x^2-y^2)^\tau}dy\right)\psi'(x)dx, \tag{2.119}$$

making the change of variables $y = \sqrt{(1-w)q^2+wx^2}$ for the inside integral then

$$\int_q^\infty \frac{y}{(y^2-q^2)^{1-\tau}(x^2-y^2)^\tau}dy = \frac{1}{2}\int_0^1 \frac{1}{(1-w)^\tau w^{1-\tau}}dw, \tag{2.120}$$

$$\int_q^\infty \frac{y}{(y^2-q^2)^{1-\tau}(x^2-y^2)^\tau}dy = \frac{\pi\csc(\tau\pi)}{2}, \tag{2.121}$$

replacing this into eq. 2.119, then

$$\int_q^\infty \frac{\phi'(y)}{(y^2-q^2)^{1-\tau}}dy = \int_q^\infty \left(\frac{\pi \csc(\tau\pi)}{2}\right)\psi'(x)dx, \tag{2.122}$$

$$\int_q^\infty \frac{\phi'(y)}{(y^2-q^2)^{1-\tau}}dy = \frac{\pi \csc(\tau\pi)}{2}\int_q^\infty \psi'(x)dx, \tag{2.123}$$

$$\int_q^\infty \frac{\phi'(y)}{(y^2-q^2)^{1-\tau}}dy = -\frac{\pi \csc(\tau\pi)}{2}\psi(x), \tag{2.124}$$

solving for $\psi(x)$

$$\psi(x) = -\frac{2}{\pi \csc(\tau\pi)}\int_q^\infty \frac{\phi'(y)}{(y^2-q^2)^{1-\tau}}dy, \tag{2.125}$$

$$\psi(x) = -\frac{2\sin(\tau\pi)}{\pi}\int_q^\infty \frac{\phi'(y)}{(y^2-q^2)^{1-\tau}}dy. \tag{2.126}$$

Eventually, using eq. 2.98 with a multiplication and division of x, then

$$f_{proj}(y,\alpha) = c_\alpha \int_y^\infty \left(\frac{x}{x}\right)\frac{y^{1+2\alpha}}{x^{1+2\alpha}\sqrt{x^2-y^2}}f_{true}(x,\alpha)dx, \tag{2.127}$$

$$f_{proj}(y,\alpha) = c_\alpha \int_y^\infty \frac{x\, y^{1+2\alpha}}{x^{2+\alpha}\sqrt{x^2-y^2}}f_{true}(x,\alpha)dx, \tag{2.128}$$

dividing by $y^{1+2\alpha}$

$$f_{proj}(y,\alpha)y^{-1-2\alpha} = c_\alpha \int_y^\infty \frac{x}{x^{2+2\alpha}\sqrt{x^2-y^2}}f_{true}(x,\alpha)dx, \tag{2.129}$$

by this way, the following changes of variables are necessary

$$g_{proj}(y,\alpha) = f_{proj}(y,\alpha)y^{-1-2\alpha}, \tag{2.130}$$

and

$$g_{true}(x,\alpha) = c_\alpha x^{-2-2\alpha} f_{true}(x,\alpha), \tag{2.131}$$

which gives

$$g_{proj}(y,\alpha) = \int_y^\infty \frac{x}{\sqrt{x^2-y^2}}g_{true}(x,\alpha)dx, \tag{2.132}$$

thus is the same relation of eq. 2.114 with $\tau = 0.5$ and the respective solution is

$$g_{true}(x,\alpha) = \frac{-2\sin\pi/2}{\pi}\int_x^\infty \frac{1}{\sqrt{y^2-x^2}} g'_{proj}(y,\alpha)dy, \tag{2.133}$$

$$g_{true}(x,\alpha) = -\frac{2}{\pi}\int_x^\infty \frac{1}{\sqrt{y^2-x^2}} g'_{proj}(y,\alpha)dy, \tag{2.134}$$

$$c_\alpha x^{-2-2\alpha} f_{true}(x,\alpha) = -\frac{2}{\pi}\int_x^\infty \frac{1}{\sqrt{y^2-x^2}} g'_{proj}(y,\alpha)dy, \tag{2.135}$$

$$f_{true}(x,\alpha) = -\frac{2x^{2+2\alpha}}{\pi c_\alpha}\int_x^\infty \frac{1}{\sqrt{y^2-x^2}} g'_{proj}(y,\alpha)dy, \tag{2.136}$$

$$f_{true}(x,\alpha) = -\frac{2x^{2+2\alpha}}{\pi c_\alpha}\int_x^\infty \frac{1}{\sqrt{y^2-x^2}} \Big(f_{proj}(y,\alpha)y^{-1-2\alpha}\Big)' dy, \tag{2.137}$$

$$f_{true}(x,\alpha) = -\frac{2x^{2+2\alpha}}{\pi c_\alpha}\int_x^\infty \frac{1}{\sqrt{y^2-x^2}} \Big(f'_{proj}(y,\alpha)y^{-1-2\alpha} - (1+2\alpha)f_{proj}(y,\alpha)y^{-2-2\alpha}\Big) dy, \tag{2.138}$$

$$\boxed{f_{true}(x,\alpha) = -\frac{2}{\pi c_\alpha}\int_x^\infty \frac{x^{2+2\alpha}}{y^{2+2\alpha}\sqrt{y^2-x^2}} \Big(f'_{proj}(y,\alpha)y - (1+2\alpha)f_{proj}(y,\alpha)\Big) dy,} \tag{2.139}$$

being this final equation the new (semi-)analytical solution from Abel's integral.

2.6.2 Cumulative distribution function

The CDF of the continuous random variable X ($F_X(x)$) can be expressed as the integral of its PDF $f_X(x=t)$, as follows

$$F_X(x) = \int_{-\infty}^x f_X(t)dt, \tag{2.140}$$

or

$$F_X(x) = 1 - \int_x^\infty f_X(t)dt, \tag{2.141}$$

using that

$$1 - F_X(x) = \int_x^\infty f_X(t)dt, \tag{2.142}$$

where $f_X(t)$ is the same function obtained in 2.139, for $f_X(t) \to f_{true}(t,\alpha)$ and $F_X(x) \to F_{true}(x,\alpha)$, then

$$1 - F_{true}(x,\alpha) = \int_x^\infty \left(-\frac{2}{\pi c_\alpha} \int_\zeta^\infty \frac{t^{2+2\alpha}}{y^{2+2\alpha}\sqrt{y^2-t^2}} \Big(f'_{proj}(y,\alpha)y - (1+2\alpha) f_{proj}(y,\alpha) \Big) dy \right) dt, \tag{2.143}$$

$$1 - F_{true}(x,\alpha) = -\frac{2}{\pi c_\alpha} \int_x^\infty \left(\int_\zeta^\infty \frac{t^{2+2\alpha}}{y^{2+2\alpha}\sqrt{y^2-t^2}} \Big(f'_{proj}(y,\alpha)y - (1+2\alpha) f_{proj}(y,\alpha) \Big) dy \right) dt, \tag{2.144}$$

$$1 - F_{true}(x,\alpha) = -\frac{2}{\pi c_\alpha} \int_x^\infty \left(\int_\zeta^y \frac{t^{2+2\alpha}}{\sqrt{y^2-t^2}} dt \right) \Big(f'_{proj}(y,\alpha)y - (1+2\alpha) f_{proj}(y,\alpha) \Big) \frac{1}{y^{2+2\alpha}} dy, \tag{2.145}$$

where the solution for the inside integral is given by

$$\int_\zeta^y \frac{t^{2+2\alpha}}{\sqrt{y^2-t^2}} dt = \frac{y^{2+2\alpha}\big(\sqrt{\pi}(3/2+\alpha) - B\big((x/y)^2, 3/2+\alpha, 1/2\big)\Gamma(2+\alpha)\big)}{2\Gamma(2+\alpha)}, \tag{2.146}$$

$$\int_\zeta^y \frac{t^{2+2\alpha}}{\sqrt{y^2-t^2}} dt = y^{2+2\alpha}\Psi(x,y), \tag{2.147}$$

where $\Psi(x,y,\alpha)$ is defined as:

$$\Psi(x,y,\alpha) = \frac{\big(\sqrt{\pi}(3/2+\alpha) - B\big((x/y)^2, 3/2+\alpha, 1/2\big)\Gamma(2+\alpha)\big)}{2\Gamma(2+\alpha)}, \tag{2.148}$$

thus, replacing in 2.145

$$1 - F_{true}(x,\alpha) = -\frac{2}{\pi c_\alpha} \int_x^\infty y^{2+2\alpha}\Psi(x,y,\alpha) \Big(f'_{proj}(y,\alpha)y - (1+2\alpha) f_{proj}(y,\alpha) \Big) \frac{1}{y^{2+2\alpha}} dy, \tag{2.149}$$

$$1 - F_{true}(x,\alpha) = -\frac{2}{\pi c_\alpha} \int_x^\infty \Psi(x,y,\alpha) \Big(f'_{proj}(y,\alpha)y - (1+2\alpha) f_{proj}(y,\alpha) \Big) dy, \tag{2.150}$$

$$1 - F_{true}(x,\alpha) = -\frac{2}{\pi c_\alpha} \left(\int_x^\infty \Psi(x,y,\alpha) f'_{proj}(y,\alpha) y dy - \int_x^\infty \Psi(x,y,\alpha)(1+2\alpha) f_{proj}(y,\alpha) dy \right), \tag{2.151}$$

and solving the first integral by parts we obtain

$$\int_x^\infty \Psi(x,y,\alpha) f'_{proj}(y,\alpha) y dy = y\Psi(x,y,\alpha) f_Y(y,\alpha)|_{y=x}^{y=\infty} - \int_x^\infty (y\Psi(x,y,\alpha))' f_{proj}(y,\alpha) dy, \tag{2.152}$$

having $\Psi(x,x,\alpha) = 0$ and assuming that $f_Y(y,\alpha)$ decays to zero fast enough so that $y\Psi(x,y) f_Y(y)$ tends to zero at infinity, therefore

$$1 - F_{true}(x,\alpha) = -\frac{2}{\pi c_\alpha} \int_x^\infty \Big(\Psi(x,y,\alpha)(1+2\alpha) + (y\Psi(x,y,\alpha))' \Big) f_{proj}(y,\alpha) dy, \tag{2.153}$$

and defining

$$\Omega(x,y,\alpha) = \frac{2}{\pi c_\alpha} \Big(\Psi(x,y,\alpha)(1+2\alpha) + (y\Psi(x,y,\alpha))' \Big), \tag{2.154}$$

$$\Omega(x,y,\alpha) = 1 + \frac{\Gamma(1+\alpha)}{\sqrt{\pi}\Gamma(3/2+\alpha)} \left(\frac{(x/y)^{3+2\alpha}}{\sqrt{1-(x/y)^2}} - (1+\alpha) B\big((x/y)^2, 3/2+\alpha, 1/2\big) \right), \tag{2.155}$$

finally, the analytic solution to obtain the non-isotropic CDF from $f_{proj}(y)$ is given by

$$F_{true}(x,\alpha) = 1 - \int_x^\infty \Omega(x,y,\alpha) f_{proj}(y) dy. \tag{2.156}$$

2.7 Summary

The absorption lines have an intrinsic component of the star and another from the broadening, in which there are the rotation, microturbulence, macroturbulence, instrumental, etc. As we study Be stars, the effect of broadening in the line it is dominated by rotation. That is why in eq. 2.27 we define the profile of the observed line as a convolution between the intrinsic profile of the star and the other as rotation. When applying the FT and make use of the convolution theorem then it is possible to separate these two components and use only with the rotating function in the domain in Fourier. Carroll (1933) proposed that the analytic solution to this rotational component in the space of the frequencies as can be described in eq. 2.29 and the first zero of this equation yields the value of $v \sin i$.

As $v \sin i$ is an observable parameter and v is the value of interest, Chandrasekhar & Münch (1950) proposed a Fredholm integral equation that relates both PDFs assuming an isotropical distribution of stellar axes in the kernel (eq. 2.61). In this thesis, an

α parameter is added to the kernel of the Fredholm integral equation that models a non-isotropy for the distribution of axes (eq. 2.98). Formal solution to obtain the CDF is given in eq. 2.156. This is a very novel solution because solves from the PDF of $v \sin i$ PDF to CDF of v in one step, without convergence criteria or differentiation. In order to compute the PDF of the variable of interest v, a Regularization is performed via Tikhonov regularization and this is described in the next chapter.

CHAPTER 3

Numerical procedures

This chapter describes the numerical procedures in how to obtain $v \sin i$ and how is distributed v from a sample of $v \sin i$. The first part is the derivation of $v \sin i$ value via FT method (section 3.1) and the second one is the Fredholm integral as an ill-posed problem (section 3.2).

3.1 Derivation of $v \sin i$ value via Fourier Transform method

It was explained in previous sections 2.1, 2.2 and appendix A about how to obtain $v \sin i$ from eq. 2.28, and, how to choose the bandwidth from the absorption line is a problem which has not been solved so far. There are several previous studies that do not quantify mathematically how this bandwidth is chosen to apply the FT to obtain the corresponding $v \sin i$ value (Carroll, 1933; Carroll & Ingram, 1933; Ilin & Ivanov, 1979; Jankov, 1995; Reiners & Schmitt, 2002; Reiners, 2003; Gray, 2005; Royer, 2005; Simón-Díaz et al., 2006; Simón-Díaz & Herrero, 2007; Díaz et al., 2011; Ramírez-Agudelo et al., 2013; Levenhagen, 2014; Simón-Díaz & Herrero, 2014). In this thesis we have developed a novel numerical procedure to obtain $v \sin i$ automatically via FT which consist in select the width of the absorption line profile via the best Gaussian profile that fit the signal in study.

3.1.1 Automated procedure

Spectra at different epochs and using one or more absorption lines that trace the surface of the star at a certain theoretical mid wavelength (hereafter midwave or λ_{theo}), then a Gaussian function $p(\lambda, \lambda_{fit}, \sigma_{fit}, A_{fit})$ is fitted to the respective normalized absorption line, given by

$$p(\lambda, \lambda_{fit}, \sigma_{fit}, A_{fit}) = A_{fit} e^{-(\lambda-\lambda_{fit})^2/2\sigma_{fit}^2}, \tag{3.1}$$

where λ_{fit} is the midwave, σ_{fit} the standard deviation and A_{fit} the amplitude of the Gaussian fit. In order to make consistent the fit with respect to the normalized absorption line profile observed expressed as $G_{fit}(\lambda, \lambda_{fit}, \sigma_{fit}, A_{fit})$, the following is established as:

$$G_{fit}(\lambda, \lambda_{fit}, \sigma_{fit}, A_{fit}) = 1 - p(\lambda, \lambda_{fit}, \sigma_{fit}, A_{fit}). \tag{3.2}$$

To perform the corresponding fit, we make use of the programming language Python 3 (Van Rossum & Drake Jr, 1995; Hunter, 2007; Pérez & Granger, 2007; Wes McKinney, 2010; Astropy Collaboration et al., 2013; Virtanen et al., 2020). Firstly, we fit a Gaussian function to a theoretical absorption line profile at λ_{theo} to select the signal of the absorption line in an automated way. For all the Gaussian fits in this research, we use as initial value an amplitude of 0.025 and a standard deviation of the spectrum for a window ± 5 $(\AA)$ with respect to λ_{theo}. This yields for the central line of ± 5 $(\AA)$ and the parameters from the fit are used as inputs to find the optimal G_{fit} at λ_{theo}. An advantage of having a Gaussian profile of the observed line profile is that we can use them to select the spectral window (amount of signal) to be introduced in the FT method (we remind to the reader that obtaining the $v \sin i$ value by FT method is directly affected by the amount of signal used in the analysis) and this consist in use the new values of λ_{fit} and σ_{fit}. This means to obtain $\pm 2\sigma_{fit}$, $\pm 2.5\sigma_{fit}$ and $\pm 3\sigma_{fit}$ on λ_{fit} which yields 95.45%, 98.75% and 99.83% of the signal "area" respectively. Now it is possible to assign the FT to $D(v)$ (eqs. 2.28 to 2.30) to obtain $v \sin i$ automatically for 3 different spectral windows.

Nevertheless, we need to know at what level of confidence is the velocity obtained from the quality of the absorption line. Sometimes the spectrum has too much noise and working with these data can yield significant errors, despite the method used in an astrophysical context, that is why there is necessary to established how "good" is

the line in which the FT is applied to obtain $v \sin i$. We establish 5 criterias to discriminate them:

1. A Gaussian profile is successfully performed $\Rightarrow$ If the observed line profile is indistinguishable with respect to the continuum, then the numerical fit will going to fail at the moment to find the best profile. This is a directly condition from the Signal-to-Noise (S/N) ratio of the spectrum.

2. The observed line profile is in absorption and is below the continuum level, i.e., $G_{fit}(\lambda = \lambda_{fit}, \lambda_{fit}, \sigma_{fit}, A_{fit}) < 1 \Rightarrow$ To obtain the projected rotational velocity of the star due to the Doppler effect, an atomic transition must be in notably absorption to trace the atmospheric surface. The emission lines can gives other type of information, e.g., the observed $H\alpha$ line profile in Be stars gives information of the disk.

3. The center of the Gaussian fit is not shifted more than $3\sigma_{fit}$ with respect to λ_{theo}, i.e., $\lambda_{fit} < |\lambda_{theo} \pm 3\sigma_{fit}| \Rightarrow$ In some cases there is no absorption line in λ_{theo} and the numerically procedure finds another transition line (can be in emission) close to it.

4. The standard deviation of the continuum (σ_c) is lesser than the amplitude of the Gaussian fit, i.e., $\sigma_c < A_{fit} \Rightarrow$ The goal of this criteria is to differentiate if the continuum has too much noise with respect to the line via the value of the amplitude from the fit.

5. The dispersion of the Gaussian fit is larger than 5 times the step of the wavelength ($\Delta\lambda$), i.e., $\sigma_{fit} > 5\Delta\lambda \Rightarrow$ To quantify the quality of the spectrum, it should be at least 5 bins in one σ_{fit} from the Gaussian fit.

If the observed absorption line satisfies these 5 criterias then it is considered as a "good" line and the FT is applied with spectral windows width of $2\sigma_{fit}$, $2.5\sigma_{fit}$ and $3\sigma_{fit}$ to obtain $v \sin i$, on contrary, the observed line profile is not considered and the program follows with the next absorption line. The summary of the whole algorithm to find $v \sin i$ is described in the flowchart, Fig. 3.1 shows it.

3.1.2 BeSOS database

BeSOS offers many spectra of AB supergiants, Herbig and Be stars obtained with the Pontificia Universidad Católica High Echelle Resolution Optical Spectrograph

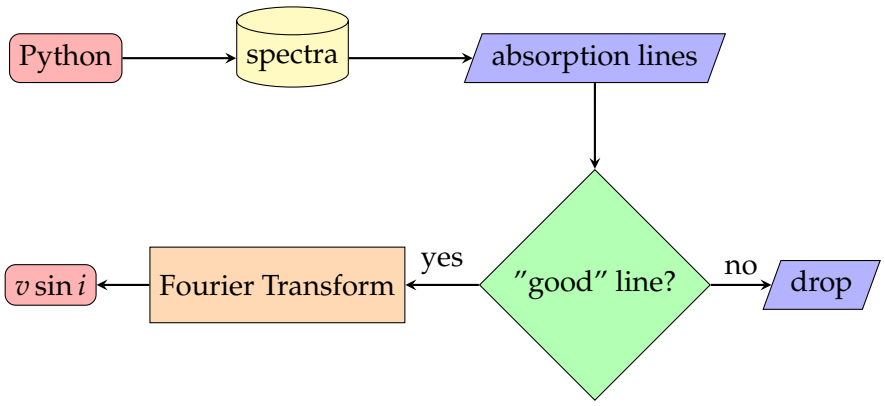

Figure 3.1: Flowchart for the proceeding to obtain $v \sin i$ via FT automatically for three different spectral windows.

(PUCHEROS[1], Vanzi et al., 2012) mounted at the 50cm telescope in Santa Martina Observatory[2]. These observations at different epochs have a resolution of 17000 in the range of $4200 - 7300$ $(\mathring{A})$ and are located in the southern hemisphere. The website of BeSOS has the particularity of visualize the data interactively, up to 12 spectra at different epochs.

This catalog has currently 64 Be stars with a total of 314 different spectra (from 1 to 10 epochs) and as we mentioned in Chapter 1, Be stars are among the fastest rotators. The broadening for the lines for these type of stars is naturally high since the Doppler effect is more dominant, and hence, the other contributions like microturbulence, macroturbulence, thermal broadening and instrumental effects are negligible for the shape of $D(v)$, as defined in eq. 2.27. Furthermore, $\Delta\lambda$ for BeSOS spectra are typically ~ 0.089 $(\mathring{A})$.

Data reduction, extraction and analysis of spectra is a collaboration work of Collection of Elemental Routines for Echelle Spectra (CERES) pipeline (Brahm et al., 2017). Stellar parameters were obtained by Arcos et al. (2018) where they fitted TLUSTY (Hubeny & Lanz, 1995) and Kurucz (Kurucz, 1993) stellar atmosphere models to the observed data to obtain the projected rotational speeds.

[1] `http://www2.astro.puc.cl/ObsUC/index.php/PUCHEROS`
[2] `http://www2.astro.puc.cl/ObsUC/index.php/UC_Observatory`

3.2 Fredholm integral as an ill-posed problem

This section is describe the numerical proceeding for our methods and procedures.

3.2.1 KDE for observable $v \sin i$

To obtain the optimal α value from a sample of $v \sin i$ values such as $f_{proj}(y, \alpha)$, an observable function, no general analytic function can quantify it for different observations, that is why, we use KDE, which is a non-parametric estimation algorithm for the PDF for a random variable (Rosenblatt, 1956; Parzen, 1962; Silverman, 1986). Since the sample of $v \sin i$ are N independently and finite values, defined by Y for $v \sin i$, the unknown PDF $\hat{f}_{proj}(y)$ at any point y is given by

$$\hat{f}_{proj}(y) = \frac{1}{N} \sum_{j=1}^{N} K_h(y - Y_j), \tag{3.3}$$

where K_h is a non-negative scaled kernel function and $h > 0$ is a smoothing parameter called bandwidth. The relation of the scaled kernel and the kernel (K) is as follows

$$K_h(y - Y_j) = \frac{1}{h} K((y - Y_j)/h). \tag{3.4}$$

In this work, we use a Gaussian kernel because is smooth and then eq. 3.3 yields

$$\hat{f}_{proj}(y) = \frac{1}{Nh\sqrt{2\pi}} \sum_{j=1}^{N} e^{-\frac{1}{2}\left((y-Y_j)/h\right)^2}, \tag{3.5}$$

and the bandwidth (Silverman, 1986) is defined as

$$h = 0.9\, min\left(\hat{\sigma}, \frac{IQ}{1.34}\right) N^{-1/5}, \tag{3.6}$$

where $\hat{\sigma}$ is the standard deviation of the random variable under study Y, and IQ is the correspondent interquartile range (Silverman, 1986). Using this non-parametric form, there is possible to get an estimator for the theoretical continuum function $f_{proj}(y)$ as $\hat{f}_{proj}(y)$.

3.2.2 Discretization of the Fredholm integral

It is necessary to work on computers by discretizing eq 2.32 as:

$$\mathbf{b} = M\mathbf{a}, \tag{3.7}$$

where M is a matrix of order $n \times n$ that represent the kernel of eq. 2.98, $\mathbf{a} \in \mathbb{R}^n$ is a vector which is the discrete form of $f_{true}(x, \alpha)$ and $\mathbf{b} \in \mathbb{R}^n$ is the discretization of $\hat{f}_{proj}(y, \alpha)$. Other notation that we use are continuum variables x and y that are expressed as $x_l = [x_1, x_2, ..., x_{n-1}, x_n]$ and $y_l = [y_1, y_2, ..., y_{n-1}, y_n]$, respectively. Then $f_{true}(x_l, \alpha) = \mathbf{a}$ and $\hat{f}_{proj}(y_l, \alpha) = \mathbf{b}$. In that sense, M and $\mathbf{b}$ are known, while $\mathbf{a}$ is unknown, being an inverse problem and it is well-posed if satisfies the requirements of existence, stability and uniqueness of its solutions (no errors in the variable that we can measure). As we try with different uniform grids for $\hat{f}_{proj}(y, \alpha)$ we conclude to use $n = 2048$ because trace with higher precision the original data and don't spend a lot of computational time. The least square solution for the eq. 3.7 system is a solution of

$$\min\{||\mathbf{b} - M\mathbf{a}||^2\}, \tag{3.8}$$

however, in many areas of sciences like spectroscopy, seismography, medical images, among others (Bertero et al., 1988; Scales & Gersztenkorn, 1999; Natterer & Wübbeling, 2001), the data are obtained and interpreted as a convolution from a noisy signal with a detector. In that way, the error is always presented in the Fredholm integral equation ($f_{proj}(y, \alpha) \rightarrow f_{proj,0}(y, \alpha) + \Theta(y)$), and this reads as

$$f_{proj,0}(y, \alpha) + \Theta(y) = c_\alpha \int_y^\infty \frac{y^{1+\alpha}}{x^{1+\alpha}\sqrt{x^2 - y^2}} f_{true}(x, \alpha) dx, \tag{3.9}$$

where $f_{proj,0}(y, \alpha) + \Theta(y)$ is the measured projected rotational velocity, $f_{proj,real}(y, \alpha)$ is the real projected rotational velocity and $\Theta(y)$ represents the unknown noise. Since the observed data are obtained with an error of measure, eq. 3.8 is an example of a discrete ill-posed problem, i.e., small errors in the measured data can produce large variations in the recovered function which make the solution unstable (Ivanov et al., 2002).

3.2.3 Deconvolution via Tikhonov regularization

In order to obtain the vector of interest $\mathbf{b}$, i.e., the discrete true rotational velocity distribution, we make use of the Tikhonov regularization method, which is a robust minimization process that includes a regularization via a λ parameter, called the Tikhonov factor. This process is a regularization method that allows an increase in numerical stability and take into account the intrinsic error for observations. This new minimization process is described by

$$\min\{||\mathbf{b} - M\mathbf{a}||^2\} \rightarrow \min\{||\mathbf{b} - M\mathbf{a}||^2 + \lambda^2||I(\mathbf{a} - \mathbf{a}_0)||^2\}, \tag{3.10}$$

where I is the identity matrix and $\mathbf{a}_0$ is an initial estimation, setting $\mathbf{a}_0 = 0$ when there is no previous information. Once the λ value is attained (explained in next subsection), the solution $\mathbf{a}_\lambda$ of the regularized problem by the Tikhonov method is given analytically by

$$\mathbf{a}_\lambda = (M^T M + \lambda^2 I)^{-1} M^T \mathbf{b}. \tag{3.11}$$

Regularization methods, and in our case, the Tikhonov regularization (Tikhonov, 1943; Tikhonov, 1963; Tikhonov & Arsenin, 1977) has been useful in multiple applications as image processing, geophysics, machine learning, among others (Bouhamidi & Jbilou, 2007; Fomel, 2007; Hansen, 2010; Deng et al., 2013).

3.2.4 Regularization parameter

To obtain $\mathbf{a}_\lambda$ in eq. 3.11 there is necessary to first compute the Tikhonov factor. These methods use a Singular Value Decomposition for M and are fully described in Hansen (2007) and Hansen (2010).

We tried to use the L-curve (explained below) to obtain the regularization parameter but this method failed. Explaining briefly this, it is proposed through regularization schemes which seek to make a balance between the size of the regularized solution (or the difference between it and a known solution) and the quality of the fit given by the data. A difficult problem is to find the regularization parameter, this is because almost all strategies require some prior knowledge of the problem and the solution. The method to select the regularization parameter that we intend to study is based on the graph of the norm of the regularized solution versus the corresponding norm of the residual, whose shape reveals an "L". The corner criterion of the L-curve proposes, for the selection of the regularization parameter is to use the "L" shape of the graph of the curve, and locate the corner of said "L". The inconvenient of this, in general, is that knowing the corner of the curve is a great difficult, since the location of the corner of the L-curve depends on the scale with which it is plotted. We could not obtain the "L" shape on the L-curve plot, but only the horizontal part of it was successful. Christen et al. (2016) reviews these concepts and in this work they have the same difficulty to find the "L" shape, showed in Fig. 3.2.

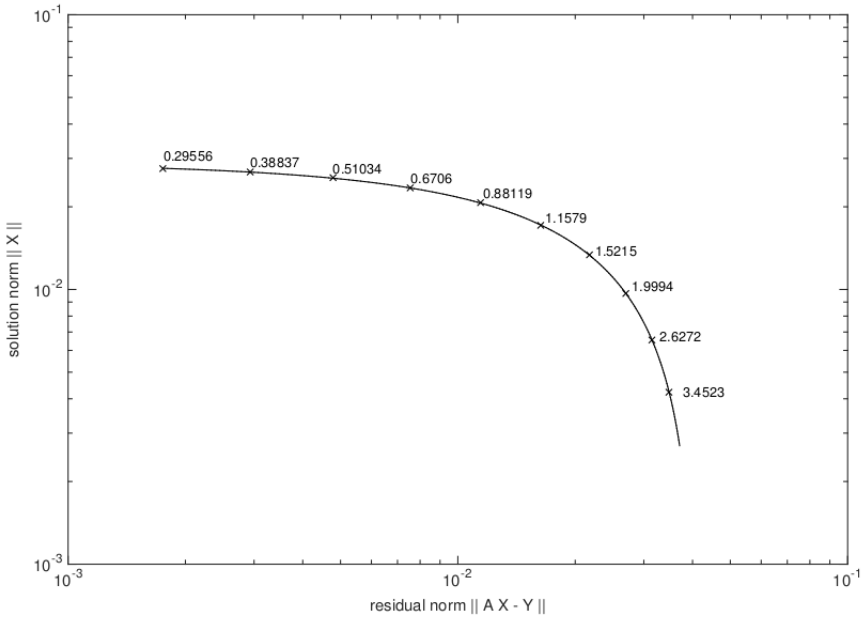

Figure 3.2: Residuals of the regularization $||A\mathbf{X}_\lambda - \mathbf{Y}||$ (our notation: $||M\mathbf{a}_\lambda - \mathbf{b}||$) versus the norm of the regularization $||\mathbf{X}_\lambda||$ (our notation: $||\mathbf{a}_\lambda||$), both in logarithm scale. Tikhonov parameter value λ is over plotted in the curve and only the horizontal part of the "L" shape is shown. *Credit*: Christen et al. (2016)

That is why we make use of an unbiased and consistent (desirable properties of any statistical estimator) way to obtain the Tikhonov factor, proposed by Christen et al. (2016). This is an iterative procedure, fast and efficient to obtain the regularization parameter for smooth solution. The step-by-step procedure is the following:

(i) We start with an initial value of λ (in this work with $\lambda_0 = 0.1$),

(ii) In each following iteration we reduce the value of λ by a factor 0.99 ($\lambda_m = 0.99^m \lambda_0$),

(iii) At iteration step m we calculate the difference between the corresponding regularization solutions: $\delta = ||\mathbf{a}_{\lambda_m} - \mathbf{a}_{\lambda_{m-1}}||^2$,

(iv) If δ is small enough, that is, $\delta \leq 10^{-8}$, we stop the iterative process and obtain the value of λ.

From that procedure, for a fix $\alpha = \alpha_{theo}$, we obtain the true rotational velocities PDF $\mathbf{a}_\lambda$ from a deconvolution via Tikhonov regularization from $\hat{f}_{proj}(y, \alpha_{theo})$. The continuous form is defined by $\hat{f}_{true}(x, \alpha_{theo})$.

All the calculations of regularization were made with the MATLAB package for analysis and solution of discrete ill-posed problems, call it Regularization Tools Version 4.1[3] developed by Hansen (2007). Other methods such as Generalized Cross-Validation, Discrepancy Principle, Restricted Maximum Likelihood and L-curve methods are also available in this package.

3.2.5 Optimal α

Having $\hat{f}_{true}(x, \alpha_{theo})$, from a regularization of $\hat{f}_{proj}(y, \alpha_{theo})$, and implementing the α parameter in the kernel of the Fredholm integral (α_{ker}) there is possible to compute a new PDF solution for the projected rotational velocities $\bar{f}_{proj}(x, \alpha_{theo}, \alpha_{ker})$. The Fredholm integral now reads:

$$\bar{f}_{proj}(y, \alpha_{theo}, \alpha_{ker}) = c_{\alpha_{theo}} \int_y^\infty \frac{y^{1+\alpha_{ker}}}{x^{1+\alpha_{ker}}\sqrt{x^2 - y^2}} \hat{f}_{true}(x, \alpha_{theo}) dx, \tag{3.12}$$

the α_{ker} is given by a grid of values that gives new PDF solutions and to compare with the original non-parametric PDF $\hat{f}_{proj}(y, \alpha_{theo})$ a Mean Square Error (MSE), $MSE(\alpha_{theo}, \alpha_{ker})$), is computed by

[3] `http://www.imm.dtu.dk/~pcha/Regutools/`

$$MSE(\alpha_{theo}, \alpha_{ker}) = \frac{1}{n}\sum_{l=1}^{n}\left(\hat{f}_{proj}(y_l, \alpha_{theo}) - \bar{f}_{proj}(y_l, \alpha_{theo}, \alpha_{ker})\right)^2, \tag{3.13}$$

that is, for a fix α_{theo}, it compares the two projected rotational velocities PDFs for a grid of α_{ker} and the minimal value of $MSE(\alpha_{theo}, \alpha_{ker})$ yields the best α parameter for each sample ($= \alpha_{min}$); this α_{min} should be very similar to α_{theo}, however, we show via Monte Carlo simulation (Chapter 3.3) that this is not always the case.

The Fredholm integral and MSE are calculated via Wolfram Mathematica (Inc., 2020). The connection with between Mathematica and MATLAB is effectuated via MATLink[4], which is an application for seamless two-way communication and data transfer.

3.2.6 Summary of the algorithm

The whole algorithm in which the spin alignment of the database coming from a cluster or field stars is displayed in Fig. 3.3.

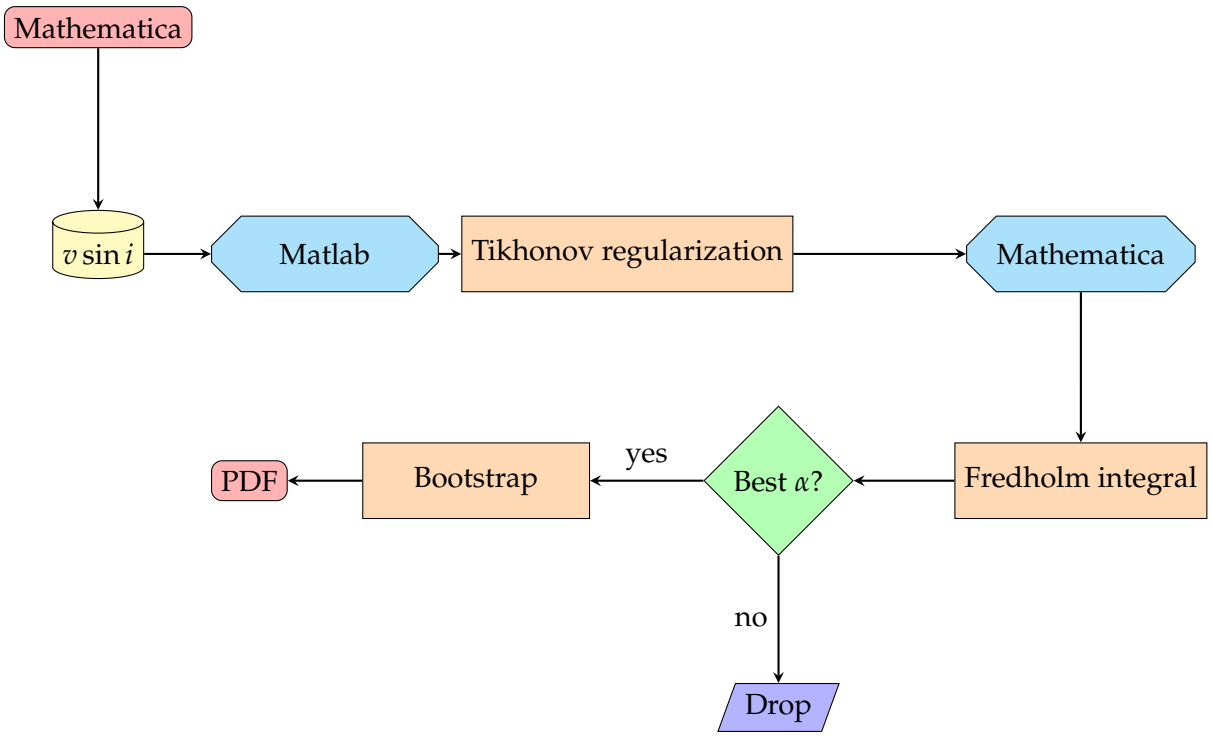

Figure 3.3: Flowchart to obtain α_{min} for a database of stars with their $v \sin i$ value.

[4] http://matlink.org/

3.3 Summary

To measure $v \sin i$ in the BeSOS spectral database, first it is necessary to fit a Gaussian profile in one or more absorption lines and then select automatically an amount of the signal to proceed to compute the FT. Since not all spectra have low S/N ratio, in each line five criteria are presented: 1) A Gaussian profile is successfully performed, 2) The observed line profile is in absorption and is below the continuum level, i.e., $G_{fit}(\lambda = \lambda_{fit}, \lambda_{fit}, \sigma_{fit}, A_{fit}) < 1$, 3) The center of the Gaussian fit is not shifted more than $3\sigma_{fit}$ with respect to λ_{theo}, i.e., $\lambda_{fit} < |\lambda_{theo} \pm 3\sigma_{fit}|$, 4) The standard deviation of the continuum) is lesser than the amplitude of the Gaussian fit, i.e., $\sigma_c < A_{fit}$, and 5) The dispersion of the Gaussian fit is higher than 5 times the step of the wavelength, i.e., $\sigma_{fit} > 5\Delta\lambda$.

How is distributed v from a $v \sin i$ sample of rotating stars is presented in this chapter. Using $v \sin i$ data, a KDE is computed and then a regularization via Tikhonov regularization is calculated using a non-isotropic distribution of axes in the kernel of the Fredholm integral. The Tikhonov factor is obtained with same procedure of (Christen et al., 2016). The best non-isotropy parameter is computed with a MSE between the KDE of $v \sin i$ and the solution of the Fredholm integral with a PDF of v from the Tikhonov regularization.

CHAPTER 4

Monte Carlo simulations

We show in this chapter our Monte Carlo (MC) simulations: the random sampling for theoretical rotational velocities (section 4.1) and the non-isotropic $v \sin i$ generator (section 4.2). The first is about the construction for absorption line profiles at different noise and velocities, and the second is the complete solution of the Fredholm integral equation for samples of $v \sin i$ data given by an unimodal and a bimodal Maxwellian distributions.

4.1 Random sampling for theoretical rotational velocities

To evaluate the consistent of the method for random sampling, we constructed theoretical line profiles rotationally convolved at different noise levels and test the developed method to find the $v \sin i$ value.

4.1.1 Rotationally convolved absorption lines

Assuming that the intrinsic line profile of a star can be modeled by a Gaussian distribution, we performed a theoretical rotating line profile with fixed center at 4480 $\AA$, a dispersion of 0.1 $\AA$ and an amplitude of 0.5. This theoretical line represents $H(v)$ in eq.

2.8. Now, a rotational kernel $G(v_z)$ for a theoretical velocity $\langle v \sin i \rangle_{theo} = 150\ (km\ s^{-1})$ is convolved with $H(v)$, yielding a theoretical line profile $D(v)$ in Fig. 4.1 without noise (symbol $\langle \bullet \rangle$ is just a notation).

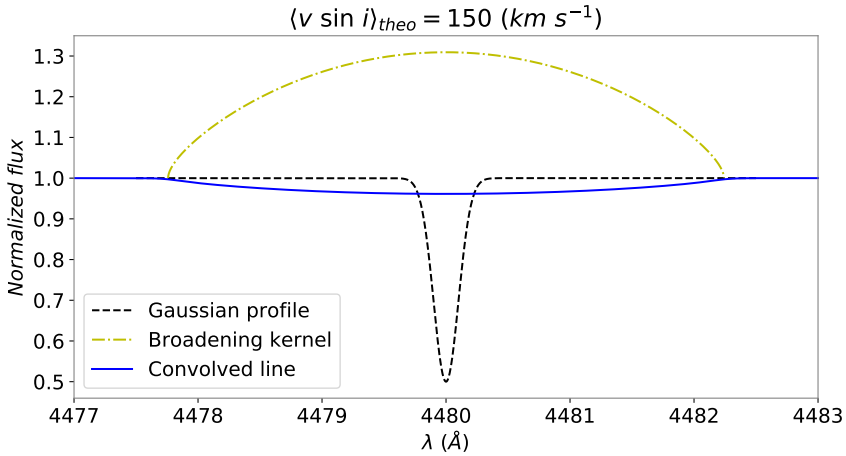

Figure 4.1: Construction of a theoretical line profile, represented by the blue curve. This line is a convolution between a rotating broadening kernel, represented by the yellow dot-dashed curve, and the intrinsic line profile of the star, denoted by the black dashed curve. $\langle v \sin i \rangle_{theo} = 150\ (km\ s^{-1})$.

In order to study the effects of rotation over the shape of the line profile, Fig. 4.2 shows the Doppler broadening and trace the amplitude for each velocity: $\langle v \sin i \rangle_{theo} = 100$, 150, 200, 250, 300, 350, 400, 450 and 500 $(km\ s^{-1})$.

An important aspect to take into account is the shape of the signal simulated for the velocity imposed, being the equivalent width conserved for each velocity. As the rotational velocity increases, the rotationally convolved line becomes weaker and wider, this can be seen in the outcome amplitudes represented by the value of A_{fit}. The probability to perform a successful fit is higher for lower velocities.

4.1.2 Simulating line profiles with noise

In the practice it is usual to observe systematic variations due to instrumental error, physical effects, among others. We simulated the effect by adding a pseudo-random noise (or error) from a Gaussian distribution where the error is parameterized by the parameter σ_{noise}, i.e., the dispersion of the distribution. It is expected that for higher noise, the spectrum shows more variation in the normalized flux. A visualization at

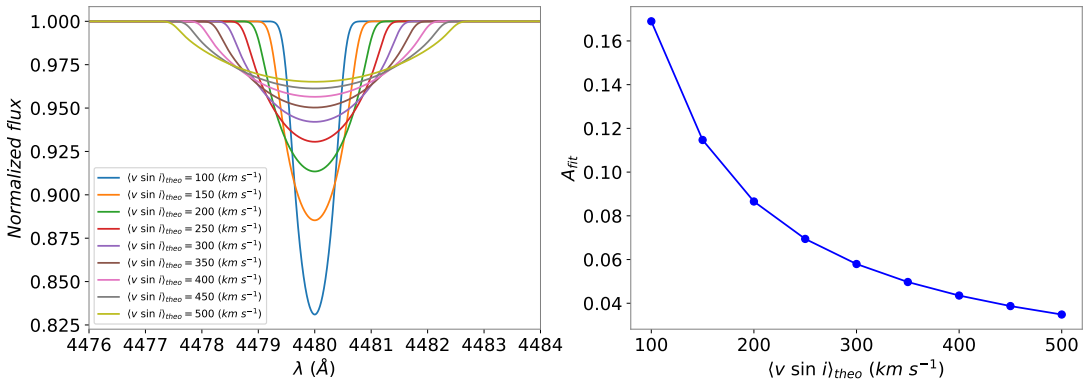

Figure 4.2: Left panel: Theoretical line profiles convolved with different rotational kernels. Right panel: Amplitude of the rotational convolved line profiles as a function of $\langle v \sin i \rangle_{theo}$.

the same scale is displayed in the Fig. 4.3 for combinations of $\sigma_{noise} = 0.001$, 0.005 and 0.01, $\langle v \sin i \rangle_{theo} = 200$, 300 and 400 $(km\ s^{-1})$, for a step in wavelength of $\Delta\lambda = 0.089\ (\AA)$, same as BeSOS spectra.

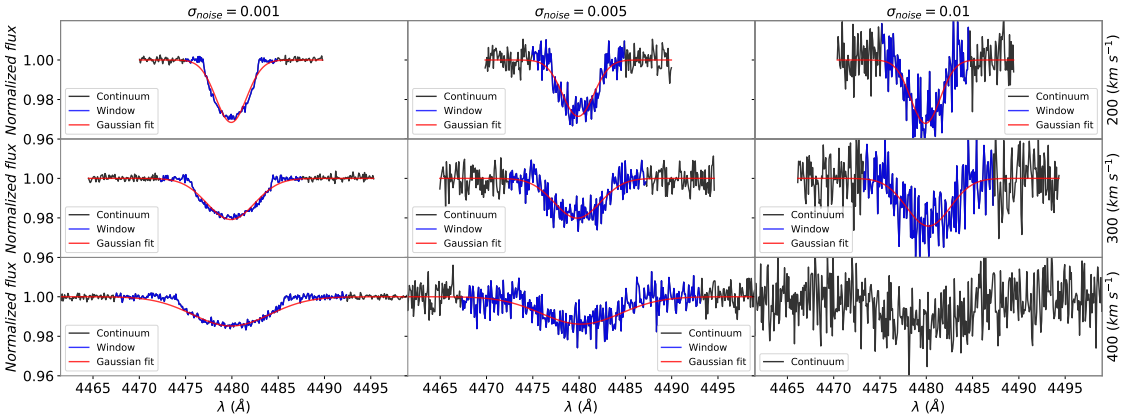

Figure 4.3: Grid of rotational theoretical line profiles with noise added. The red curve represent the best Gaussian fit with a dispersion parameter of σ_{fit}, where the blue curve is the signal window of $\pm 3\sigma_{fit}$ with respect to λ_{fit} and the black solid line is the continuum, represented for each side for $3\sigma_{fit}$. Left panels: $\sigma_{noise} = 0.001$. Middle panels: $\sigma_{noise} = 0.005$. Right panels: $\sigma_{noise} = 0.01$. Top panels: lines rotationally convolved with $\langle v \sin i \rangle_{theo} = 200\ (km\ s^{-1})$. Middle panels: lines convolved with $\langle v \sin i \rangle_{theo} = 300\ (km\ s^{-1})$. Bottom panels: lines rotationally convolved with $\langle v \sin i \rangle_{theo} = 400\ (km\ s^{-1})$.

In Fig. 4.3 we can see that the higher is the noise, the line profile is more difficult to detect and even more at high rotational speeds as can be seeing in Fig. 4.2. Following the procedure of flowchart Fig. 3.1, when the initial parameters from the optimal Gaussian profile do not find the spectral line, the profile is dropped, as the line profile with $\langle v\ \sin\ i\rangle_{theo} = 400\ (km\ s^{-1})$ and $\sigma_{noise} = 0.01$ is shown in Fig. 4.3. The continuum for each line is defined as the signal which does not comes from the line, this means that if the signal of the line profile is defined by a window of $\pm\sigma_{fit}$ (with respect to the midwave) the remainder spectrum (in both sides) is established as the continuum. With this continuum we can obtain the standard deviation σ_c, which is defined as the noise. However, we noted that the selected line profile must satisfy our five criteria to be a "good" line, then our proposal of five criterias is performed to obtain the projected rotational velocity. If one criteria is not satisfied, then the line is not taking into account. Finally, having the spectral window of the observed line profile limited by $\pm 3\sigma_{fit}$ with respect to λ_{fit}, we calculated the FT to obtain the domain of the frequencies and then the value of the projected stellar rotational velocity. To see how is the behavior of $g(\nu)$, Fig. 4.4 shows where is the first zero of the function, giving the projected rotational value of $\langle v\ \sin\ i\rangle_{FT}$ for each normalized line profile of Fig. 4.3.

It is expected that the noise added to the spectrum will produce an error in the determination of the projected rotational speed. Another issue that is necessary to take into account is the window which is giving in the FT. Fig. 4.5 describes the size windows of $2\sigma_{fit}$, $2.5\sigma_{fit}$ and $3\sigma_{fit}$ for the specific case of $\langle v\ \sin\ i\rangle_{theo} = 300\ (km\ s^{-1})$ and $\sigma_{noise} = 0.005$ for these three different windows. Evidently there is no clear pattern for the size of the window and the respective velocity that yields.

4.1.3 Simulated grid of velocities and noise added to the spectrum

To see if there is a behavior for random sampling we simulated 10000 MC samples for a grid of lines of $\langle v\ \sin\ i\rangle_{theo} = 200$, 300 and 400 $(km\ s^{-1})$, $\sigma_{noise} = 0.001$ to 0.01 in steps of 0.001, and windows of $2\sigma_{fit}$, $2.5\sigma_{fit}$ and $3\sigma_{fit}$. Figs. 4.6, 4.7 and 4.8 shows the evolution for the number of successfully fits, the percentiles 2.5%-50%-97.5% of $\langle v\ \sin 1\rangle_{FT}$ and σ_c as a function of σ_{noise}, respectively.

Number of successfully fits, so far, are defined as Gaussian profiles that were performed with a favorable result for the five criterias as "good" lines. As a first discussion it was predicted that for lower rotations number of lines that satisfy all five

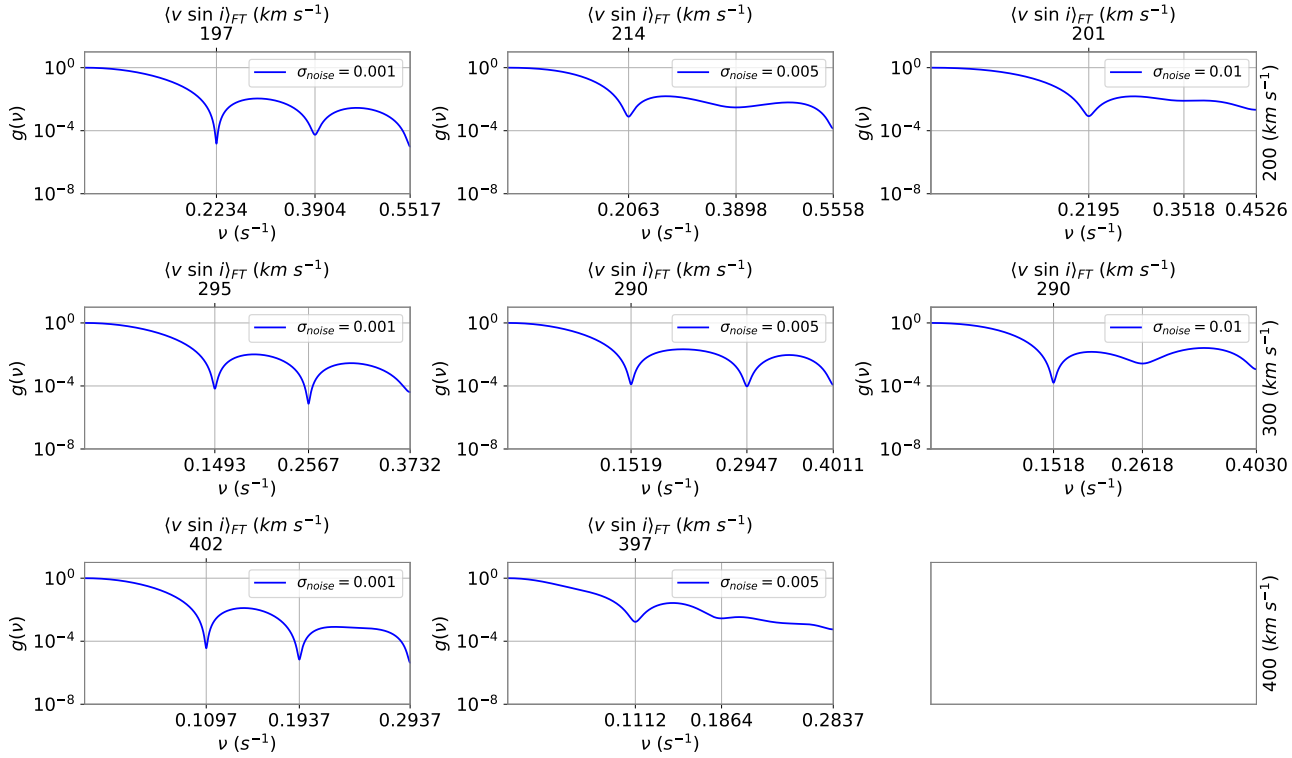

Figure 4.4: Rotational kernel $g(\nu)$ as a function of ν and their conversion for the first zero of the velocity obtained. Left panels: $\sigma_{noise} = 0.001$. Middle panles: $\sigma_{noise} = 0.005$. Right panels: $\sigma_{noise} = 0.01$. Top panels: lines rotationally convolved with $\langle v \ \sin \ i \rangle_{theo} = 200 \ (km \ s^{-1})$. Middle panels: lines convolved with $\langle v \ \sin \ i \rangle_{theo} = 300 \ (km \ s^{-1})$. Bottom panels: lines rotationally convolved with $\langle v \ \sin \ i \rangle_{theo} = 400 \ (km \ s^{-1})$. For the case of $\sigma_{noise} = 0.01$ and $\langle v \ \sin \ i \rangle_{theo} = 400 \ (km \ s^{-1})$ no FT is calculated because the respective absorption line profile do not satisfied the five criteria.

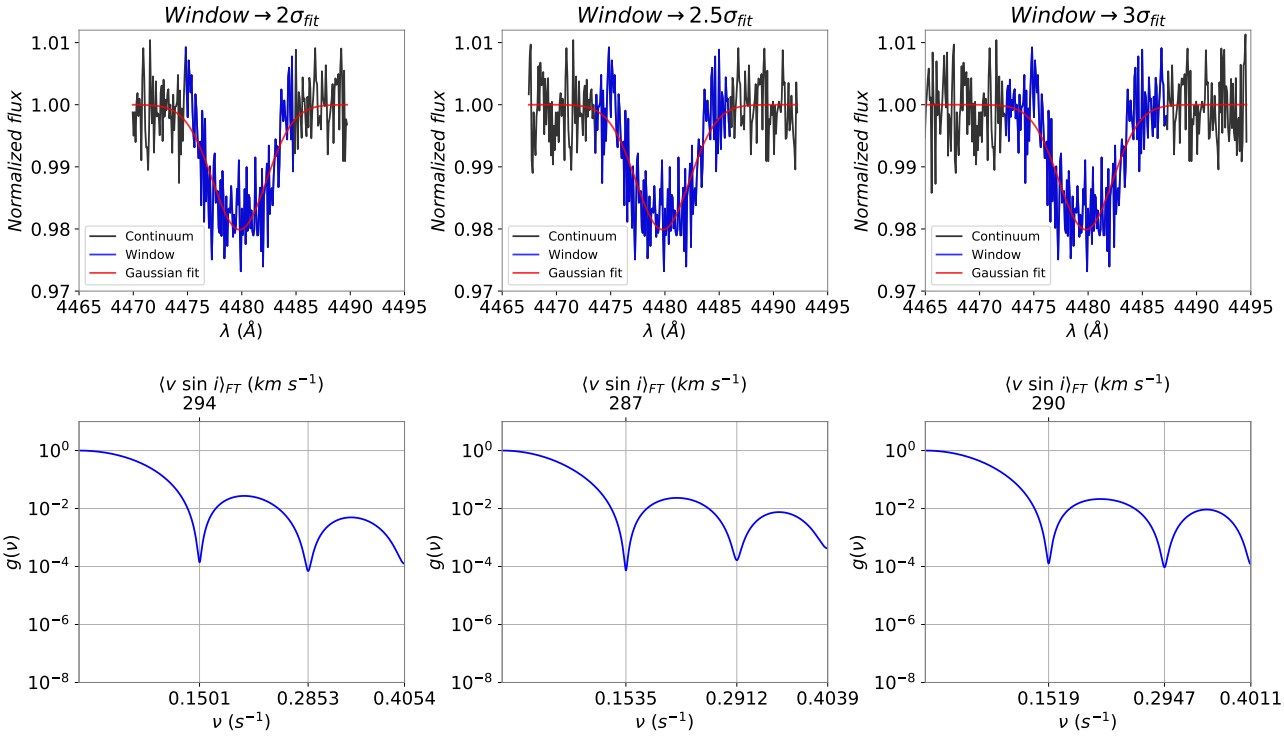

Figure 4.5: FT (bottom panels) for the normalized line profiles (top panels) where the signal is selected by windows of $2\sigma_{fit}$ (left panels), $2.5\sigma_{fit}$ (middle panels) and $3\sigma_{fit}$ (right panels).

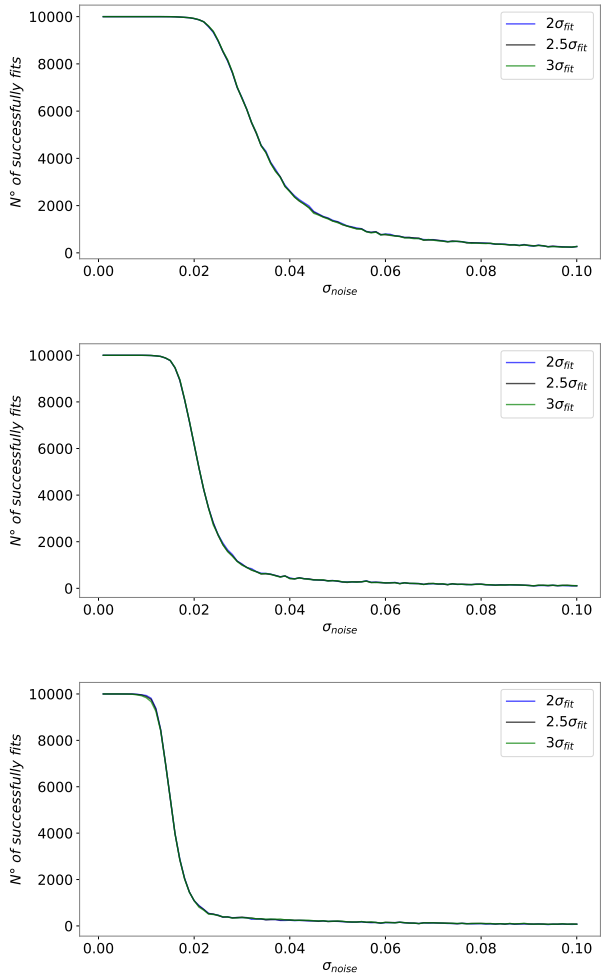

Figure 4.6: Number of successfully fits as a function of the theoretical noise added. The theoretical velocity of the rotational kernels are 200 $(km\ s^{-1})$, 300 $(km\ s^{-1})$ and 400 $(km\ s^{-1})$ for top, middle and bottom panels, respectively. The window of the signal are represented by $2\sigma_{fit}$ (blue), $2.5\sigma_{fit}$ (black) and $3\sigma_{fit}$ (green).

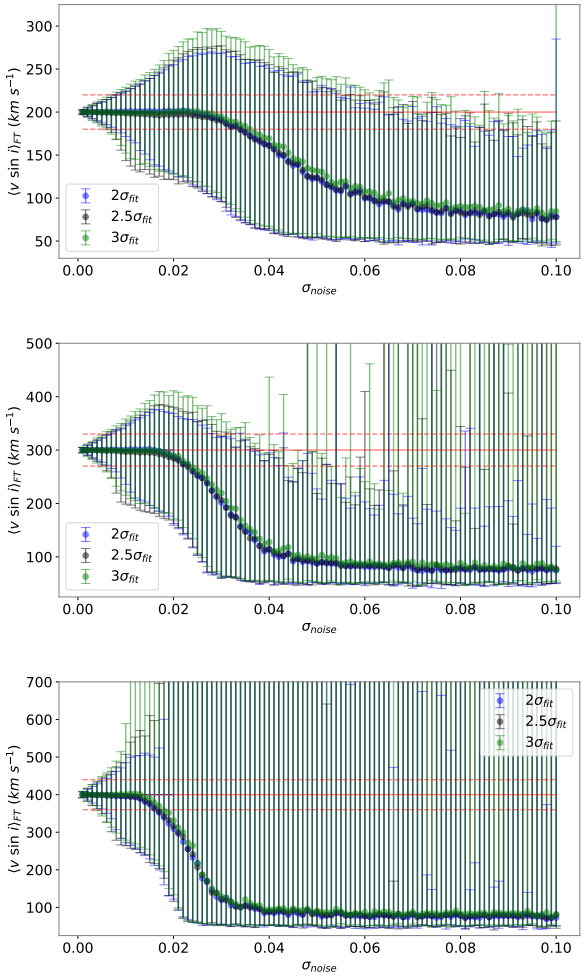

Figure 4.7: Median of the $\langle v \sin i \rangle_{FT}$ with their confidence intervals of 2.5% and 97.5% (error bars) as a function of σ_{noise}, the red line represent the respective $\langle v \sin i \rangle_{theo}$ and the red dashed line their $\pm 10\%$ values. The theoretical velocity of the rotational kernels are 200 $(km\ s^{-1})$, 300 $(km\ s^{-1})$ and 400 $(km\ s^{-1})$ for top, middle and bottom panels, respectively. The window of the signal are represented by $2\sigma_{fit}$ (blue), $2.5\sigma_{fit}$ (black) and $3\sigma_{fit}$ (green).

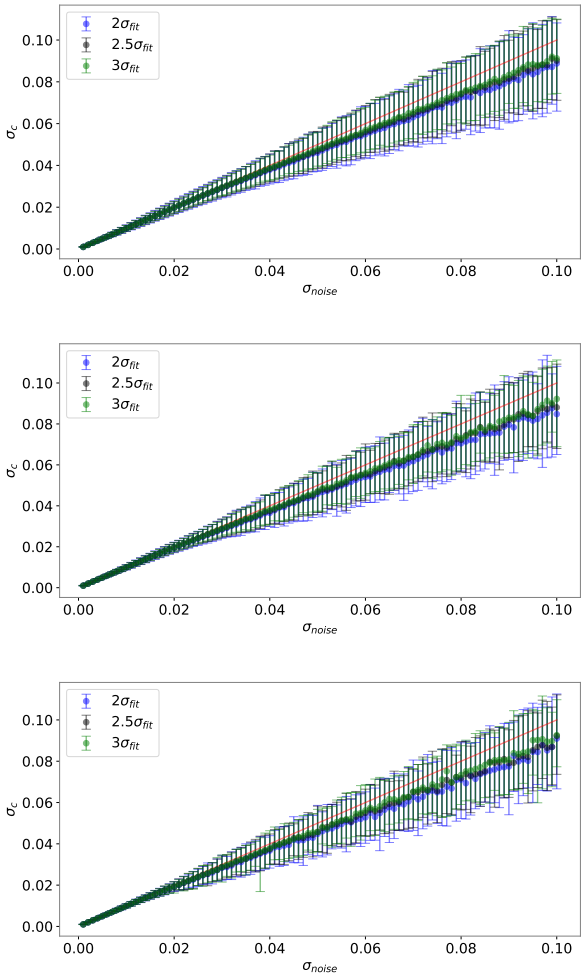

Figure 4.8: Standard deviation of the continuum as a function of the theoretical noise added, the 1:1 relation is represented by a red line. The theoretical velocity of the rotational kernels are 200 $(km\ s^{-1})$, 300 $(km\ s^{-1})$ and 400 $(km\ s^{-1})$ for top, middle and bottom panels, respectively. The window of the signal are represented by $2\sigma_{fit}$ (blue), $2.5\sigma_{fit}$ (black) and $3\sigma_{fit}$ (green).

criteria is higher, and clearly, this is reflected in Fig. 4.6 because the curve of successful fits starts to decay at lower σ_{noise} for lower rotational velocities. Furthermore, the error bars of 2.5% and 97.5% of the velocities obtained via FT $\langle v \sin i \rangle_{FT}$ are also displayed as a function of σ_{noise}. The importance here is that when the median value of $\langle v \sin i \rangle_{FT}$ for the 10000 repetitions is under/above the 10% of $\langle v \sin i \rangle_{theo}$ our method is no reliable at a certain σ_{noise} so far (when this limit happen, $\sigma_{noise,crit}$ is defined). Finally, σ_{noise} is a noise imposed to our spectral lines simulations and the relation 1:1 with respect to σ_c demonstrate that are well correlated. This means that measuring the standard deviation of the continuum it is possible to relate observations with simulations.

Performing a complete study of at what σ_{noise} (or σ_c) it is possible to get trusty measurement, denoted by $\sigma_{noise,crit}$ (or $\sigma_{c,crit}$). Fig. 4.9 describes the pattern for a grid of different rotational velocities (100 to 600 in steps of 10 $km\ s^{-1}$), added noise (0.001 to 0.01 in steps of 0.001) and the usually three ($2\sigma_{fit}$, $2.5\sigma_{fit}$ and $3\sigma_{fit}$).

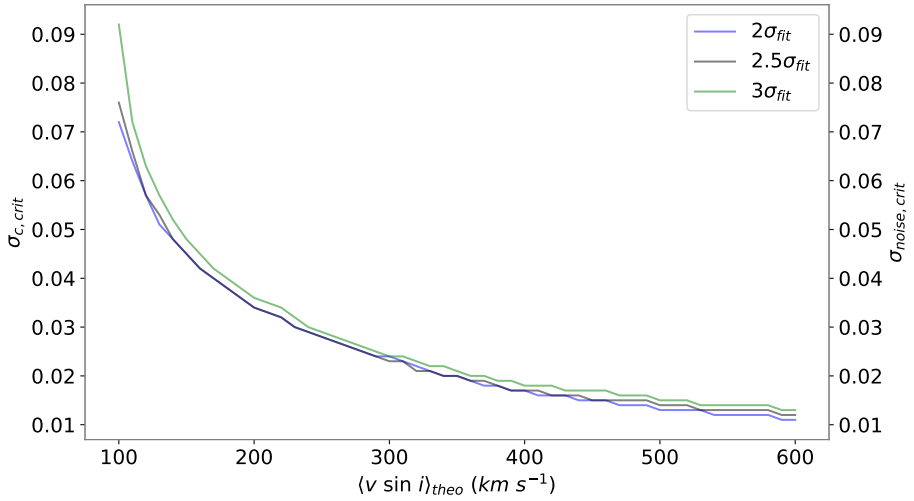

Figure 4.9: Critical standard deviation of the continuum in observations $\sigma_{c,crit}$ (or $\sigma_{noise,crit}$ in simulations) to obtain $v \sin i$. The window of the signal is represented by $2\sigma_{fit}$ (blue), $2.5\sigma_{fit}$ (black) and $3\sigma_{fit}$ (green).

When the median of $\langle v \sin i \rangle_{FT}$ is above/under the 10% of $\langle v \sin i \rangle_{theo}$, then the value of σ_{noise} (or σ_c) is preserve as $\sigma_{noise,crit}$ (or $\sigma_{c,crit}$). Having the previous five criterias to select an absorption line profiles, now a 6th criteria is added considering this last relationship. It is possible to constrain the observations with their observable σ_c, this

means that if the value is higher than the one showed by the curve, it is considered as a line with appreciable noise (bad spectrum) and therefore is not considered as a good line. Using this new criteria it is possible to know the dispersion of velocities obtained using HeI lines in Be stars or our sample.

4.2 Non-isotropic $v \sin i$ generator

We have described the mathematical model and the numerical algorithm and procedures to find the best α value that describe a non-sphericity for a database of rotational speed of stars (open clusters or field stars). In this section, we create synthetic samples with different theoretical α values and equatorial rotational velocity distributions to constrain and analyze the consistent by our method.

4.2.1 Maxwellian distribution

The original Maxwell-Boltzmann distribution was found to describe the particle speeds in idealized gases, where these gaseous particles (atoms or molecules) do not interact between them. For further information of this distribution visit Rowlinson (2005). Conversely, in the context of stellar rotation, this is traduced as the dispersion in the equatorial rotational velocities (Deutsch, 1970). In our simulations, two different distributions of true rotational velocities are performed: two unimodal Maxwellian and a bimodal Maxwellian distribution. We assume an unimodal Maxwellian distribution ($UniMax$) as

$$UniMax(x,\sigma) = \sqrt{\frac{2}{\pi}} e^{-\frac{x^2}{2\sigma^2}} x^2/\sigma^3, \tag{4.1}$$

for $x > 0$, being σ the dispersion parameter. We simulate two different true rotational velocity distributions, one for $\sigma = 16\ km\ s^{-1}$ (slow rotators) and another for $\sigma = 150\ km\ s^{-1}$ (fast rotators).

Now, a bimodal Maxwellian distribution is defined by

$$BiMax(C_1,C_2,\sigma_1,\sigma_2,x) = \frac{C_1}{C_1+C_2}\left(\sqrt{\frac{2}{\pi}} e^{-\frac{x^2}{2\sigma_1^2}} x^2/\sigma_1^3\right) + \frac{C_2}{C_1+C_2}\left(\sqrt{\frac{2}{\pi}} e^{-\frac{x^2}{2\sigma_2^2}} x^2/\sigma_2^3\right), \tag{4.2}$$

where $C_1 = C_2 = 0.5$ are statistical weights, and $\sigma_1 = 170\ km\ s^{-1}$ and $\sigma_2 = 60\ km\ s^{-1}$ are the dispersion velocity parameters, very similar parameters obtained in a bimodal

Maxwellian fit to an open cluster of Ramírez-Agudelo et al. (2013).

4.2.2 Inclination angles

Measured rotational velocities have apparent component given by $\sin i$ and it is necessary to simulate this angle distribution i as a function of α which is given by the following equation

$$i(\alpha) = \arcsin\left(c_\alpha \frac{r^{1+2\alpha}}{\sqrt{1-r^2}}\right), \tag{4.3}$$

where r is the random variate generator for inclination angles given by an uniform distribution $[0, 1]$.

The initial database is constructed by $v \sin i(\alpha)$ for a grid of α_{theo} which starts at -0.5 and finish at 2, in steps of 0.1, being a total 26 α_{theo} values (each sample with length equal to 200). Finally, 100 MC repetitions are performed for each grid of α_{theo} of 200 samples for two different σ (16 and 150; $km\ s^{-1}$).

4.2.3 Deconvolution

In order to compute the Tikhonov regularization method to each sample of $v \sin i(\alpha)$, Fig. 4.10 shows the regularization parameter λ as a function of α_{theo}.

As can be appreciated in this figure, the regularization parameter increase significantly for $\alpha_{theo} < 0.5$ and for higher values, λ starts to be almost constant. Note that λ is a small number. This is more evident for $\sigma = 16\ km\ s^{-1}$ than for $\sigma = 150\ km\ s^{-1}$. It is important to mention that the shaded areas represent the quantiles 0.025 (lower) to 0.975 (upper) or 95% confidence intervals.

Subsequently the KDE for $v \sin i(\alpha)$ and the deconvolution is displayed in Fig. 4.11 and 4.12, for slow and fast rotators respectively and for four α_{theo} (-0.5, 0, 0.5 and 2). As expected, for lower α_{theo}, $\hat{f}_{proj}(v \sin i, \alpha_{theo})$ shows higher a probability to obtain lower values of $v \sin i$. The analytical solution of the Maxwell distribution should be claimed similar to $\hat{f}_{true}(v, \alpha_{theo})$ for any α_{theo}. Another important aspect to mention is that for $\alpha_{theo} = 2$, the KDE and the deconvolved PDF are very similar. The reason is because as α_{theo} increases and λ remains constant, then the Tikhonov regularization parameter reach the upper limit and the deconvolved PDFs do not change for high α_{theo}.

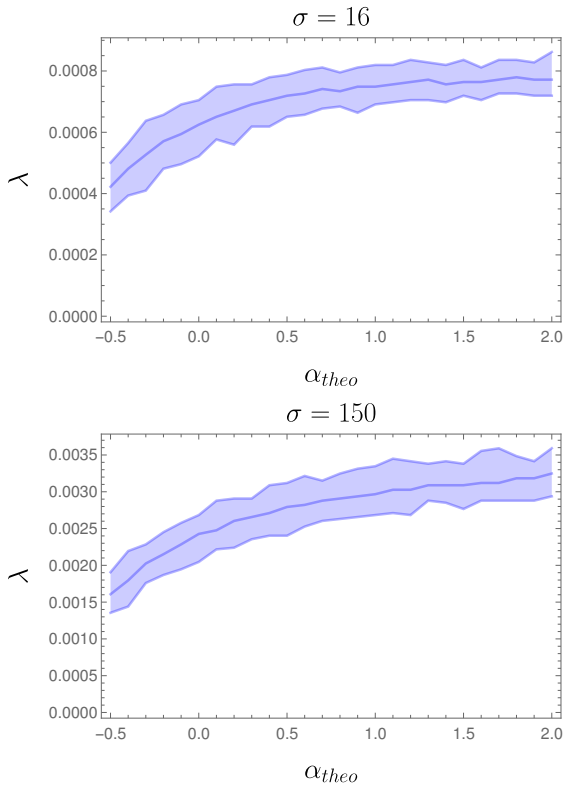

Figure 4.10: Regularization parameter as a function of the theoretical α for 100 MC repetitions for each sample of length 200. The dashed area represent the quantiles 0.025 (lower) to 0.975 (upper). Unimodal Maxwellian distribution with $\sigma = 16\ km\ s^{-1}$ (upper panel) and $\sigma = 150\ km\ s^{-1}$ (bottom panel).

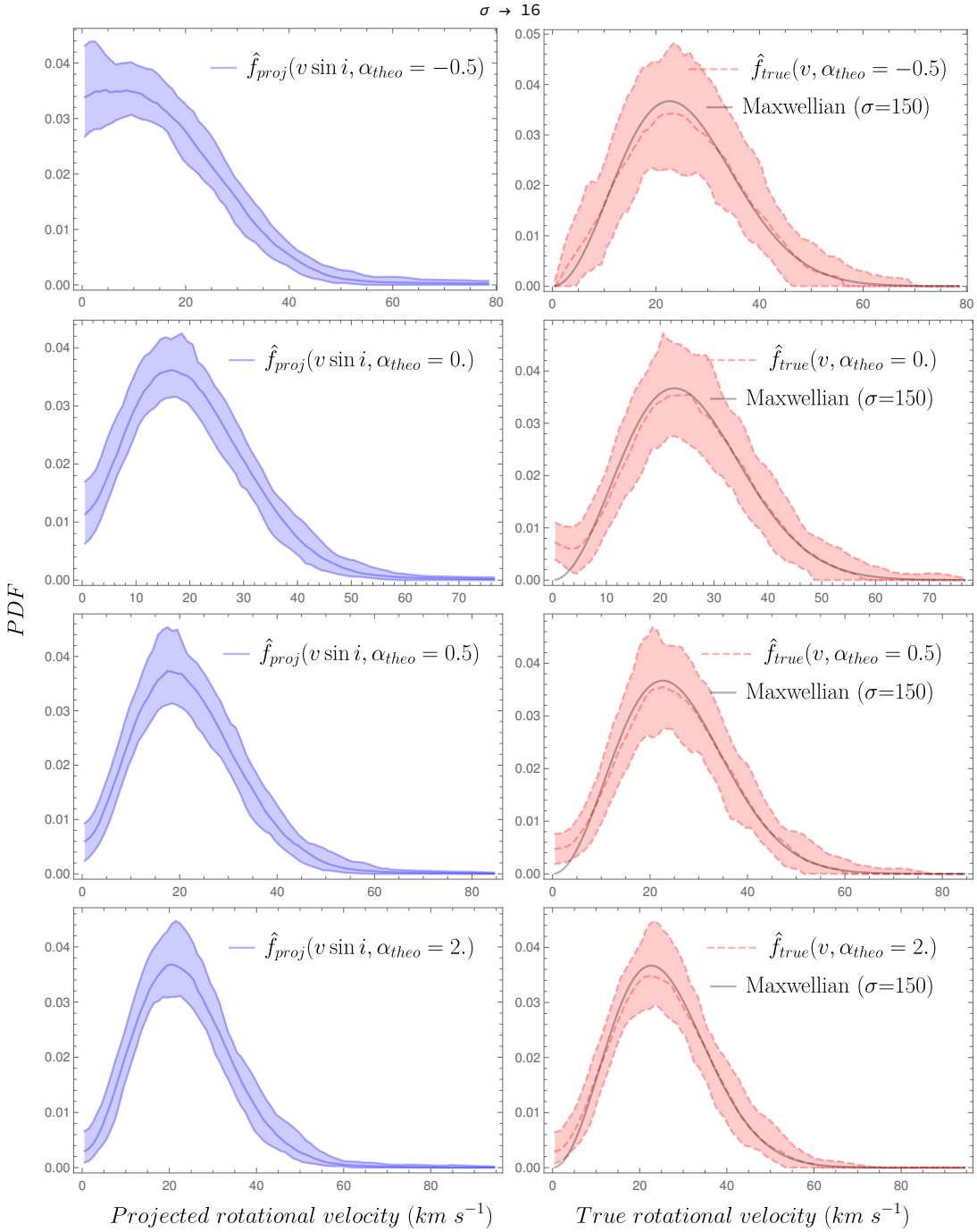

Figure 4.11: Kernel density estimator for the projected rotational velocities represented by the blue curves (left panels) and the deconvolution via Tikhonov regularization represented by the red dashed line with the respective analytical Maxwell solution with the black curve (right panels). The solutions are for $\alpha_{theo} = -0.5$ (first row), $\alpha_{theo} = 0$ (second row), $\alpha_{theo} = 0.5$ (third row) and $\alpha_{theo} = 2$ (fourth row). The dashed area represent the quantiles 0.025 (lower) to 0.975 (upper). Unimodal Maxwellian distribution with $\sigma = 16\ km\ s^{-1}$.

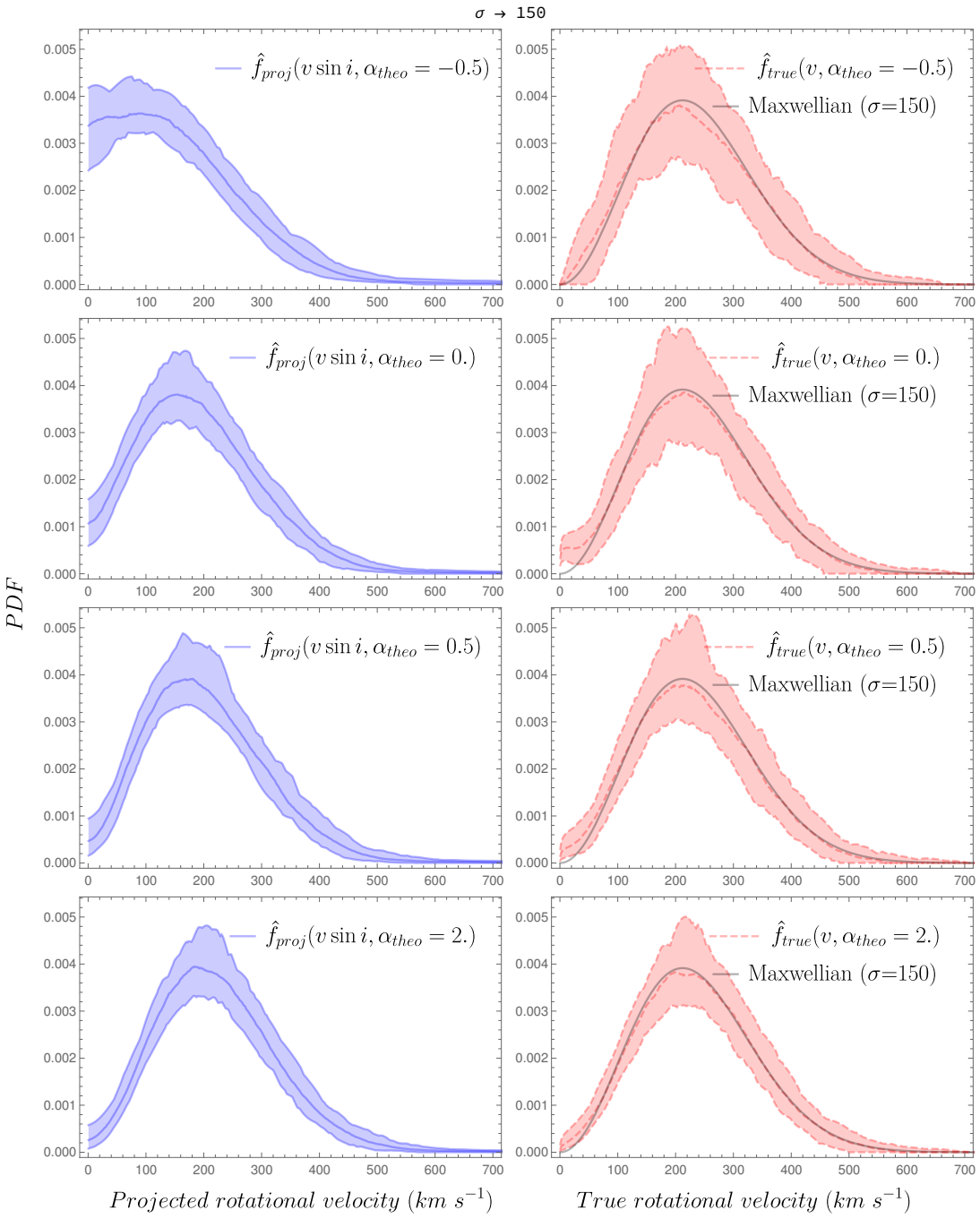

Figure 4.12: Kernel density estimator for the projected rotational velocities represented by the blue curves (left panels) and the deconvolution via Tikhonov regularization represented by the red dashed line with the respective analytical Maxwell solution with the black curve (right panels). The solutions are for $\alpha_{theo} = -0.5$ (first row panel), $\alpha_{theo} = 0$ (second row panel), $\alpha_{theo} = 0.5$ (third row panel) and $\alpha_{theo} = 2$ (fourth row panel). The dashed area represent the quantiles 0.025 (lower) to 0.975 (upper). Unimodal Maxwellian distribution with $\sigma = 150\ km\ s^{-1}$.

The entire procedure is repeated for the bimodal Maxwellian distribution, Fig. 4.13 shows the behavior of λ as a function of α_{theo}. Same as fast rotators from unimodal Maxwellian distribution, the regularization parameter is higher than the one for the slow rotators. It is possible that this behavior is observed in only in fast rotators.

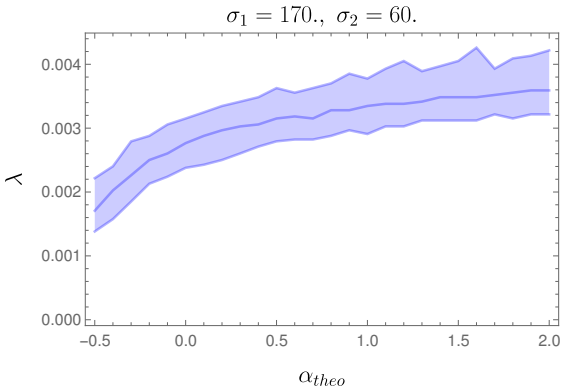

Figure 4.13: Regularization parameter as a function of the theoretical α for 100 MC repetitions of samples of length 200. The dashed area represent the quantiles 0.025 (lower) to 0.975 (upper). Bimodal Maxwellian distribution.

On the other hand, results for PDFs are displayed in Fig. 4.14. These have the special feature for the bimodal Maxwellian distribution to not fit very well for low velocities with respect to $\hat{f}_{true}(v, \alpha_{theo})$. Typical difficulties in fit numerical deconvolutions via Tikhonov regularization is that the borders are not good tracers. This can be reflected in Figs. 4.11, 4.12 and 4.14.

4.2.4 Grid of α

Once we have $\hat{f}_{proj}(v \sin i, \alpha_{theo})$ with their respective deconvolutions $\hat{f}_{true}(v, \alpha_{theo})$ it is necessary to find the best α. The Fredholm integral equation has to be solved for a new grid of α_{ker}, where Tables 4.1 and 4.2 describe the values for a fix α_{theo}. This new grid of solution is shown in Fig. 4.15 and 4.16 ($\sigma = 16\ km\ s^{-1}$ and $150\ km\ s^{-1}$, respectively) for only one MC result. The principal outcome here is that $\bar{f}_{proj}(v \sin i, \alpha_{theo}, \alpha_{ker})$ is indistinguishable with respect to $\hat{f}(v \sin i, \alpha_{theo})$ at any α_{ker} for higher values of α_{theo}. Also, the residues shows how is the variation with respect the original KDE of the data.

The MSE function compute the optimal α to find the spin alignment axes and this is showed in Figs. 4.17 and 4.18 for $\sigma = 16\ km\ s^{-1}$ and $\sigma = 150\ km\ s^{-1}$ respectively. It

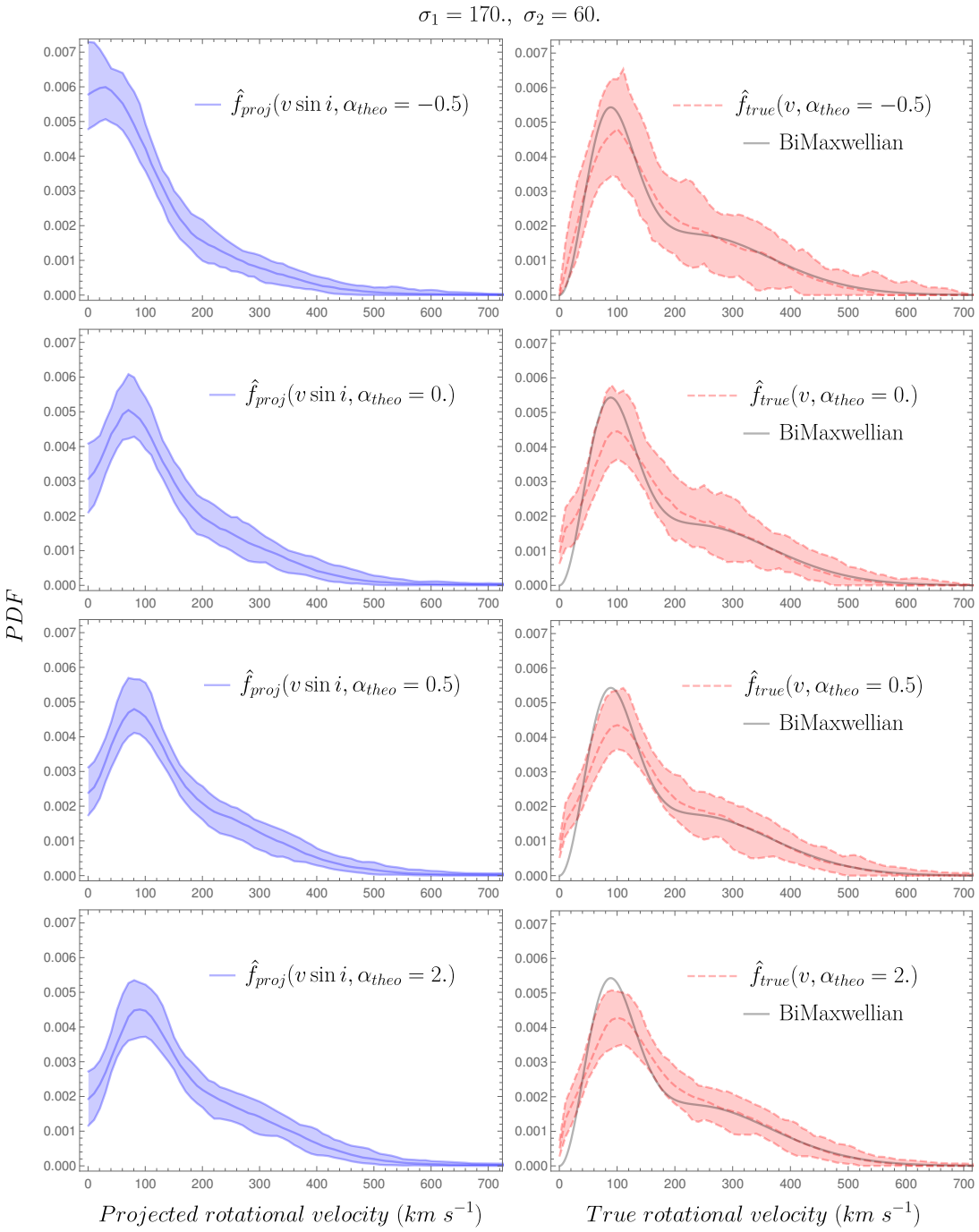

Figure 4.14: Left panels: Kernel density estimator for the projected rotational velocities represented by the blue curves. Right panels: the deconvolution via Tikhonov regularization is represented by the red dashed line with the respective analytical Maxwell solution with the black curve. The solutions are for $\alpha_{theo} = -0.5$ (first row panel), $\alpha_{theo} = 0$ (second row panel), $\alpha_{theo} = 0.5$ (third row panel) and $\alpha_{theo} = 2$ (fourth row panel). The dashed area represent the quantiles 0.025 (lower) to 0.975 (upper). Bimodal Maxwellian distribution.

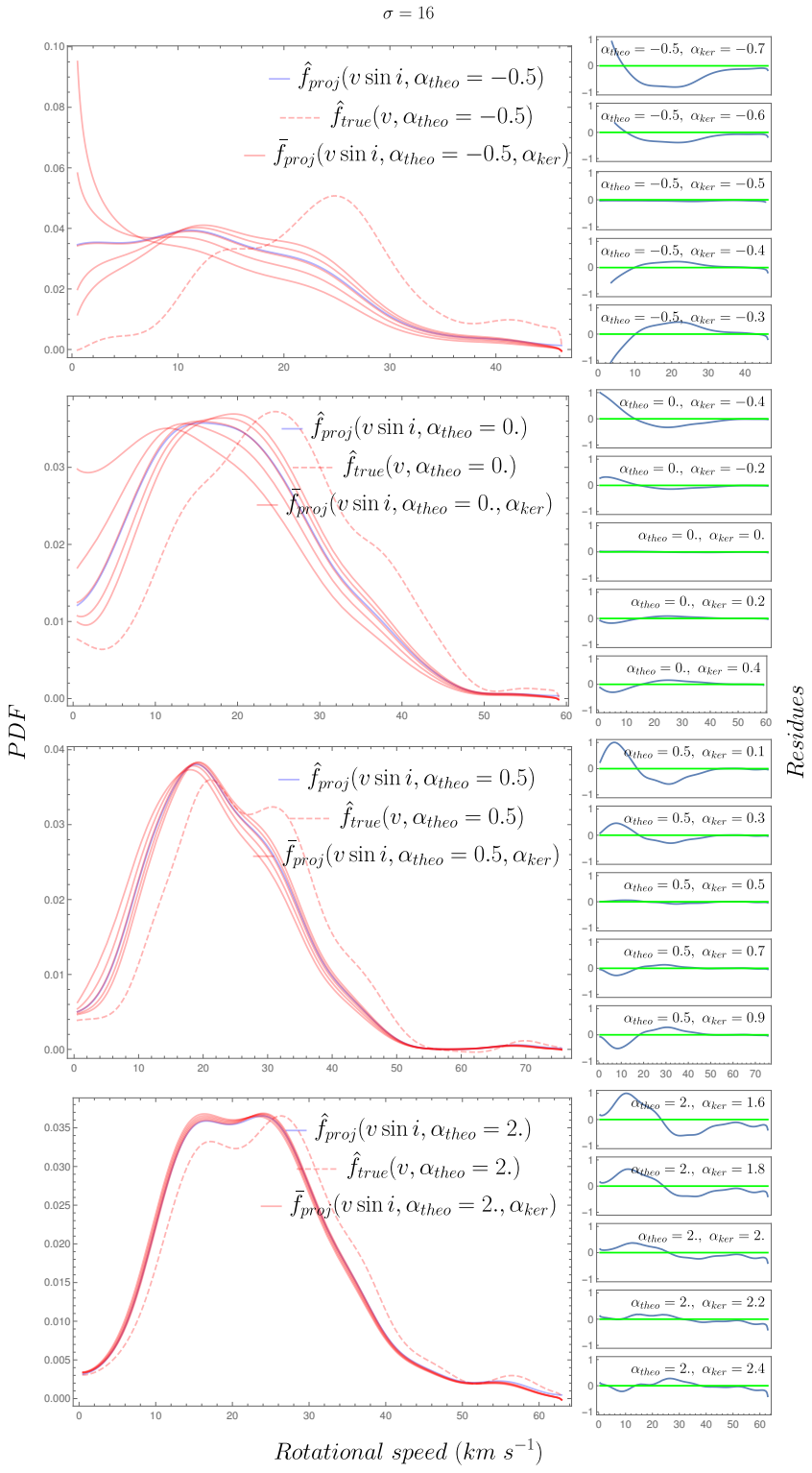

Figure 4.15: $\hat{f}_{true}(v, \alpha_{theo})$ solutions of the Fredholm integral for a grid of α_{ker} represented by the red curves. Blue curve represent the KDE for only one MC repetition, red dashed lines are the deconvolutions via Tikhonov regularization. The residues are showed in the right subfigures. The solutions are for $\alpha_{theo} = -0.5$ (first row), $\alpha_{theo} = 0$ (second row), $\alpha_{theo} = 0.5$ (third row) and $\alpha_{theo} = 2$ (fourth row). Unimodal Maxwellian distribution with $\sigma = 16\ km\ s^{-1}$.

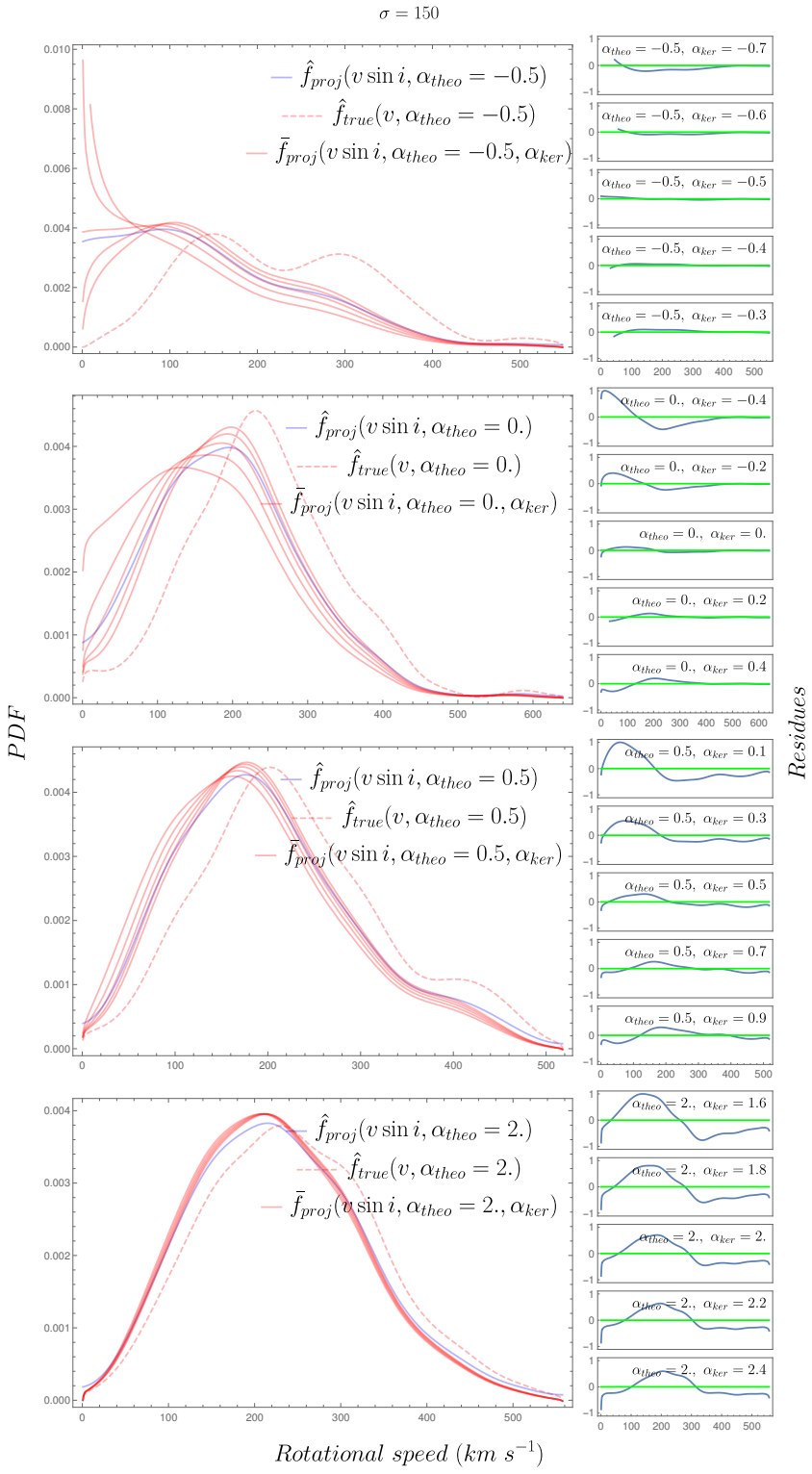

Figure 4.16: $\hat{f}_{true}(v, \alpha_{theo})$ solutions of the Fredholm integral for a grid of α_{ker} represented by the red curves. Blue curve represent the KDE for only one MC repetition, red dashed lines are the deconvolutions via Tikhonov regularization. The residues are showed in the right subfigures. The solutions are for $\alpha_{theo} = -0.5$ (first row), $\alpha_{theo} = 0$ (second row), $\alpha_{theo} = 0.5$ (third row) and $\alpha_{theo} = 2$ (fourth row). Unimodal Maxwellian distribution with $\sigma = 150\ km\ s^{-1}$.

$\alpha_{theo} \leq 0$	$\alpha_{theo} - 0.2$	$\alpha_{theo} - 0.1$	α_{theo}	$\alpha_{theo} + 0.1$	$\alpha_{theo} + 0.2$
$\alpha_{theo} = -0.5$	$\alpha_{ker} = -0.7$	$\alpha_{ker} = -0.6$	$\alpha_{ker} = -0.5$	$\alpha_{ker} = -0.4$	$\alpha_{ker} = -0.3$
$\alpha_{theo} = -0.4$	$\alpha_{ker} = -0.6$	$\alpha_{ker} = -0.5$	$\alpha_{ker} = -0.4$	$\alpha_{ker} = -0.3$	$\alpha_{ker} = -0.2$
$\alpha_{theo} = -0.3$	$\alpha_{ker} = -0.5$	$\alpha_{ker} = -0.4$	$\alpha_{ker} = -0.3$	$\alpha_{ker} = -0.2$	$\alpha_{ker} = -0.1$
$\alpha_{theo} = -0.2$	$\alpha_{ker} = -0.4$	$\alpha_{ker} = -0.3$	$\alpha_{ker} = -0.2$	$\alpha_{ker} = -0.1$	$\alpha_{ker} = 0.0$
$\alpha_{theo} = -0.1$	$\alpha_{ker} = -0.3$	$\alpha_{ker} = -0.2$	$\alpha_{ker} = -0.1$	$\alpha_{ker} = 0.0$	$\alpha_{ker} = 0.1$
$\alpha_{theo} = 0.0$	$\alpha_{ker} = -0.2$	$\alpha_{ker} = -0.1$	$\alpha_{ker} = 0.0$	$\alpha_{ker} = 0.1$	$\alpha_{ker} = 0.2$

Table 4.1: Grid of α_{ker} for $\alpha_{theo} \leq 0$. The first column is the fix value of the theoretical α and the second to the fifth column is the value of α in the kernel.

can be seen that for $\alpha_{theo} = -0.5$, 0 and 0.5 the minimum of the MSE is equal than the expected but for $\alpha_{theo} = 2$ this minimum shifted to lower α_{ker} values.

Other values for α_{ker} are necessary to follow in the bimodal Maxwellian distribution and Tables 4.1 and 4.3 represent this grid of α_{ker} to solve the Fredholm integral equation. Fig. 4.19 and Fig. 4.20 are the solutions of the Fredholm integral equation for a grid of α_{ker} and the mean square error of $\hat{f}_{proj}(v \sin i, \alpha_{theo})$ with $\bar{f}_{proj}(v \sin i, \alpha_{theo}, \alpha_{ker})$, respectively.

4.2.5 Constrain of the method

To analyze the whole grid of 26 α_{theo}, Figs. 4.21 and 4.22 shows the behavior of α_{min} as a function of α_{theo} for the simulations performed ($\sigma = 16\ km\ s^{-1}$ and $\sigma = 150\ km\ s^{-1}$ respectively). For the slow rotators, the method is useful for $\alpha_{theo} \leq 1$ (both 50 and 200 samples), and for fast rotators, the method is useful for $\alpha_{theo} \leq 0.4$ (50 samples) and $\alpha_{theo} \leq 0.2$ (200 samples).

Finally, Fig. 4.23 represent the consistent of the method for a bimodal Maxwellian distribution of statistical weights $C_1 = C_2 = 0.5$ and dispersion velocity parameter $\sigma_1 = 170\ km\ s^{-1}$ and $\sigma_2 = 60\ km\ s^{-1}$. The inference for this is that the method works for $\alpha_{theo} < 1.6$.

4.3 Summary

To generate absorption line profiles, it is necessary to convolve the intrinsic line profile of a star with rotation and then add noise coming from a pseudo-random Gaussian

$\alpha_{theo} > 0$	$\alpha_{theo} - 0.4$	$\alpha_{theo} - 0.2$	α_{theo}	$\alpha_{theo} + 0.2$	$\alpha_{theo} + 0.4$	$\alpha_{theo} + 0.6$	$\alpha_{theo} + 0.8$
$\alpha_{theo} = 0.1$	$\alpha_{ker} = -0.3$	$\alpha_{ker} = -0.1$	$\alpha_{ker} = 0.1$	$\alpha_{ker} = 0.3$	$\alpha_{ker} = 0.5$	$\alpha_{ker} = 0.7$	$\alpha_{ker} = 0.9$
$\alpha_{theo} = 0.2$	$\alpha_{ker} = -0.2$	$\alpha_{ker} = 0.0$	$\alpha_{ker} = 0.2$	$\alpha_{ker} = 0.4$	$\alpha_{ker} = 0.6$	$\alpha_{ker} = 0.8$	$\alpha_{ker} = 1.0$
$\alpha_{theo} = 0.3$	$\alpha_{ker} = -0.1$	$\alpha_{ker} = 0.1$	$\alpha_{ker} = 0.3$	$\alpha_{ker} = 0.5$	$\alpha_{ker} = 0.7$	$\alpha_{ker} = 0.9$	$\alpha_{ker} = 1.1$
$\alpha_{theo} = 0.4$	$\alpha_{ker} = 0.0$	$\alpha_{ker} = 0.2$	$\alpha_{ker} = 0.4$	$\alpha_{ker} = 0.6$	$\alpha_{ker} = 0.8$	$\alpha_{ker} = 1.0$	$\alpha_{ker} = 1.2$
$\alpha_{theo} = 0.5$	$\alpha_{ker} = 0.1$	$\alpha_{ker} = 0.3$	$\alpha_{ker} = 0.5$	$\alpha_{ker} = 0.7$	$\alpha_{ker} = 0.9$	$\alpha_{ker} = 1.1$	$\alpha_{ker} = 1.3$
$\alpha_{theo} = 0.6$	$\alpha_{ker} = 0.2$	$\alpha_{ker} = 0.4$	$\alpha_{ker} = 0.6$	$\alpha_{ker} = 0.8$	$\alpha_{ker} = 0.0$	$\alpha_{ker} = 1.2$	$\alpha_{ker} = 1.4$
$\alpha_{theo} = 0.7$	$\alpha_{ker} = 0.3$	$\alpha_{ker} = 0.5$	$\alpha_{ker} = 0.7$	$\alpha_{ker} = 0.9$	$\alpha_{ker} = 1.1$	$\alpha_{ker} = 1.3$	$\alpha_{ker} = 1.5$
$\alpha_{theo} = 0.8$	$\alpha_{ker} = 0.4$	$\alpha_{ker} = 0.6$	$\alpha_{ker} = 0.8$	$\alpha_{ker} = 0.0$	$\alpha_{ker} = 1.2$	$\alpha_{ker} = 1.4$	$\alpha_{ker} = 1.6$
$\alpha_{theo} = 0.9$	$\alpha_{ker} = 0.5$	$\alpha_{ker} = 0.7$	$\alpha_{ker} = 0.9$	$\alpha_{ker} = 1.1$	$\alpha_{ker} = 1.3$	$\alpha_{ker} = 1.5$	$\alpha_{ker} = 1.7$
$\alpha_{theo} = 1.0$	$\alpha_{ker} = 0.6$	$\alpha_{ker} = 0.8$	$\alpha_{ker} = 1.0$	$\alpha_{ker} = 1.2$	$\alpha_{ker} = 1.4$	$\alpha_{ker} = 1.6$	$\alpha_{ker} = 1.8$
$\alpha_{theo} = 1.1$	$\alpha_{ker} = 0.7$	$\alpha_{ker} = 0.9$	$\alpha_{ker} = 1.1$	$\alpha_{ker} = 1.3$	$\alpha_{ker} = 1.5$	$\alpha_{ker} = 1.7$	$\alpha_{ker} = 1.9$
$\alpha_{theo} = 1.2$	$\alpha_{ker} = 0.8$	$\alpha_{ker} = 1.0$	$\alpha_{ker} = 1.2$	$\alpha_{ker} = 1.4$	$\alpha_{ker} = 1.6$	$\alpha_{ker} = 1.8$	$\alpha_{ker} = 2.0$
$\alpha_{theo} = 1.3$	$\alpha_{ker} = 0.9$	$\alpha_{ker} = 1.1$	$\alpha_{ker} = 1.3$	$\alpha_{ker} = 1.5$	$\alpha_{ker} = 1.7$	$\alpha_{ker} = 1.9$	$\alpha_{ker} = 2.1$
$\alpha_{theo} = 1.4$	$\alpha_{ker} = 1.0$	$\alpha_{ker} = 1.2$	$\alpha_{ker} = 1.4$	$\alpha_{ker} = 1.6$	$\alpha_{ker} = 1.8$	$\alpha_{ker} = 2.0$	$\alpha_{ker} = 2.2$
$\alpha_{theo} = 1.5$	$\alpha_{ker} = 1.1$	$\alpha_{ker} = 1.3$	$\alpha_{ker} = 1.5$	$\alpha_{ker} = 1.7$	$\alpha_{ker} = 1.9$	$\alpha_{ker} = 2.1$	$\alpha_{ker} = 2.3$
$\alpha_{theo} = 1.6$	$\alpha_{ker} = 1.2$	$\alpha_{ker} = 1.4$	$\alpha_{ker} = 1.6$	$\alpha_{ker} = 1.8$	$\alpha_{ker} = 2.0$	$\alpha_{ker} = 2.2$	$\alpha_{ker} = 2.4$
$\alpha_{theo} = 1.7$	$\alpha_{ker} = 1.3$	$\alpha_{ker} = 1.5$	$\alpha_{ker} = 1.7$	$\alpha_{ker} = 1.9$	$\alpha_{ker} = 2.1$	$\alpha_{ker} = 2.3$	$\alpha_{ker} = 2.5$
$\alpha_{theo} = 1.8$	$\alpha_{ker} = 1.4$	$\alpha_{ker} = 1.6$	$\alpha_{ker} = 1.8$	$\alpha_{ker} = 2.0$	$\alpha_{ker} = 2.2$	$\alpha_{ker} = 2.4$	$\alpha_{ker} = 2.6$
$\alpha_{theo} = 1.9$	$\alpha_{ker} = 1.5$	$\alpha_{ker} = 1.7$	$\alpha_{ker} = 1.9$	$\alpha_{ker} = 2.1$	$\alpha_{ker} = 2.3$	$\alpha_{ker} = 2.5$	$\alpha_{ker} = 2.7$
$\alpha_{theo} = 2.0$	$\alpha_{ker} = 1.6$	$\alpha_{ker} = 1.8$	$\alpha_{ker} = 2.0$	$\alpha_{ker} = 2.2$	$\alpha_{ker} = 2.4$	$\alpha_{ker} = 2.6$	$\alpha_{ker} = 2.8$

Table 4.2: Grid of α_{ker} for $\alpha_{theo} > 0$ in the unimodal Maxwellian MC simulations. The first column is the fix value of the theoretical α and the second to the seventh column is the value of α in the kernel.

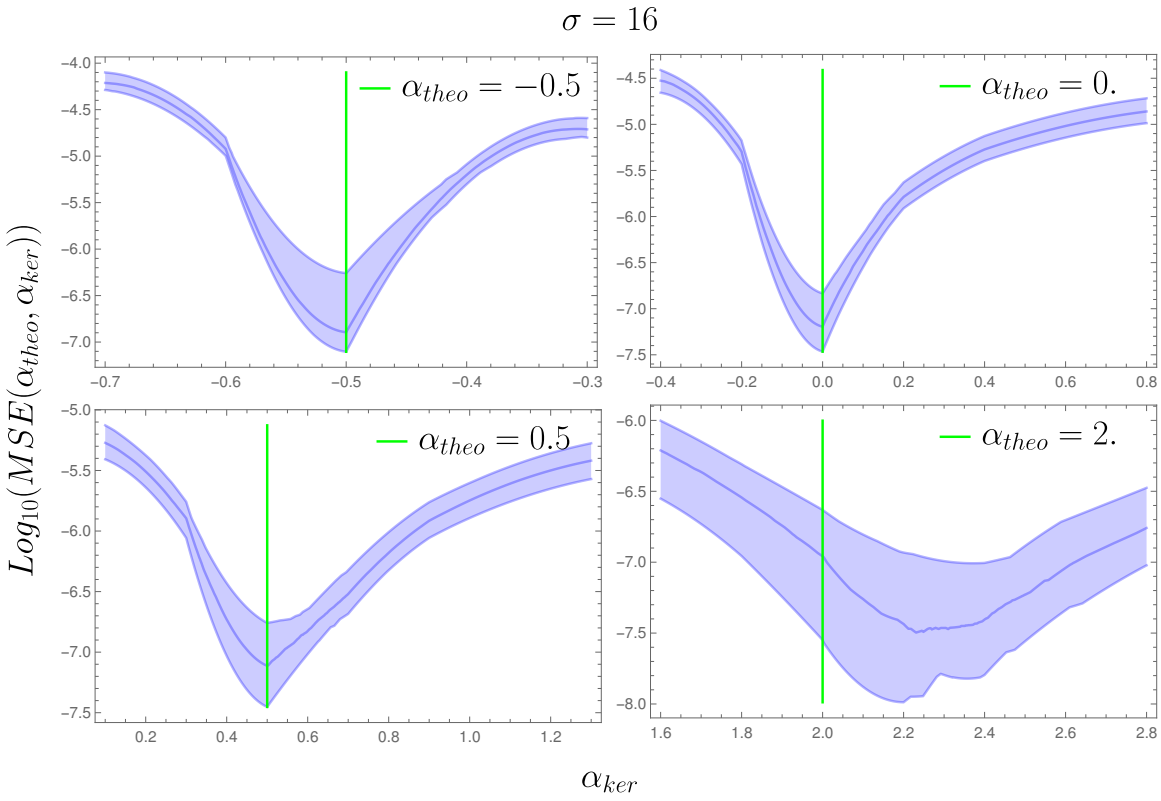

Figure 4.17: $\hat{f}_{true}(v, \alpha_{theo})$ unimodal Maxwellian distribution with $\sigma = 16\, km\, s^{-1}$. Mean square error as a function of the solution given by the Fredholm integral equation for a grid of α_{ker} with respect of the original kernel density estimator from the data. The dashed are represent the quantiles 0.025 (lower) to 0.975 (upper) for 100 MC repetitions and the green vertical line is the theoretical α expected as the correct result. The solutions are for $\alpha_{theo} = -0.5$ (upper left panel), $\alpha_{theo} = 0$ (upper right panel), $\alpha_{theo} = 0.5$ (bottom right panel) and $\alpha_{theo} = 2$ (bottom right panel).

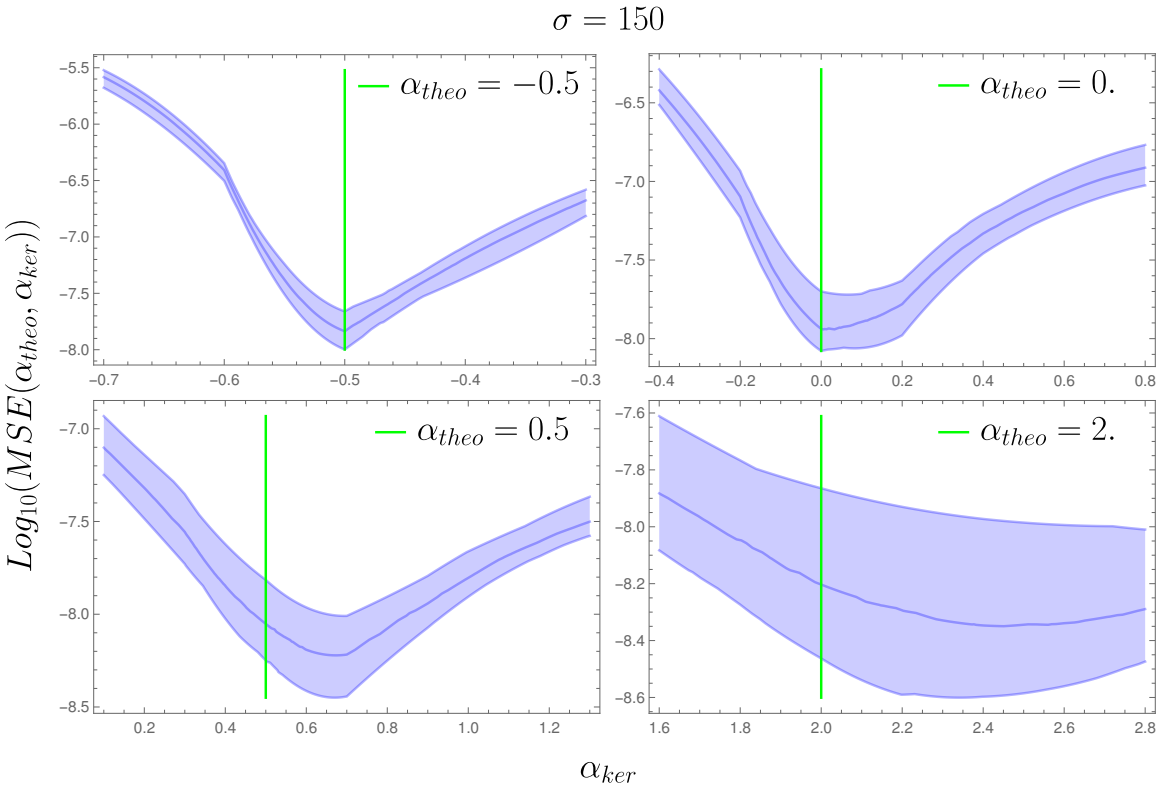

Figure 4.18: $\hat{f}_{true}(v, \alpha_{theo})$ unimodal Maxwellian distribution with $\sigma = 150\ km\ s^{-1}$. Mean square error as a function of the solution given by the Fredholm integral equation for a grid of α_{ker} with respect of the original kernel density estimator from data. The dashed area represent the quantiles 0.025 (lower) to 0.975 (upper) for 100 MC repetitions and the green vertical line is the theoretical α expected as correct result. The solutions are for $\alpha_{theo} = -0.5$ (upper left panel), $\alpha_{theo} = 0$ (upper right panel), $\alpha_{theo} = 0.5$ (bottom right panel) and $\alpha_{theo} = 2$ (bottom right panel).

$\alpha_{theo} > 0$	$\alpha_{theo} - 0.8$	$\alpha_{theo} - 0.6$	$\alpha_{theo} - 0.4$	$\alpha_{theo} - 0.2$	α_{theo}	$\alpha_{theo} + 0.2$	$\alpha_{theo} + 0.4$
$\alpha_{theo} = 0.1$	$\alpha_{ker} = -0.7$	$\alpha_{ker} = -0.5$	$\alpha_{ker} = -0.3$	$\alpha_{ker} = -0.1$	$\alpha_{ker} = 0.1$	$\alpha_{ker} = 0.3$	$\alpha_{ker} = 0.5$
$\alpha_{theo} = 0.2$	$\alpha_{ker} = -0.6$	$\alpha_{ker} = -0.4$	$\alpha_{ker} = -0.2$	$\alpha_{ker} = 0.0$	$\alpha_{ker} = 0.2$	$\alpha_{ker} = 0.4$	$\alpha_{ker} = 0.6$
$\alpha_{theo} = 0.3$	$\alpha_{ker} = -0.5$	$\alpha_{ker} = -0.3$	$\alpha_{ker} = -0.1$	$\alpha_{ker} = 0.1$	$\alpha_{ker} = 0.3$	$\alpha_{ker} = 0.5$	$\alpha_{ker} = 0.7$
$\alpha_{theo} = 0.4$	$\alpha_{ker} = -0.4$	$\alpha_{ker} = -0.2$	$\alpha_{ker} = 0.0$	$\alpha_{ker} = 0.2$	$\alpha_{ker} = 0.4$	$\alpha_{ker} = 0.6$	$\alpha_{ker} = 0.8$
$\alpha_{theo} = 0.5$	$\alpha_{ker} = -0.3$	$\alpha_{ker} = -0.1$	$\alpha_{ker} = 0.1$	$\alpha_{ker} = 0.3$	$\alpha_{ker} = 0.5$	$\alpha_{ker} = 0.7$	$\alpha_{ker} = 0.9$
$\alpha_{theo} = 0.6$	$\alpha_{ker} = -0.2$	$\alpha_{ker} = 0.0$	$\alpha_{ker} = 0.2$	$\alpha_{ker} = 0.4$	$\alpha_{ker} = 0.6$	$\alpha_{ker} = 0.8$	$\alpha_{ker} = 1.0$
$\alpha_{theo} = 0.7$	$\alpha_{ker} = -0.1$	$\alpha_{ker} = 0.1$	$\alpha_{ker} = 0.3$	$\alpha_{ker} = 0.5$	$\alpha_{ker} = 0.7$	$\alpha_{ker} = 0.9$	$\alpha_{ker} = 1.1$
$\alpha_{theo} = 0.8$	$\alpha_{ker} = 0.0$	$\alpha_{ker} = 0.2$	$\alpha_{ker} = 0.4$	$\alpha_{ker} = 0.6$	$\alpha_{ker} = 0.8$	$\alpha_{ker} = 1.0$	$\alpha_{ker} = 1.2$
$\alpha_{theo} = 0.9$	$\alpha_{ker} = 0.1$	$\alpha_{ker} = 0.3$	$\alpha_{ker} = 0.5$	$\alpha_{ker} = 0.7$	$\alpha_{ker} = 0.9$	$\alpha_{ker} = 1.1$	$\alpha_{ker} = 1.3$
$\alpha_{theo} = 1.0$	$\alpha_{ker} = 0.2$	$\alpha_{ker} = 0.4$	$\alpha_{ker} = 0.6$	$\alpha_{ker} = 0.8$	$\alpha_{ker} = 1.0$	$\alpha_{ker} = 1.2$	$\alpha_{ker} = 1.4$
$\alpha_{theo} = 1.1$	$\alpha_{ker} = 0.3$	$\alpha_{ker} = 0.5$	$\alpha_{ker} = 0.7$	$\alpha_{ker} = 0.9$	$\alpha_{ker} = 1.1$	$\alpha_{ker} = 1.3$	$\alpha_{ker} = 1.5$
$\alpha_{theo} = 1.2$	$\alpha_{ker} = 0.4$	$\alpha_{ker} = 0.6$	$\alpha_{ker} = 0.8$	$\alpha_{ker} = 1.0$	$\alpha_{ker} = 1.2$	$\alpha_{ker} = 1.4$	$\alpha_{ker} = 1.6$
$\alpha_{theo} = 1.3$	$\alpha_{ker} = 0.5$	$\alpha_{ker} = 0.7$	$\alpha_{ker} = 0.9$	$\alpha_{ker} = 1.1$	$\alpha_{ker} = 1.3$	$\alpha_{ker} = 1.5$	$\alpha_{ker} = 1.7$
$\alpha_{theo} = 1.4$	$\alpha_{ker} = 0.6$	$\alpha_{ker} = 0.8$	$\alpha_{ker} = 1.0$	$\alpha_{ker} = 1.2$	$\alpha_{ker} = 1.4$	$\alpha_{ker} = 1.6$	$\alpha_{ker} = 1.8$
$\alpha_{theo} = 1.5$	$\alpha_{ker} = 0.7$	$\alpha_{ker} = 0.9$	$\alpha_{ker} = 1.1$	$\alpha_{ker} = 1.3$	$\alpha_{ker} = 1.5$	$\alpha_{ker} = 1.7$	$\alpha_{ker} = 1.9$
$\alpha_{theo} = 1.6$	$\alpha_{ker} = 0.8$	$\alpha_{ker} = 1.0$	$\alpha_{ker} = 1.2$	$\alpha_{ker} = 1.4$	$\alpha_{ker} = 1.6$	$\alpha_{ker} = 1.8$	$\alpha_{ker} = 2.0$
$\alpha_{theo} = 1.7$	$\alpha_{ker} = 0.9$	$\alpha_{ker} = 1.1$	$\alpha_{ker} = 1.3$	$\alpha_{ker} = 1.5$	$\alpha_{ker} = 1.7$	$\alpha_{ker} = 1.9$	$\alpha_{ker} = 2.1$
$\alpha_{theo} = 1.8$	$\alpha_{ker} = 1.0$	$\alpha_{ker} = 1.2$	$\alpha_{ker} = 1.4$	$\alpha_{ker} = 1.6$	$\alpha_{ker} = 1.8$	$\alpha_{ker} = 2.0$	$\alpha_{ker} = 2.2$
$\alpha_{theo} = 1.9$	$\alpha_{ker} = 1.1$	$\alpha_{ker} = 1.3$	$\alpha_{ker} = 1.5$	$\alpha_{ker} = 1.7$	$\alpha_{ker} = 1.9$	$\alpha_{ker} = 2.1$	$\alpha_{ker} = 2.3$
$\alpha_{theo} = 2.0$	$\alpha_{ker} = 1.2$	$\alpha_{ker} = 1.4$	$\alpha_{ker} = 1.6$	$\alpha_{ker} = 1.8$	$\alpha_{ker} = 2.0$	$\alpha_{ker} = 2.2$	$\alpha_{ker} = 2.4$

Table 4.3: Grid of α_{ker} for $\alpha_{theo} > 0$ in the bimodal Maxwellian MC simulations. The first column is the fix value of the theoretical α and the second to the seventh column is the value of α in the kernel.

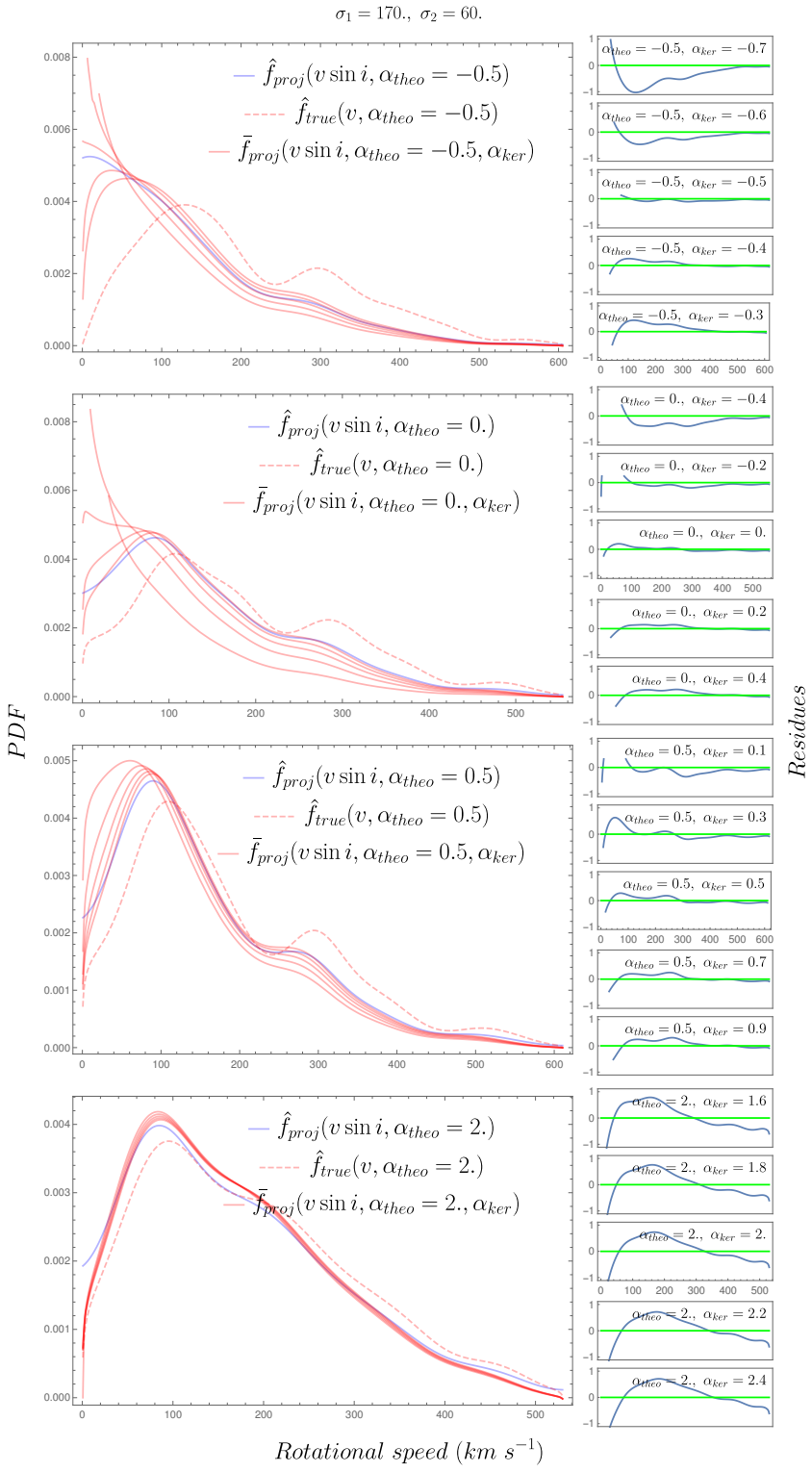

Figure 4.19: Solution of the Fredholm integral for a grid of α_{ker} represented by the red curves. Blue curve represent the KDE for only one MC repetition, red dashed lines are the deconvolutions via Tikhonov regularization. The residues are showed in the right sub-figures. The solutions are for $\alpha_{theo} = -0.5$ (first row), $\alpha_{theo} = 0$ (second row), $\alpha_{theo} = 0.5$ (third row) and $\alpha_{theo} = 2$ (fourth row). Bimodal Maxwellian distribution.

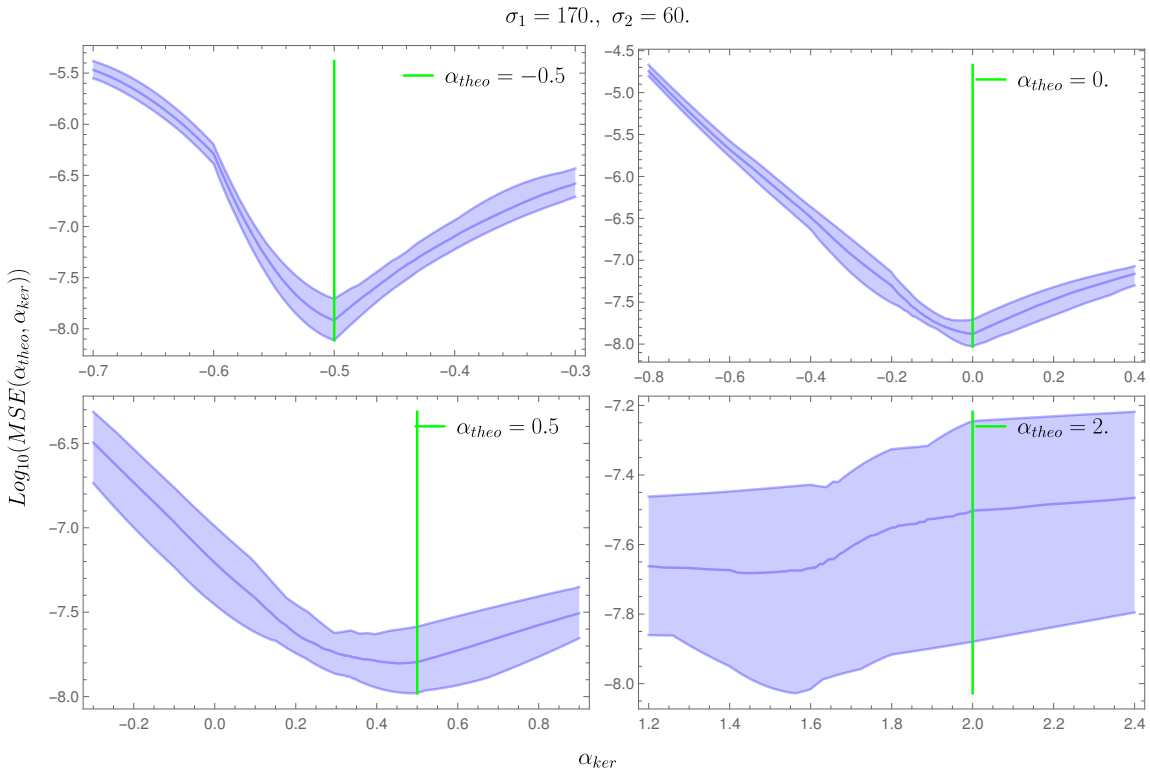

Figure 4.20: Mean square error as a function of the solution given by the Fredholm integral equation for a grid of α_{ker} with respect of the original kernel density estimator from data. The dashed area represent the quantiles 0.025 (lower) to 0.975 (upper) for 100 MC repetitions and the green vertical line is the theoretical α expected as correct result. The solutions are for $\alpha_{theo} = -0.5$ (upper left panel), $\alpha_{theo} = 0$ (upper right panel), $\alpha_{theo} = 0.5$ (bottom right panel) and $\alpha_{theo} = 2$ (bottom right panel). Bimodal Maxwellian distribution.

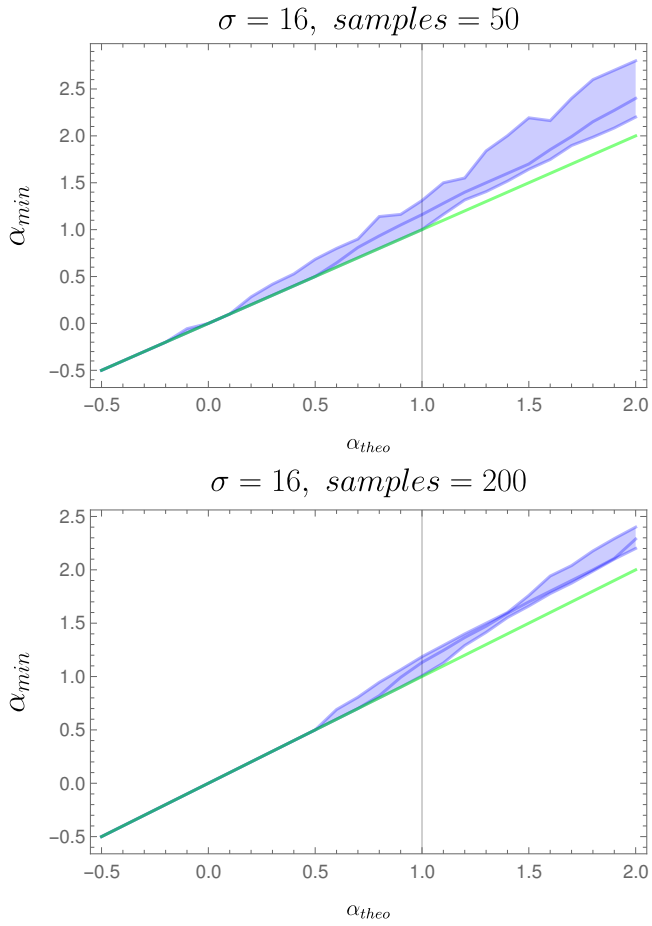

Figure 4.21: Relation between the best α obtained by the MSE with respect to the theoretical one. The dashed area represent the quantiles 0.025 (lower) to 0.975 (upper) for 100 MC repetitions and the green line the 1:1 relation. The upper panel is for 50 samples and the bottom panel for 200 samples. Unimodal Maxwellian distribution with $\sigma = 16\ km\ s^{-1}$.

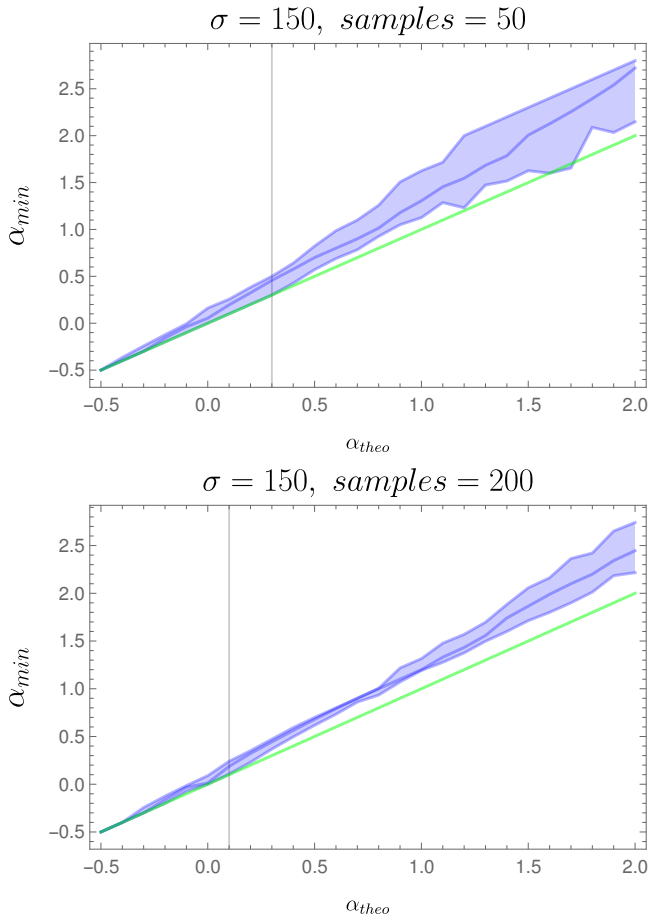

Figure 4.22: Relation between the best α obtained by the MSE with respect to the theoretical one. The dashed area represent the quantiles 0.025 (lower) to 0.975 (upper) for 100 MC repetitions and the green line the 1:1 relation. The upper panel is for samples of length 50 samples and the bottom panel for 200. Unimodal Maxwellian distribution with $\sigma = 150\ km\ s^{-1}$.

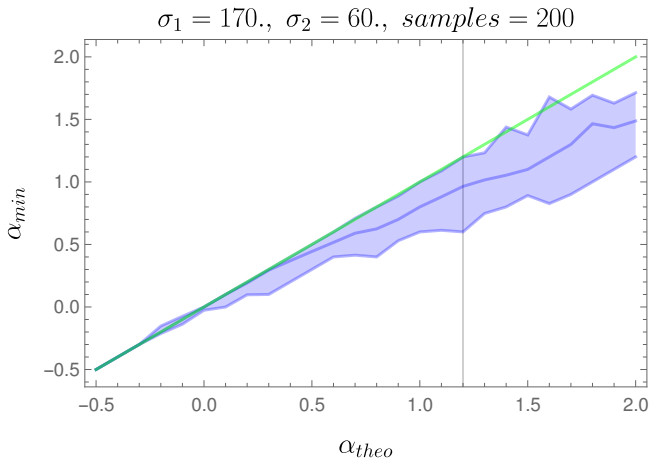

Figure 4.23: Relation between the best α obtained by the MSE with respect to the theoretical one. The dashed area represent the quantiles 0.025 (lower) to 0.975 (upper) for 100 MC repetitions and the green line the 1:1 relation. Bimodal Maxwellian distribution.

distribution. The FT to the grid of lines at different velocities and noise is computed. 10000 MC simulations establish a new criteria for "good" lines (Fig. 4.9).

For the case of how is distributed the stellar axes, unimodal (with two different dispersion values) and bimodal Maxwellian distributions are presented for the true rotational velocities and eq. 4.3 represent the non-isotropic distribution of axes for angles i. Using this, it is possible to construct MC simulations of $v \sin i(\alpha)$ and hereafter study the consistent of our method. In global conclusions, for the three different Maxwellian distributions (two unimodal and one bimodal), our method is reliable until $\alpha \leq 1$ in a 95% of confidence.

CHAPTER 5

Results

In this chapter we present our results obtained from observed data samples. The first section 5.1, "$v \sin i$ obtained from BeSOS", is about use our automated procedure to BeSOS database. The second part is devoted to the non-isotropic rotational velocity distribution from field stars and open clusters, in sections 5.2 and 5.3 respectively.

5.1 $v \sin i$ obtained from BeSOS spectral database

Having developed an automated procedure to obtain the projected rotational velocity via FT, now it is possible to apply it to spectral lines from BeSOS database. Nine HeI absorption lines can be used as tracers of rotational velocities in Be stars: $\lambda\lambda 4387.93, 4437.55, 4471.48, 4713.14, 4921.93, 5015.67, 5047.74, 5875.63$ and 6678.15 $(\AA)$ (Mihalas, 1964; O'Mara & Simpson, 1972; Neiner et al., 2002; Vinicius et al., 2006).

Fig. 5.1 shows the spectra of HD205637_2012-11-14_00-46-43 (HD205637 star in Henry Draper catalog, taken at 00:46:43, on 11-14-2012) for the HeI theoretical lines of $\lambda\lambda 4387.94$, 4471.48 and 4713.14 $(\AA)$ with a window of $2.5\sigma_{fit}$.

The continuum in the line 4387.93 $(\AA)$ shows that the error in both sides is not symmetrical with respect to the midwave. In the case of the line 4471.48 $(\AA)$, the right side of the spectral line shows a bad pixel in the spectrum, this might be caused by a cosmic ray. For the last case, 4713.14 $(\AA)$ line, a very high peak is detected.

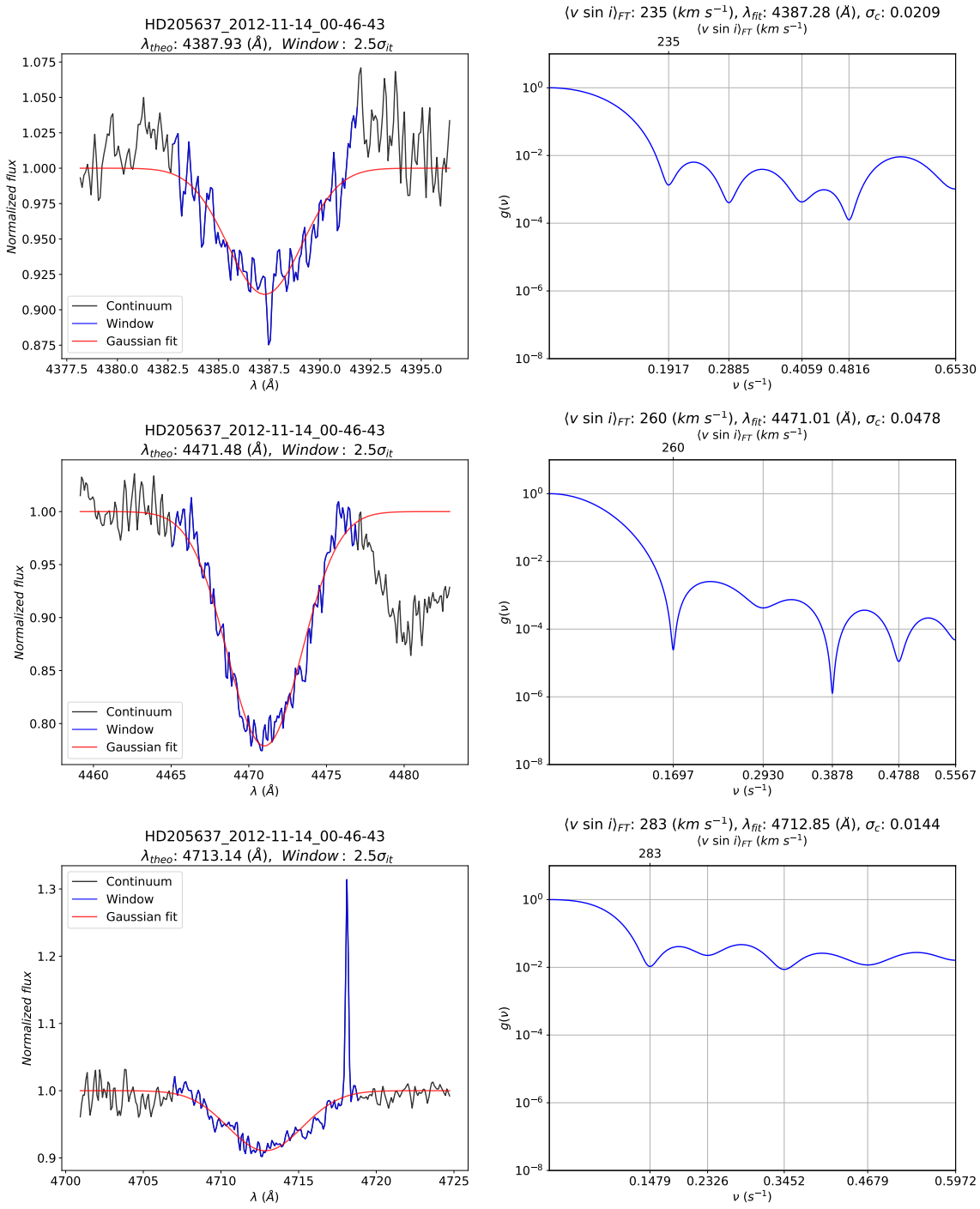

Figure 5.1: Left panels: 3 absorption lines of HD205637. The black lines represents the continuum, where the Gaussian fit given by the red line yields the signal of the absorption line given by the blue lines. Right panels: FT to the absorption lines for an amount of signal given by $2.5\sigma_{fit}$. Top panels: midwave at $\lambda_{theo} = 4387.93$. Middle panels: midwave at $\lambda_{theo} = 4471.48$. Bottom panels: midwave at $\lambda_{theo} = 4712.14$.

It is important to define correctly the window for each absorption line. In the last case if $2\sigma_{fit}$ is taking into account to evaluate the FT, the cosmic rays (peak) are not worked and could give an improve result. In contrast to 4471.48 ($\AA$) line, taking into account the signal closed by a $2\sigma_{fit}$, this can lead a loss of information because the internal wings of the absorption line are not considered. In the case of the $3\sigma_{fit}$ window, sometimes, encloses a lot of useless and unfavorable information since the continuum is evaluated. In conclusion there is not clarity about what is the proper width. That is why we present the results obtained using these 3 typical windows with also the boundary of the 6th criteria. However, in the Fig. 5.2 $\langle v \sin i \rangle_{FT}$ is plotted as a function of the nine λ_{theo}. We included the ones with and without the 6th criteria. To do our analysis in a consistent way, only the velocities inside the interquartile range (IQR) are taking into account, i.e., the 50% of the data between the first quartile (25%) and the third one (75%), the rest are defined as "outliers". To those valid rotational velocities, an average is computed, called $\langle v \sin i \rangle_{FT,ave}$ and $\langle v \sin i \rangle_{FT,ave,crit}$ for the one where the 6th criteria is applied.

The condition to obtain $\langle v \sin i \rangle_{FT,ave}$ is that must be more than one line satisfying the 5 criterias of good line, otherwise, there is no possible to select the IQR and obtain the rotational velocity per epoch.

Finally, for the star HD205637, there were only two epochs and where we repeated the same procedure, then we can see how the rotational velocity changes for each epoch, as shown in Fig. 5.3. We can appreciate that the final average velocity $\langle v \sin i \rangle_{FT,final}$ differs from $\langle v \sin i \rangle_{FT,crit,final}$ by 6 ($km\ s^{-1}$).

Here, we showed in details the procedure for only one star, with a bandwidth of $2.5\sigma_{fit}$ and for the whole database of BeSOS we apply our automated procedure. Tables 5.1, 5.2 and 5.3 summarizes our results.

In general terms, our results are in global agreement with the literature obtained by Arcos et al. (2018) and Frémat et al. (2005) using their own methods to get $v \sin i$. To explore the $v \sin i$ obtained with and without the 6th criteria of "good" absorption line, Fig. 5.4 shows this relation for $2\sigma_{fit}$, $2.5\sigma_{fit}$ and $3\sigma_{fit}$.

From these relations we find that $\langle v \sin i \rangle_{FT,final}$ tends to yield lower values than $\langle v \sin i \rangle_{FT,crit,final}$, that is, when the 6th criteria is applied then the speeds obtained are overstimated with respect to that of the five criterias. This pattern is repeated for signal windows of $2\sigma_{fit}$, $2.5\sigma_{fit}$ and $3\sigma_{fit}$.

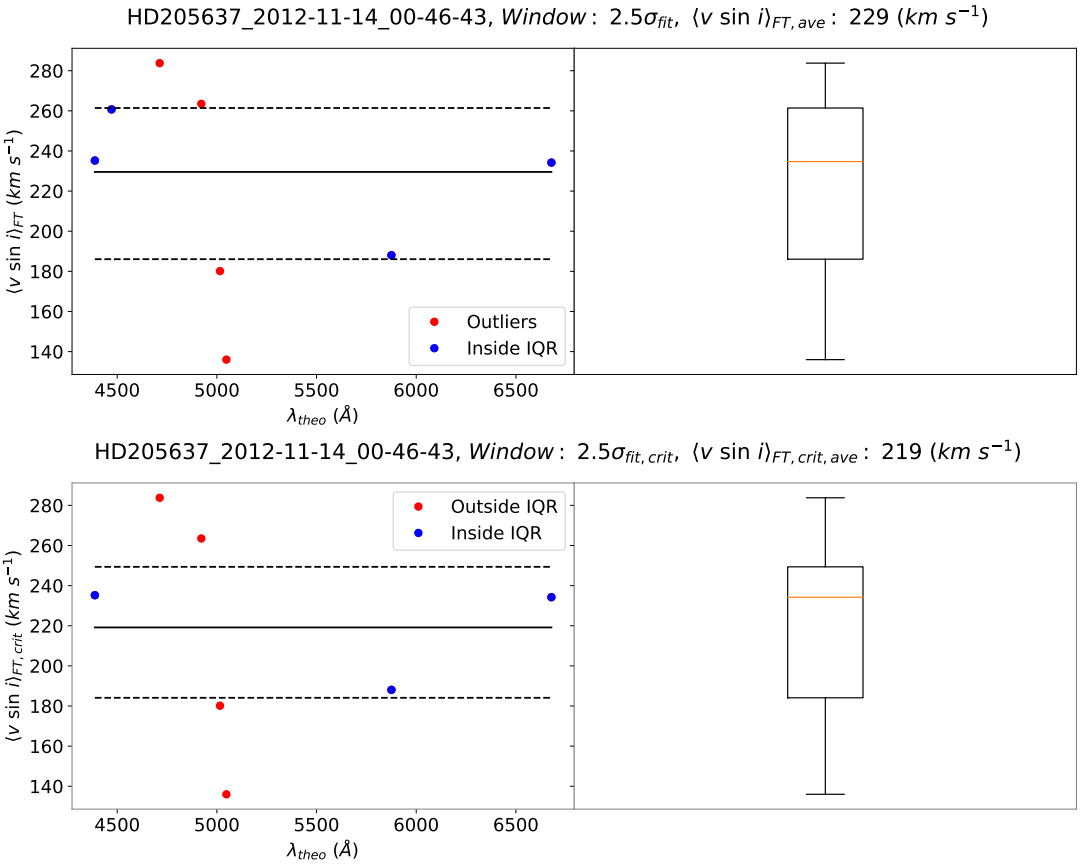

Figure 5.2: Left panels: Average of the velocities inside the IQR (black line), denoted by blue dots, the red dots are considered as outliers of the limits (denoted by the black dashed lines). Right panels: Corresponding boxplot of the same results.

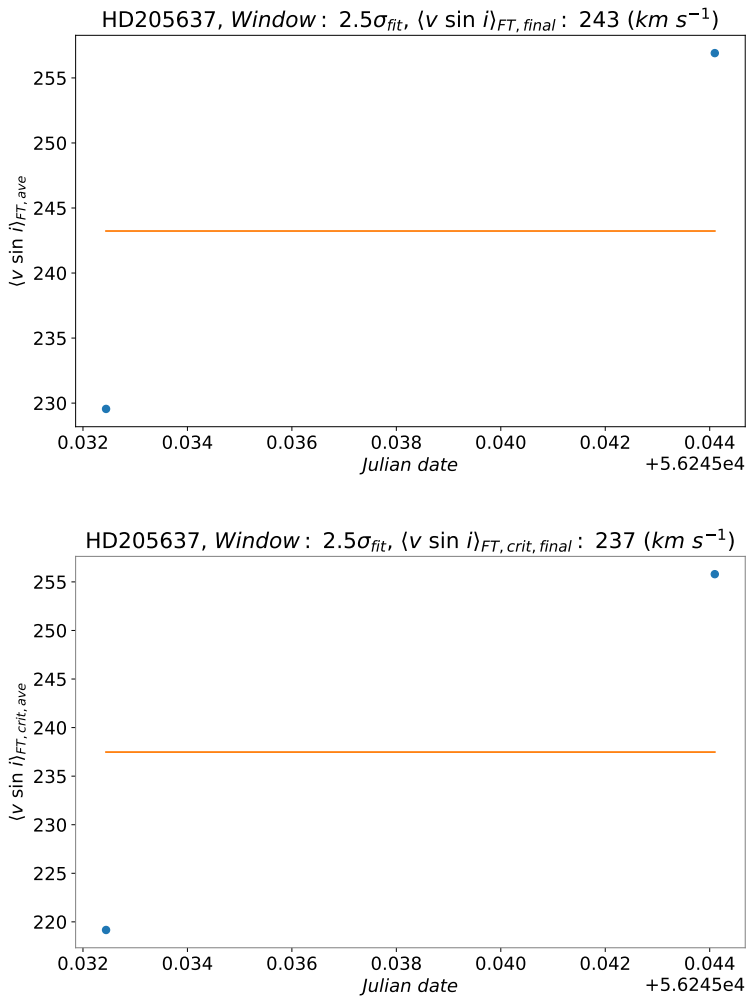

Figure 5.3: Average (orange line) of the projected stellar velocity at two epochs (blue points) for HD205637.

Star	$2\sigma_{fit}$	$2.5\sigma_{fit}$	$3\sigma_{fit}$	$2\sigma_{fit}$ (6th criteria)	$2.5\sigma_{fit}$ (6th criteria)	$3\sigma_{fit}$ (6th criteria)	Arcos et al. (2018)	Frémat et al. (2005)
HD124771	186 (2)	151 (2)	172 (2)	186 (2)	151 (2)	172 (2)	150	205
HD124367	320 (1)	284 (1)	281 (1)	— (—)	— (—)	— (—)	260	318
HD102776	213 (5)	194 (5)	201 (5)	204 (4)	186 (4)	191 (4)	200	270
HD89890	72 (5)	57 (5)	64 (5)	72 (5)	57 (5)	64 (5)	26	67
HD68980	114 (3)	109 (3)	114 (3)	114 (3)	109 (3)	114 (3)	110	152
HD41335	247 (5)	249 (5)	259 (4)	205 (5)	200 (4)	234 (4)	330	376
HD37041	138 (5)	133 (5)	141 (5)	137 (5)	133 (5)	136 (4)	140	133
HD214748	183 (9)	185 (9)	189 (7)	183 (9)	181 (8)	189 (7)	—	205
HD42167	191 (2)	205 (3)	217 (3)	175 (2)	182 (3)	171 (3)	—	249
HD35439	242 (8)	241 (7)	262 (7)	238 (7)	235 (7)	246 (3)	266	266
HD92938	122 (7)	115 (7)	121 (7)	122 (7)	115 (7)	121 (7)	110	139
HD148184	118 (5)	108 (5)	114 (5)	119 (5)	108 (5)	113 (5)	150	151
HD131492	158 (6)	149 (6)	150 (6)	140 (6)	132 (6)	130 (4)	100	192
HD212571	219 (4)	216 (4)	225 (4)	200 (5)	216 (4)	225 (4)	215	233
HD167128	59 (3)	56 (3)	59 (3)	59 (3)	56 (3)	59 (3)	50	55
HD205637	241 (2)	243 (2)	253 (2)	233 (2)	237 (2)	253 (2)	230	238
HD209014	188 (1)	157 (1)	191 (1)	188 (1)	157 (1)	191 (1)	—	357
HD103192	205 (4)	167 (4)	175 (3)	166 (2)	138 (3)	138 (3)	—	42
HD219688	284 (4)	271 (2)	259 (2)	— (—)	— (—)	— (—)	—	316
HD48917	186 (10)	173 (10)	189 (10)	176 (9)	161 (8)	175 (7)	200	212
HD157042	301 (5)	301 (5)	310 (5)	307 (4)	311 (3)	301 (2)	280	348

Table 5.1: Summary of projected stellar rotational velocities for different methods. Name of the star (first column). $v \sin i$ (in $km\ s^{-1}$) obtained by our method by the size of the bandwidth (with and without the 6th criteria) and in parentheses their respective number of epochs (2nd to 7th column), Arcos et al. (2018) (8th column) and Frémat et al. (2005) (9th column).

Star	$2\sigma_{fit}$	$2.5\sigma_{fit}$	$3\sigma_{fit}$	$2\sigma_{fit}$ (6th criteria)	$2.5\sigma_{fit}$ (6th criteria)	$3\sigma_{fit}$ (6th criteria)	Arcos et al. (2018)	Frémat et al. (2005)
HD57219	83 (4)	76 (4)	78 (4)	83 (4)	76 (4)	78 (4)	50	84
HD37795	172 (8)	163 (9)	170 (9)	168 (9)	156 (9)	171 (8)	—	192
HD217891	81 (10)	80 (10)	83 (10)	80 (10)	80 (10)	82 (10)	90	100
HD105382	88 (5)	76 (5)	83 (5)	88 (5)	76 (5)	81 (5)	67	72
HD181615	137 (4)	117 (4)	130 (4)	— (—)	— (—)	— (—)	—	37
HD209409	233 (2)	242 (2)	277 (3)	— (—)	— (—)	— (—)	350	282
HD58343	56 (2)	45 (2)	45 (2)	56 (2)	45 (2)	45 (2)	10	49
HD45910	134 (6)	117 (6)	120 (6)	— (—)	— (—)	— (—)	100	254
HD93563	234 (4)	209 (3)	156 (1)	167 (1)	141 (3)	123 (3)	280	275
HD212076	105 (6)	96 (6)	102 (6)	105 (5)	94 (5)	100 (5)	100	103
HD75311	253 (2)	236 (2)	238 (2)	253 (2)	236 (2)	238 (2)	250	283
HD78764	126 (3)	105 (3)	115 (3)	126 (3)	105 (3)	115 (3)	140	120
HD135734	214 (3)	232 (3)	230 (3)	215 (4)	232 (4)	248 (4)	—	282
HD142983	305 (4)	274 (3)	315 (3)	— (—)	— (—)	— (—)	370	407
HD120324	128 (3)	112 (3)	121 (3)	128 (3)	112 (3)	121 (3)	110	162
HD68423	89 (1)	83 (1)	84 (1)	89 (1)	83 (1)	84 (1)	—	26
HD35411	289 (3)	228 (2)	266 (2)	225 (2)	220 (2)	107 (1)	53	174
HD107348	227 (2)	216 (3)	254 (3)	218 (2)	211 (2)	242 (1)	—	237
HD91465	273 (6)	274 (6)	280 (6)	244 (2)	256 (5)	275 (4)	280	285
HD138769	79 (5)	73 (5)	72 (5)	79 (5)	73 (5)	72 (5)	30	78

Table 5.2: Continuation of Table 5.1.

Star	$2\sigma_{fit}$	$2.5\sigma_{fit}$	$3\sigma_{fit}$	$2\sigma_{fit}$ (6th criteria)	$2.5\sigma_{fit}$ (6th criteria)	$3\sigma_{fit}$ (6th criteria)	Arcos et al. (2018)	Frémat et al. (2005)
HD10144	243 (2)	228 (2)	233 (2)	237 (2)	222 (2)	229 (2)	—	—
HD60606	253 (6)	254 (6)	261 (6)	253 (6)	254 (6)	262 (6)	250	285
HD56139	82 (4)	76 (4)	79 (4)	82 (4)	76 (4)	79 (4)	100	89
HD157246	259 (4)	256 (4)	264 (4)	258 (4)	256 (4)	263 (4)	230	230
HD89080	211 (2)	202 (4)	179 (3)	211 (2)	200 (2)	168 (1)	—	254
HD56014	144 (2)	155 (2)	116 (2)	144 (2)	155 (2)	116 (2)	200	290
HD98058	233 (2)	224 (1)	223 (1)	— (—)	— (—)	— (—)	—	254
HD105435	247 (3)	246 (3)	245 (3)	243 (3)	232 (3)	237 (2)	250	163
HD50013	227 (6)	211 (6)	232 (6)	227 (6)	211 (6)	232 (6)	290	244
HD112078	309 (1)	301 (1)	337 (1)	— (—)	— (—)	— (—)	290	327
HD71510	159 (6)	149 (6)	148 (6)	159 (6)	149 (6)	147 (6)	150	154
HD58715	264 (2)	225 (1)	223 (1)	— (—)	— (—)	— (—)	—	231
HD127972	241 (4)	215 (4)	214 (4)	233 (4)	208 (4)	206 (4)	240	326
HD124195	125 (2)	121 (2)	130 (2)	113 (1)	113 (1)	123 (2)	150	—
HD35165	302 (2)	288 (2)	256 (5)	— (—)	— (—)	— (—)	240	350
HD33328	283 (5)	268 (5)	285 (5)	279 (5)	264 (5)	281 (4)	287	333
HD143275	193 (1)	161 (1)	175 (2)	193 (1)	161 (1)	175 (2)	257	150
HD45725	346 (2)	334 (2)	336 (2)	— (—)	— (—)	— (—)	280	345
HD57150	206 (2)	208 (2)	224 (2)	208 (2)	209 (2)	225 (2)	180	290
HD52918	305 (2)	302 (2)	311 (2)	— (—)	— (—)	— (—)	242	265

Table 5.3: Continuation of Table 5.1 and 5.2.

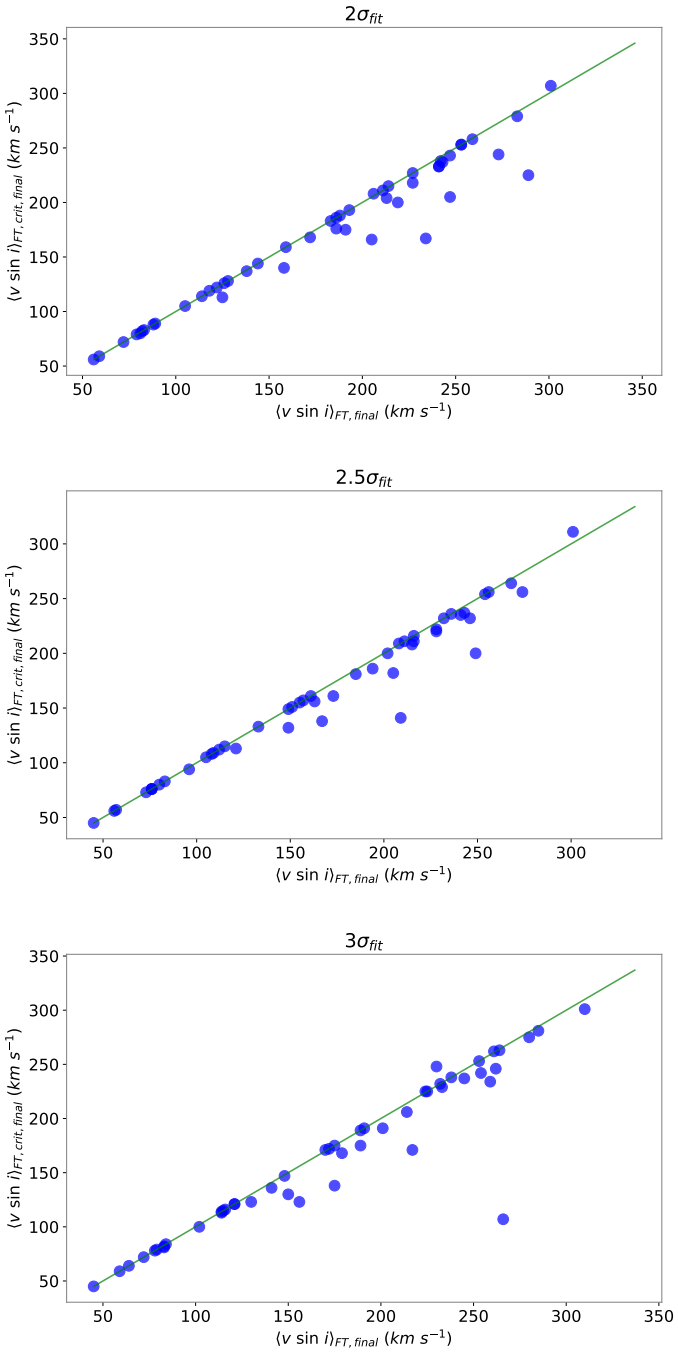

Figure 5.4: Projected rotational velocities obtained via FT transform with (y-axis) and without 6th criteria (x-axis) of "good" lines. The signal windows are for $2\sigma_{fit}$ (upper panel), $2.5\sigma_{fit}$ (middle panel) and $3\sigma_{fit}$ (upper panel).

5.2 Non-isotropic distribution of axes in field stars

Based on the results of MC simulations and their constrains, now we apply our non-isotropic methodology to a field star database of projected rotational velocities.

5.2.1 Stellar properties

The first field stars database that we used is from Nordström et al. (2004) and Holmberg et al. (2007), which have $v \sin i$ for 16682 nearby F and G dwarf stars. We use 11818 samples, derived from Carvalho et al. (2009) and analyzed by Curé et al. (2014) where they select rotational values with $v \sin i < 30$ $(km\ s^{-1})$. Fig. 5.5 show the location of these stars around the Solar neighborhood with their respective values of projected rotational velocities.

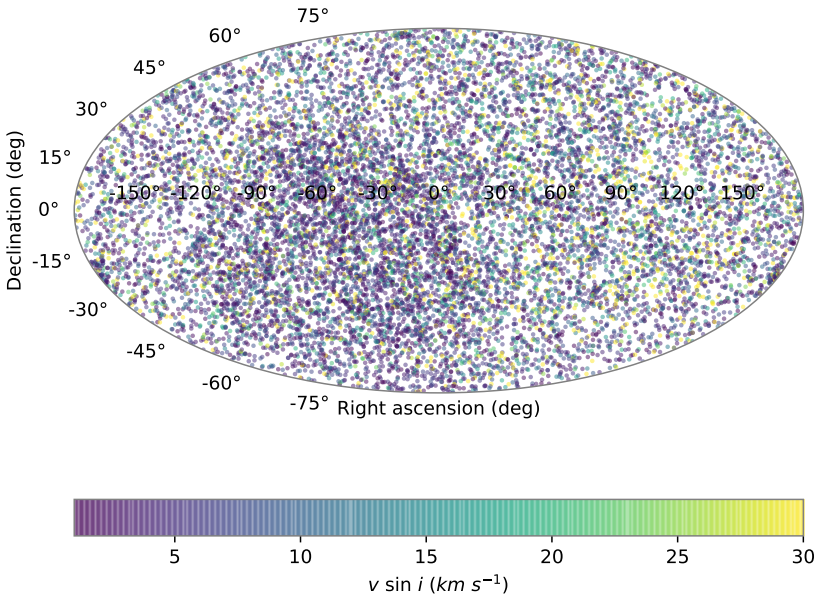

Figure 5.5: Spatial distribution of field stars as a function of the projected rotational velocities.

5.2.2 Deconvolution of a real sample

The histogram of 11818 $v \sin i$ values and, in order to quantify this, the respective KDE (non-parametric fit) to data is showed in Fig. 5.6. From that histogram (and the respective KDE), it can be appreciated that the highest concentration of $v \sin i$ values is in $\sim$ 3 $(km\ s^{-1})$, being slow rotator as expected for F- and G-type spectral type stars. As α_{theo} is an unknown value then $\hat{f}_{proj}(v \sin i, \alpha_{theo})$ is converted to $\hat{f}_{proj}(v \sin i)$ because out intention is to find the optimal α value that yields the non-isotropy for the distribution of axes. This is repeated for any database of stars.

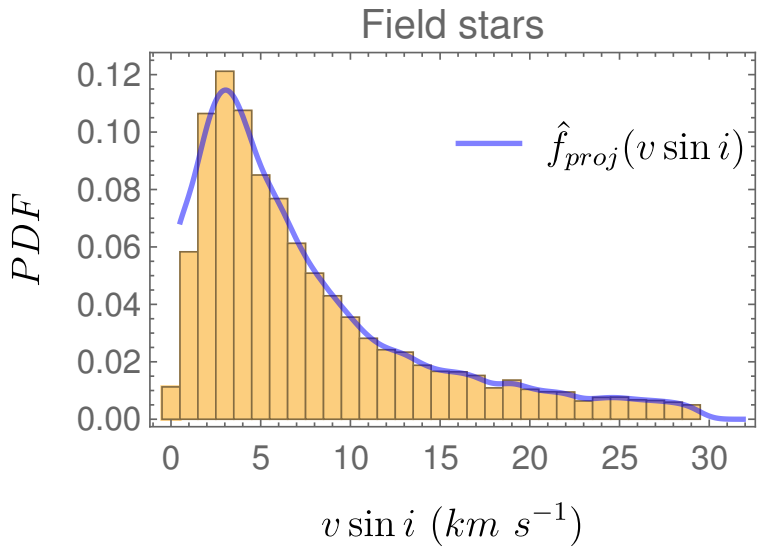

Figure 5.6: Kernel density estimator (blue curve) to $v \sin i$ data (histogram) in field stars.

The Tikhonov regularization parameter as a function of the theoretical α for these field stars is shown in Fig. 5.7, where α_{theo} is given by a grid of solutions from -0.5 to 2 in steps of 0.1, being a total of 26 different values. As these stars are slow rotators, it can be identify that the regularization parameter λ follows an equivalent scale with respect to MC simulations of slow rotators (see upper panel of Fig. 4.10).

5.2.3 Grid of optimal α for a real sample

To compute the non-isotropic distribution of axes it is necessary to get α_{min}. To do that, KDE of $v \sin i$, deconvolution via Tikhonov regularization and solutions given by the Fredholm integral are calculated for α_{theo} from -0.5 to 2 in steps of 0.1. For simplicity, only a grid for $\alpha_{theo} = -0.5, 0, 0.5$ and 2 is showed 5.8.

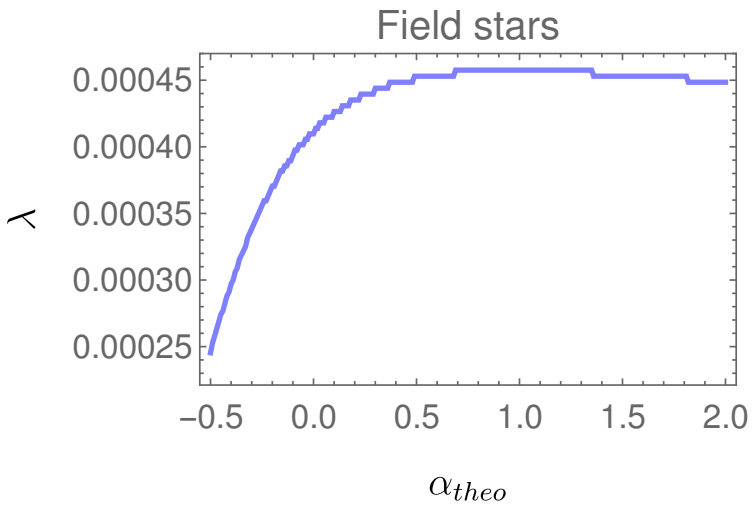

Figure 5.7: Regularization parameter λ as a function of α in field stars.

Here we can appreciate that the deconvolution for $\alpha_{theo} = -0.5$, the respective distribution for $v \leq 2$ $(km\ s^{-1})$ gives negative PDF values, which is not considered as a correct model. For the case of the original PDF $\hat{f}_{proj}(v \sin i, \alpha_{theo} = -0.5)$, this is not similar to $\bar{f}_{proj}(v \sin i, \alpha_{theo} = -0.5)$ in contrast to $\alpha_{theo} = 0, 0.5$ and 2. To visualize better this comparison, Fig. 5.9 describe the MSE for the whole grid of α_{theo}. The minimum is reached at -0.03. This value means that these 11818 field stars have a distribution of axes very isotropically ($\alpha \sim 0$), that is, rotating uniformly over the sphere.

The Kaniadakis distribution (Kaniadakis, 2002, 2005), $Kan(k, \sigma_k, x)$, is given by

$$Kan(k, \sigma_k, x) = \frac{8k^4}{\sigma_k^3}\sqrt{\frac{2}{\pi}}\frac{\Gamma(\frac{7}{4}+\frac{1}{2k})}{\Gamma(\frac{1}{2k}-\frac{3}{4})}x^2\left(\sqrt{\frac{k^2x^4}{\sigma_k^4}+1}-\frac{kx^2}{\sigma_k^2}\right)^{1/k} \tag{5.1}$$

where σ_k is the dispersion and k the Kaniadakis parameter. An unimodal Kaniadakis distribution was firstly fitted to the best true rotational velocity PDF $\hat{f}_{true}(v \sin i, \alpha_{theo} = \alpha_{min} = -0.03)$ yielding a least square regression value of 0.192, being the best parameter values $\sigma_k = 2.7$ and $k = -0.68$. Curé et al. (2014) estimated for this sample the one step solution of the CDF for the equatorial rotational speeds with the assumption of isotropical distribution of axes in the kernel of the Fredholm integral. The models were the unimodal Tsallis, Maxwellian and Kaniadakis distributions yielding least square regression values of 0.0126, 0.3142 and 0.0217. To search for better functions that reproduce the distribution of true rotational velocities in this

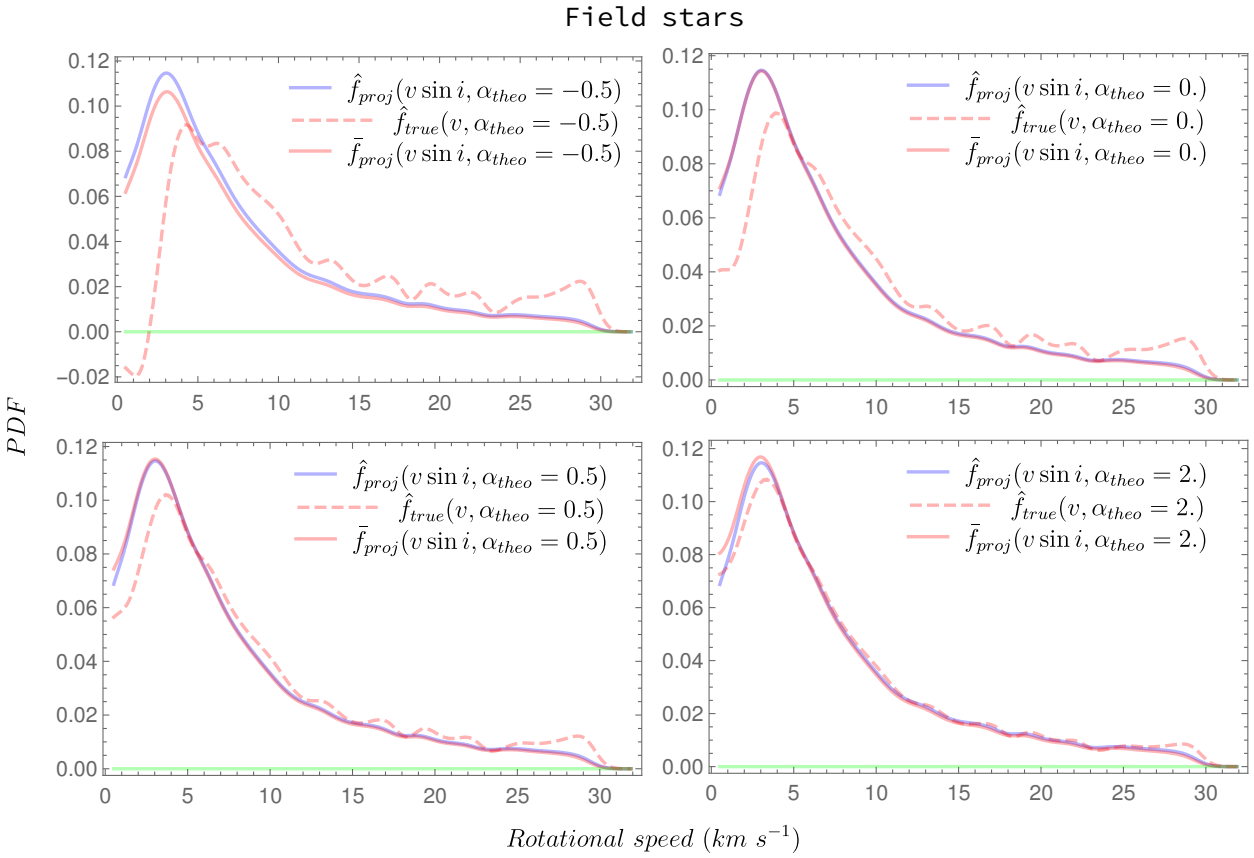

Figure 5.8: Kernel density estimator of the $v \sin i$ data (blue line) with the respective Tikhonov regularization PDF (red dashed line) and the solution by the Fredholm integral equation (red line) for the Geneva sample of field stars. There are four grid solution for $\alpha_{theo} = -0.5$ (upper left panel), $\alpha_{theo} = 0$ (upper right panel), $\alpha_{theo} = 0.5$ (bottom left panel) and $\alpha_{theo} = 2$ (bottom right panel).

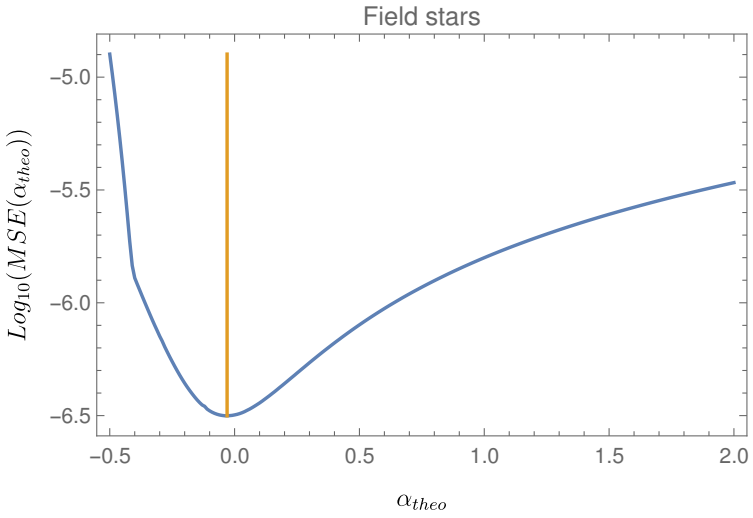

Figure 5.9: Mean square error in field stars (blue line). The orange vertical line represent the place of $\alpha_{min} = -0.03$.

field stars, a bimodal Kaniadakis distribution, $BiKan(c_1, c_2, k_1, k_2, \sigma_{k_1}, \sigma_{k_2}, x)$, is fitted, this distribution reads:

$$BiKan(c_1, c_2, k_1, k_2, \sigma_{k_1}, \sigma_{k_2}, x) = \frac{c_1}{c_1 + c_2}\left(\frac{8k_1^4}{\sigma_{k_1}^3}\sqrt{\frac{2}{\pi}}\frac{\Gamma(\frac{7}{4}+\frac{1}{2k_1})}{\Gamma(\frac{1}{2k_1}-\frac{3}{4})}x^2\left(\sqrt{\frac{k_1^2x^4}{\sigma_{k_1}^4}+1}-\frac{k_1x^2}{\sigma_{k_1}^2}\right)^{1/k_1}\right) + \frac{c_2}{c_1 + c_2}\left(\frac{8k_2^4}{\sigma_{k_2}^3}\sqrt{\frac{2}{\pi}}\frac{\Gamma(\frac{7}{4}+\frac{1}{2k_2})}{\Gamma(\frac{1}{2k_2}-\frac{3}{4})}x^2\left(\sqrt{\frac{k_2^2x^4}{\sigma_{k_2}^4}+1}-\frac{k_2x^2}{\sigma_{k_2}^2}\right)^{1/k_2}\right) \quad (5.2)$$

where c_1 and c_2 are the amplitudes, k_1 and k_2 the Kaniadakis parameters, and σ_{k_1} and σ_{k_2} the dispersions. Fig. 5.10. shows this fit and the true rotational velocity PDF $\hat{f}_{true}(v \sin i, \alpha_{theo} = \alpha_{min} = -0.03)$ for this field stars.

The least square regression gives value of 0.048 (bimodal Kaniadakis distribution), better than 0.192 (unimodal Kaniadakis distribution) and parameters of $c_1 = 0.968$, $c_2 = 0.032$, $k_1 = -0.652$, $k_2 = -0.105$, $\sigma_{k_1} = 2.824$ and $\sigma_{k_2} = 5.712$.

5.2.4 Confidence intervals

Once α_{min} is derived, a bootstrap of 1000 repetitions is computed for the initial 11818 $v \sin i$ values. Since there is necessary to solve the Fredholm integral equation, with a linear grid of α_{ker} from -0.04 to 0.01 in steps of 0.01. The MSE for these confidence

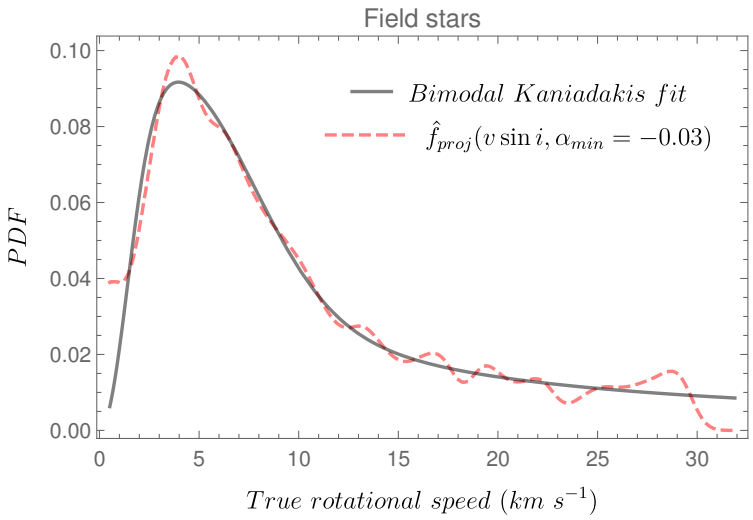

Figure 5.10: Best true rotational velocity PDF (red dashed line) with the best Kaniadakis distribution (black line) in field stars.

interval is displayed in Fig. 5.11.

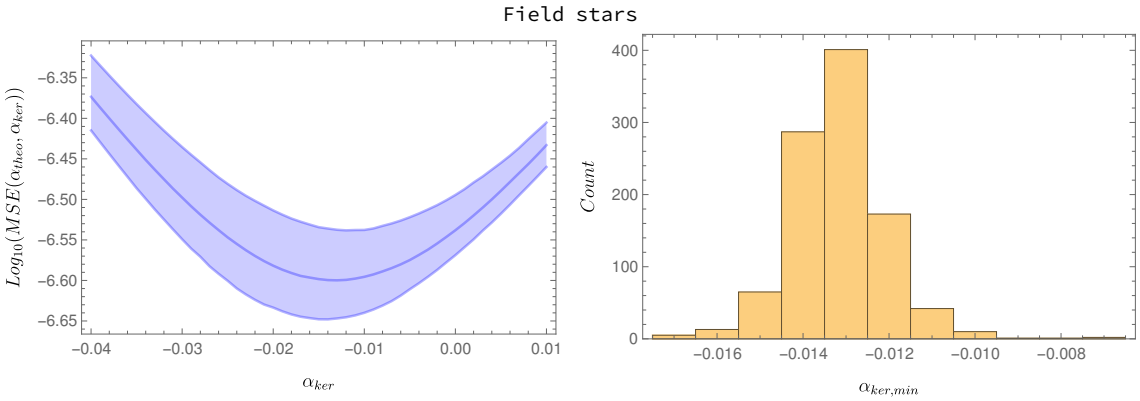

Figure 5.11: Bootstrap calculations give the mean square error in field stars (blue curve) with confidence intervals of 2.5 to 97.5% (left panel) and the respective histogram (right panel) for field stars.

The minimum for bootstrap repetitions is at -0.013, being a higher value from $\alpha_{min} = -0.03$. This shift can be interpreted as neglectable.

5.2.5 CDF correlation

In order to compute the CDF, the typical eq. 2.140 is used replacing $f_X(t)$ for $\hat{f}_{true}(v, \alpha_{theo} = \alpha_{min})$. Our new solution, given by eq. 2.156, needs an analytical solution by $f_{proj}(y)$ but we can use the PDF $\bar{f}_{proj}(v \sin i, \alpha_{theo} = \alpha_{min})$. Those 2 different solutions are showed in Fig. 5.12 with a $q - q$ plot that compare the probability distributions by plotting their quantiles against each other.

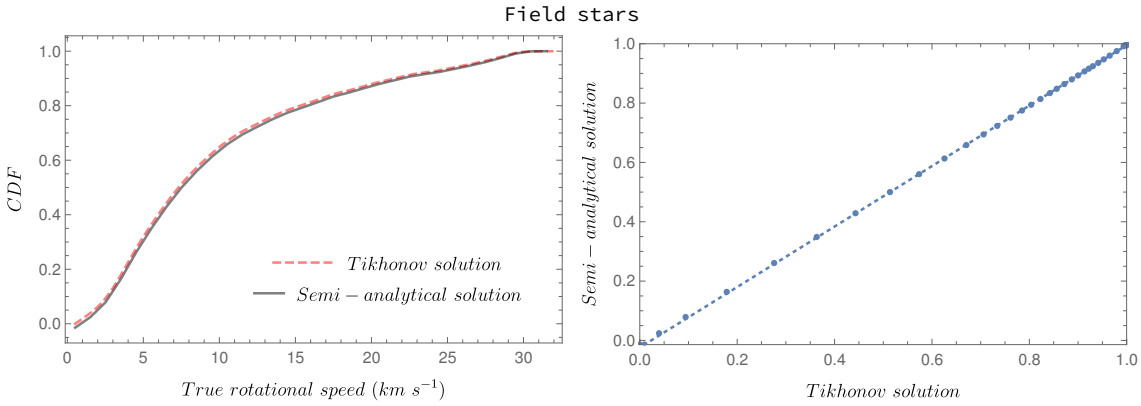

Figure 5.12: Best true rotational velocity CDF by Tikhonov regularization (red dashed line) with the semi-analytical solution (black line) in the left panel. The right panel shows the $q - q$ plot. This is for Geneva field stars.

It can be appreciated that they are very similar and the $q - q$ plot confirms it. Using a non-isotropic distribution of axes in the kernel of the Fredholm integral, KDE and deconvolution via Tikhonov regularization to obtain α_{min} and hence replacing this value into the our CDF one step solution yields the same distribution.

5.3 Non-isotropic distribution of axes in an open cluster

Now, we apply oyr non-isotropic methodology to an open cluster database of projedted rotational velocities.

5.3.1 Stellar properties

We select the open cluster of the 30 Doradus (30 Dor) region of the Large Magellanic Cloud, also known as the Tarantula nebula, which is the nearest starburst region. Stellar population of Tarantula nebula is from stellar formation in progress to older supergiants ($\sim 20 - 25$ Myr), spanning multiple ages (Grebel & Chu, 2000; Brandner et al., 2001; Walborn et al., 2013). We took rotational velocities from Ramírez-Agudelo et al. (2013), a VLT-FLAMES Tarantula Survey project, in which the observational overview have been described in Evans et al. (2011). This sample contains 216 stars with $v \sin i$ data from 40 $(km\ s^{-1})$ up to 610 $(km\ s^{-1})$. Fig. 5.13 represents the spatial distribution for these rotational stars.

In the last figure it can be noted that there is a double spatial concentration for the stars.

5.3.2 Deconvolution of a real sample

In the case of the open cluster, for comparison purposes, following Ramírez-Agudelo et al. (2013) and also Christen et al. (2016), the two largest values of the sample are discarded (outliers) and Fig. 5.14 shows the corresponding KDE for $v \sin i$ data.

Repeating the procedure, we constrain the evolution of λ as a function of α_{theo} is shown in Fig. 5.15.

5.3.3 Grid of optimal α for a real sample

For the Tarantula open cluster, PDFs from KDE, deconvolution via Tikhonov regularization and the solution by the Fredholm integral equation for $\alpha_{theo} = -0.5, 0, 0.5$ and 2 are displayed in Fig. 5.16.

To obtain the best α value, Fig. 5.17 represents the mean square error, yielding $\alpha_{min} = 0.07$, a value very close to 0 (an isotropic axial distribution).

For $\hat{f}_{true}(v, \alpha_{theo} = \alpha_{min})$, a bimodal Maxwellian distribution is fitted same as Ramírez-Agudelo et al. (2013) for comparison purposes, with our results yielding $C_1 = 0.51$, $C_2 = 0.49$, $\sigma_1 = 62$ $(km\ s^{-1})$ and $\sigma_2 = 172$ $(km\ s^{-1})$ with a least square regression value of 0.0001

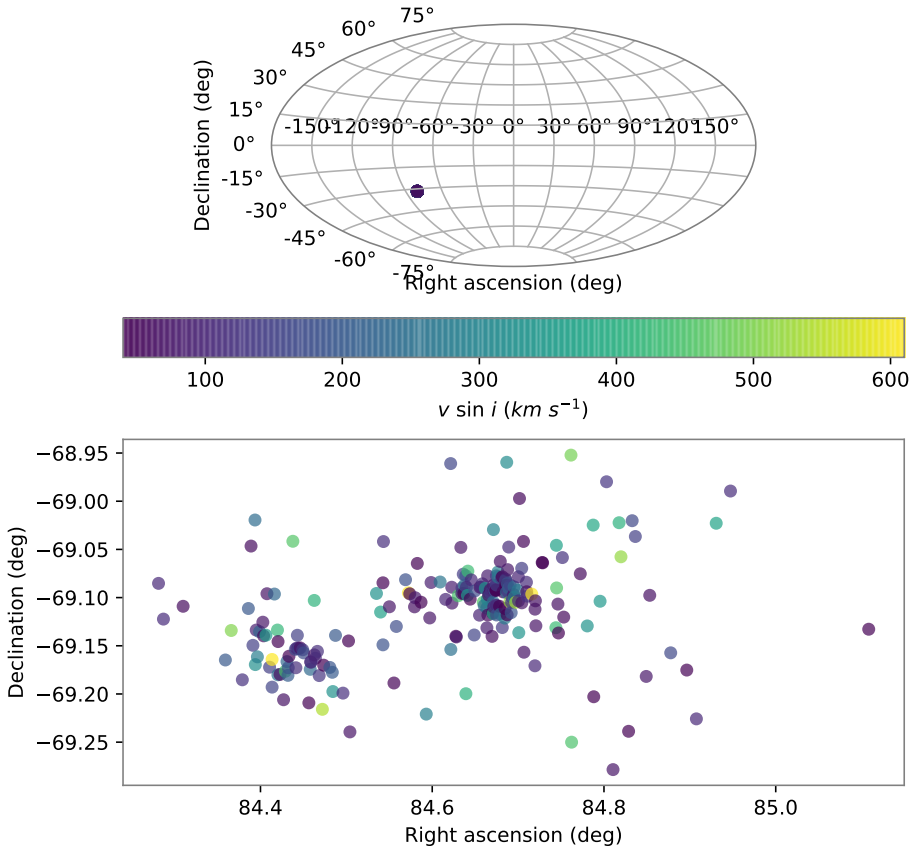

Figure 5.13: Spatial distribution of the open cluster as a function of the projected rotational velocity. The upper panel represent the galactic point-of-view and the bottom panel the zoom for the coordinates.

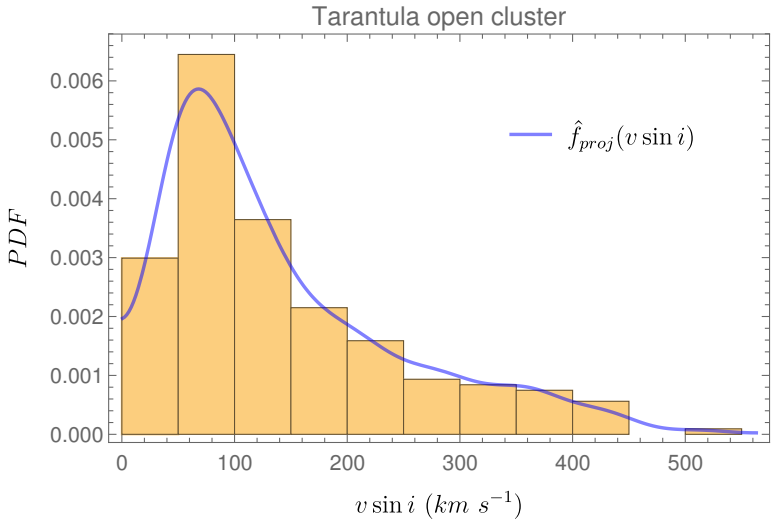

Figure 5.14: Kernel density estimator (blue curve) to $v \sin i$ data (histogram) for the Tarantula database.

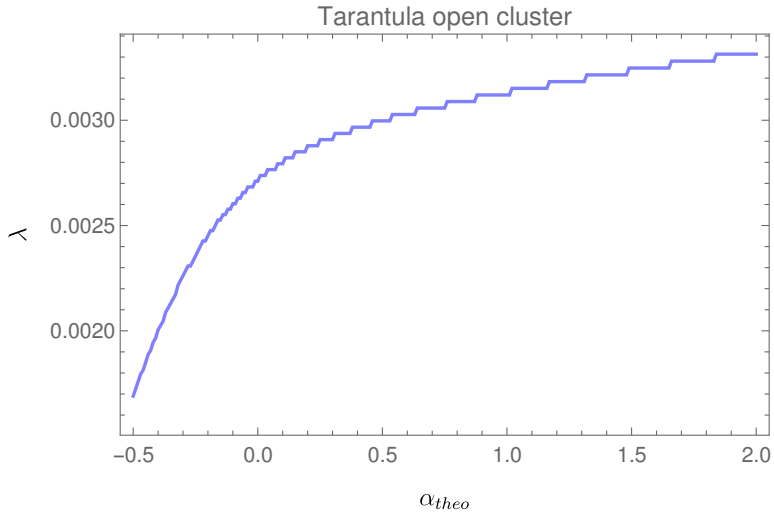

Figure 5.15: Regularization parameter as a function of α for the Tarantula database.

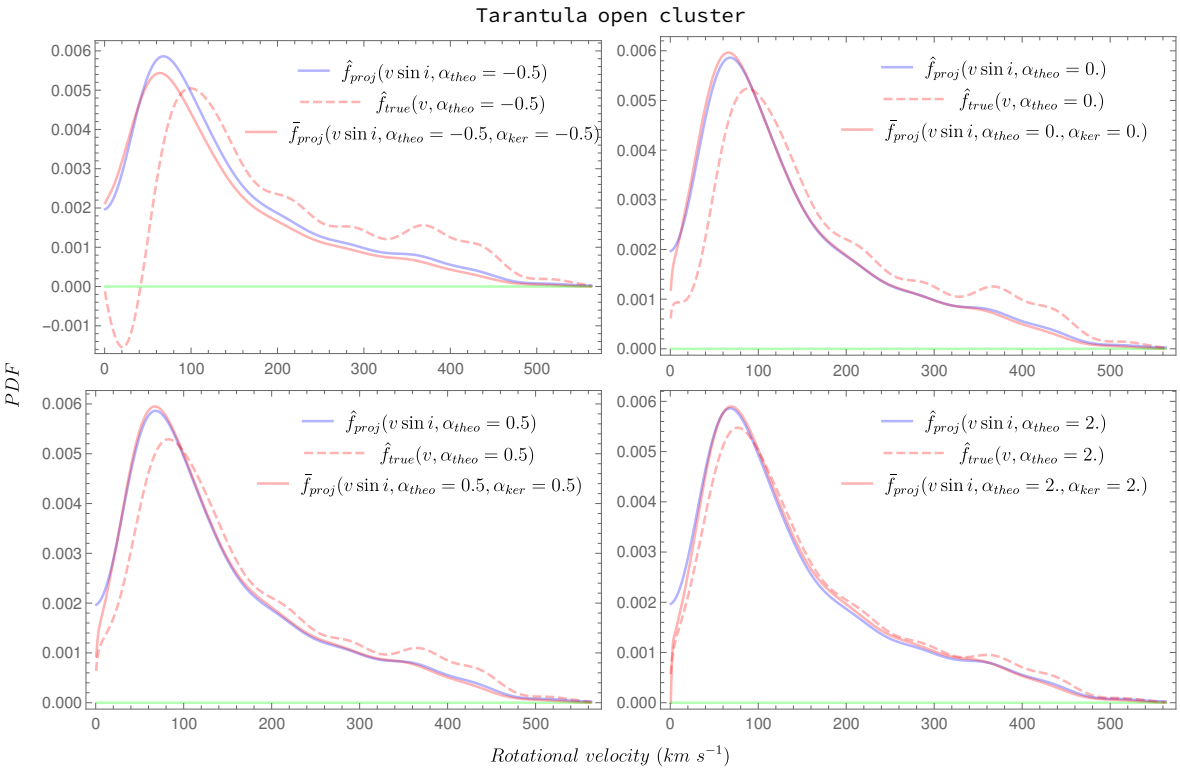

Figure 5.16: Kernel density estimator of the $v \sin i$ data (blue line) with the respective Tikhonov regularization PDF (red dashed line) and the solution by the Fredholm integral equation (red line) in the open cluster. There are four grid solution for $\alpha_{theo} = -0.5$ (top left panel), $\alpha_{theo} = 0$ (top right panel), $\alpha_{theo} = 0.5$ (bottom left panel) and $\alpha_{theo} = 2$ (bottom right panel).

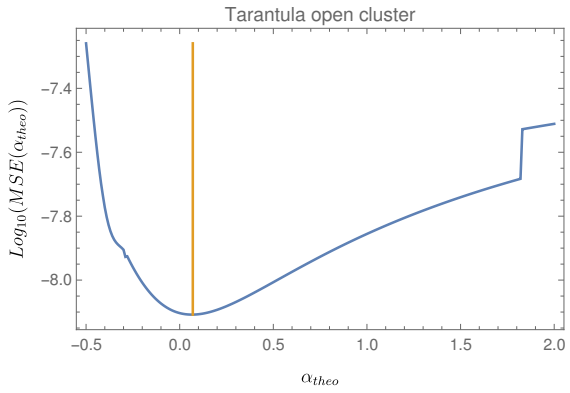

Figure 5.17: Mean square error in an open cluster (blue line). The orange vertical line represent the location of $\alpha_{min} = 0.07$.

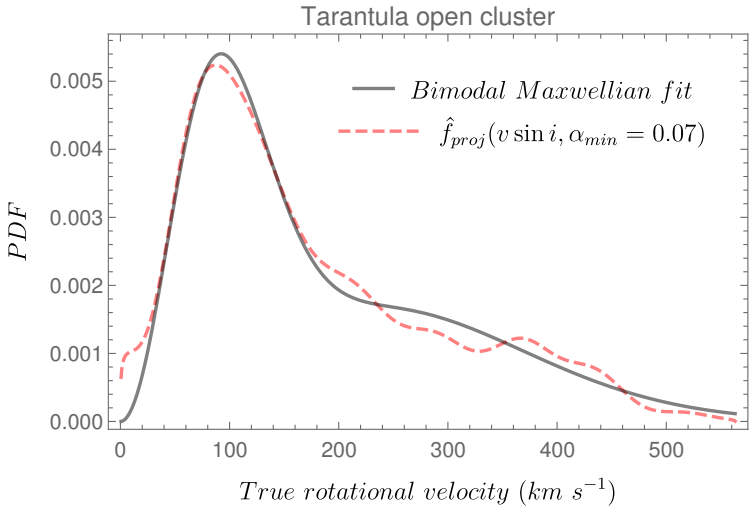

Figure 5.18: Best true rotational velocity PDF (red dashed line) with the best Bimodal Maxwellian distribution (black line) in the Tarantula open cluster.

5.3.4 Confidence intervals

Bootstrap random choice sample are repeated 1000 times for the sample of Ramírez-Agudelo et al. (2013) and the results to find the α_{min} using this method are described in Fig. 5.19. In the mean square error plot the percentiles shows different peaks and the histogram shows a poorly bimodality for $\alpha_{ker,min} < 0$.

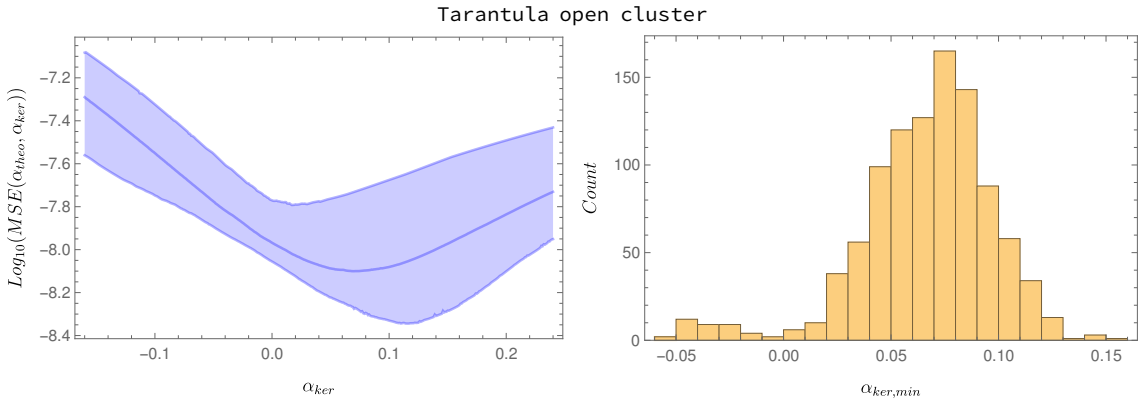

Figure 5.19: Bootstrap calculations give the mean square error in field stars (blue curve) with confidence intervals of 2.5 to 97.5% (left panel) and the respective histogram (right panel) for the Tarantula open cluster.

5.3.5 CDF correlation

Repeating the procedure from field stars, now in 30 Dor, CDF solutions (Tikhonov regularization and one step solution) are showed in Fig. 5.20. Both CDFs are almost identical and the q-q plot corroborate it.

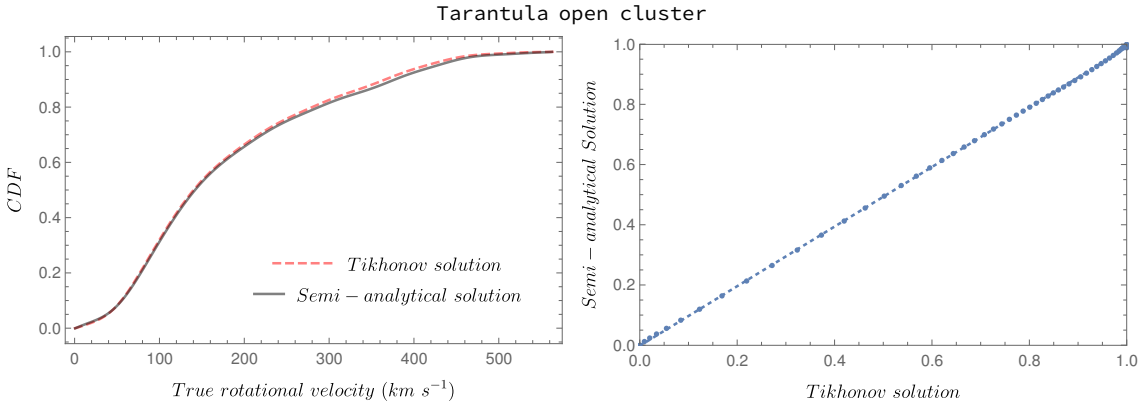

Figure 5.20: Best true rotational velocity CDF by Tikhonov regularization (red dashed line) with the semi-analytical solution (black line) in the left panel. The right panel shows the $q-q$ plot. This is for the Tarantula open cluster.

Similarity between both CDFs also is found, as resulted in the field stars. With this outcome it can be preliminarily concluded that our non-isotropic distribution of axes in both methods via Tikhonov and one step CDF analytical solution gives equivalent results.

5.4 Other samples

In order to extend the study to other open clusters, we only shows the results obtained from Mermilliod et al. (2009) in Table 5.4 and Corsaro et al. (2017) in Table 5.5 (without confidence/error intervals).

These results correspond to open clusters and the spin alignment obtained varies between $\alpha_{min} = -0.44$ to $\alpha_{min} = 1$. Remembering that our procedure can not model $\alpha \geq 1$, then for high non-isotropic distribution of axes using our method is still remains an open question. For Be field stars, Table 5.6 shows the values obtained for different databases of them. For this case we can appreciate that all cases yields $\alpha_{min} \geq 1$.

Any database of open cluster or field stars can be reproduced. In this work, we show these fews examples.

Cluster	$v \sin i$ range ($km\ s^{-1}$)	Number of stars	α_{min}
NGC 7092	3-41	24	-0.44
IC 2602	2-66	37	-0.4
IC 2391	3-67	30	-0.37
Alpha Persei	3-66	57	-0.27
NGC 752	0-52	87	-0.11
Pleiades	0-66	145	0.39
Coma Ber	0-35	64	0.43
NGC 1976	2-30	74	0.62
NGC 6475	1-68	74	≥ 1 ?
Blanco 1	0-69	150	≥ 1 ?
Hyades	1-65	156	≥ 1 ?
Praesepe	0-71	33	≥ 1 ?

Table 5.4: Spin alignment obtained in Mermilliod et al. (2009) database (open clusters).

Cluster	$v \sin i$ range ($km\ s^{-1}$)	Number of stars	α_{min}
NGC 6791	0-48	25	-0.44
NGC 6819	0-80	23	≥ 1 ?

Table 5.5: Spin alignment obtained in Corsaro et al. (2017) database (open clusters).

$v \sin i$ range ($km\ s^{-1}$)	Number of stars	α_{min}	Reference
45-311	49	≥ 1 ?	Arcos et al. (2018) (BeSOS 2.5$\sigma_{fit,crit}$)
45-301	49	≥ 1 ?	Arcos et al. (2018) (BeSOS 3$\sigma_{fit,crit}$)
56-307	49	≥ 1 ?	Arcos et al. (2018) (BeSOS 2$\sigma_{fit,crit}$)
5-500	616	≥ 1 ?	Neiner et al. (2011) (BeSS)
18-422	462	≥ 1 ?	Yudin (2001)
10-440	233	≥ 1 ?	Zorec et al. (2016)

Table 5.6: Non-isotropy obtained for different Be field stars databases.

5.5 Summary

The entire procedure to obtain $v \sin i$ for different epochs and lines is applied to the BeSOS database. Arcos et al. (2018) obtained the projected rotational velocities for these Be stars using stellar atmosphere models with the line 4471.48 $(\AA)$ at a single epoch. Our method is in global agreement with those results with a few exceptions that should be study deeper. In this chapter we only show the HeI theoretical lines of $\lambda\lambda$4387.94, 4471.48 and 4713.14 $(\AA)$ for HD205637 BeSOS spectra (taken at 00:46:43, on 11-14-2012).

Two databases are showed to obtain the non-isotropic parameter, 11881 F- and G-type field stars from Nordström et al. (2004), and 216 O- and B-type stars for open cluster from Ramírez-Agudelo et al. (2013). For the field stars a very isotropic behavior is obtained, with $\alpha_{min} = -0.03$. For the open cluster there is no spin alignment found with $\alpha_{min} = -0.013$ and this could be because there are mainly two different spatial concentration of stars that could affect the final result. The method is applied to more databases, as 12 open clusters (Mermilliod et al., 2009), 23 and 25 red giant stars (Corsaro et al., 2017) and Be field stars (Yudin, 2001; Neiner et al., 2011; Zorec et al., 2016; Arcos et al., 2018) represented in Tables 5.4, 5.5 and 5.6.

CHAPTER 6

Discussion

Discuss and future development of our theoretical modeling, MC simulations and results are described here. Firstly, the way to obtain $v \sin i$ via FT in an automated way is discussed in section 6.1. Secondly, the non-isotropic distribution of axes using deconvolution via Tikhonov regularization in the Fredholm integral is commented in section 6.2. Finally, future works are showed in 6.3.

6.1 Measuring $v \sin i$

Our automatic method to obtain $v \sin i$ is useful to analyze several absorption lines in any normalized spectra at different epochs. Here, we only analyzed 64 stars with a total of 314 spectra (BeSOS) however this can be applied to different databases. The code is not computationally expensive. Nevertheless, a MC simulations must be performed to analyze the behavior of the numerical routine. For the grid of theoretical velocities ($\langle v \sin i \rangle_{theo}$), this was constructed for 100 ($km\ s^{-1}$) to 600 ($km\ s^{-1}$) in steps of 10 ($km\ s^{-1}$), another grid of noise added (σ_{noise}) for 0.001 to 0.01 in steps of 0.001, and windows of $\pm$ 2.0 to 3.0 in steps of 0.5 (σ_{fit}) with respect to the mid Gaussian fit (λ_{fit}) for 10000 MC repetitions in each one. BeSOS spectra (with PUCHEROS instrument) has wavelength steps ($\Delta\lambda$) of 0.089 $\AA$. Together with our five criteria to verify a good absorption line, a sixth criteria is added for the 10000 MC simulations. It is necessary to apply this procedure to more instruments with different spectral resolution, then

it is essential to compute a MC simulations to reproduce observations and establish the 6th criteria of "good" absorption lines. This method should be applied to other spectrographs, like FLAMES[1] (spectral resolution $\sim$ 43000) and/or UVES[2] (spectral resolution $\sim$ 80000), among many others.

For spectra with $\Delta\lambda = 0.089$ $\mathring{A}$ (BeSOS database), theoretical line profiles convolved with rotational velocities lesser than 60 $km\ s^{-1}$ (results not showed in this thesis) the FT can not convert to the frequencies domain, this is due to numerical instabilities Sundqvist et al. (2013). We only analyzed Be stars that are fast rotators, in which there are only a few $v \sin i$ obtained with our method with values lesser than 60 $km\ s^{-1}$. For instruments with higher resolution, it is possible to convolve successfully for theoretical velocities $> 10\ km\ s^{-1}$ (not showed here), as UVES, and therefore, $v \sin i$ data can be derived for low mass stars (slow rotators).

A variable that needs to be studied further is the limb darkening parameter ϵ. We used $\epsilon = 0.6$ but we are currently making a grid for all the possible values to analyze if there is a important effect to consider in future studies. Moreover, we used a linear limb darkening law but there exist other limb darkening laws as the quadratic, square-root and logarithmic. Levenhagen (2014) developed a C code (named ZPEKTR) that evaluate the effects of limb darkening and gravity darkening. He obtained the $v \sin i$ values from Achernar (a high rotator Be star) and concluded that it is necessary to take into consideration the gravity darkening because, otherwise, the values are underestimated. Currently just established a collaboration with him.

The noise added to the theoretical rotationally convolved absorption lines, σ_{noise}, comes from a Gaussian distribution. This type of noise is very symmetric and other types of distributions should be studied. As a first approximation, the error considered here reproduce well data from BeSOS but it does not do it in a perfect way.

For the Be stars in study, our $v \sin i$ values are comparatively close to Arcos et al. (2018) and Frémat et al. (2005) in most cases. They used stellar atmosphere models using the 4471.48 ($\mathring{A}$) absorption line and we applied the FT method to 9 HeI lines: $\lambda\lambda 4387.93, 4437.55, 4471.48, 4713.14, 4921.93, 5015.67, 5047.74, 5875.63$ and $6678.15\ (\mathring{A})$. An upgrade of the method can be developed to other types of stars (with different lines), but other variables has to be taken into account, as macroturbulence in slow rotators, asymmetric windows, and remove unexpected peaks and cosmic rays.

Typical studies in Be stars use the HeI 4471.48 ($\mathring{A}$) to obtain $v \sin i$ via FT. We stud-

[1] https://www.eso.org/public/teles-instr/paranal-observatory/vlt/vlt-instr/flames/

[2] https://www.eso.org/public/teles-instr/paranal-observatory/vlt/vlt-instr/uves/

ied this line, together with eight more HeI lines, obtaining different results for each one. Since we have an automatic procedure to obtain the $v \sin i$ values, our goal now is to analyze if HeI 4471.48 ($\AA$) line underestimate/overestimate with respect to other lines or/and the average of the epoch. For a more complete study, other lines should be included, as CII 4267 line that appears in Achernar for example. Other typical line seen in Be stars is HeI 4921 (see Neiner et al., 2002).

A very important work from Reiners & Schmitt (2002) and Reiners (2003) studying the zero position of the FT frequencies domain in modeled spectra for rotating stars, they found an interesting relation between the ratio for the zeros and the differential rotation of a star. In our entire work, we set the star as a rigid rotator. Implement the differential rotation using FT can be important to understand if there is a influence that we should take into account.

6.2 Non-isotropic distribution of stellar axes via Tikhonov regularization

A non-parametric fit to compute the observed data is given by a KDE, using a Gaussian kernel. There are others like the uniform, triangular, biweight, triweight, Epanechnikov, among others. These others kernel can be used to compare results in simulations. Also, the bandwidth to smooth the function is important to take into account. Curé et al. (2014) used two types of bandwidths (one of them used here) and found no comparatively difference but still it could be improved in simulations. The KDE is very sensible to the limits in which the fit is performed and should be computed more limits to work on. Moreover, Wand & Jones (1994) estimate the KDE with data that are measured with some non-negligible error. This last is a problem of considerable practical interest that can be essential to implement in this type of study.

We computed the L-curve to find the Tikhonov factor, but we discarded the method because the "L" shape was not obtained despite to have similar results from our iterative method from Christen et al. (2016). We also deconvolved using the MATLAB package of Hansen (2010) the projected rotational velocity PDF via maximum entropy method (not showed here), the goal was to show that the procedure works on an astrophysical context and to make more statistical studies, this methods, can be implemented, comparing with the Lucy-Richardson deconvolution. Having this, we will have a total of 3 different deconvolution methods; Tikhonov regularization

(with Tikhonov factor from our method and L-curve method), Maximum Entropy (with Tikhonov factor from our method and L-curve method) and Lucy-Richardson method. We use the first method mentioned before but not with the L-curve method.

One way to find the best α is with the MSE function (this thesis), but apart from this, we calculated another minimization method using the Mellin Transform to the Fredholm integral equation. The results for both minimization were in global agreement. There is an intention to continue delving into this new minimization method for future projects.

Most of deconvolutions for low α_{theo} values presented negative PDFs (not showed here), especially for $0 \leq \alpha_{theo}$, and one representative case is the database from Yudin (2001) with $\alpha_{theo} = 0$. From that negatives PDFs we infer that the model we implemented can not properly describe this database sample.

In Be stars, a crucial parameter is the critical rotation. Zorec et al. (2016) pointed out the equatorial rotational velocities PDFs from the ratio of the projected rotational velocity with respect to the critical rotation. This procedure is important for future studies to analyze if there is any correlation between these parameters.

Our angles generator has dependence on α and more proposals can be developed to extend the form of the kernel in Fredholm integral equation for a non-isotropic distribution of stellar axes. Furthermore, there are more ways to simulate the equatorial rotational velocities (we only used uni/bi-modal Maxwell and Kaniadakis distribution), Tsallis, Normal, etc.

The procedure to find the best α value is given by the flowchart in Fig. 3.3, however, an improvement can be developed using the CDF solution for a grid of α values without the use of PDFs and similar results should be appear.

As a future work, we want to establish a relation from the paper Jackson & Jeffries (2010), "Are the spin axes of stars randomly aligned within a cluster?", with our model.

In MC simulations, the plot of λ as a function of α_{theo} (Figs. 4.10 and 4.13) shows that the Tikhonov factor starts to be constant as α_{theo} increases. In general, for $\alpha_{theo} \geq 1$, $\hat{f}_{proj}(v \sin i, \alpha_{theo})$ is similar to $\hat{f}_{true}(v, \alpha_{theo})$, that is why it is unnecessary to deconvolve for high α_{theo} and our model is not correct for these samples. An important correlation found was that the scale of λ is lower for low rotator stars and higher for high rotator stars and thus for low rotator stars the numerical procedure to obtain the Tikhonov factor should be more precisely. An example of this statement is the decay of the Tikhonov factor for $\alpha_{theo} > 1.3$ in the deconvolution for the 11818 field stars (see Fig.

5.7).

The simulations shows the reliability of the method and for equatorial rotational velocities generated by the bimodal Maxwellian distribution, the deconvolution does not reproduce well in comparison to the analytical solution for low velocities. Apart from this a difference between the samples length equal to 50 and 200. For sample lengths equal to 50, α_{min} exhibits a large variation for the quantiles 0.025 and 0.975 with respect to the equal to 200, being the quantile 0.5 very similar, as expected.

In one hand the deconvolution for Geneva-Copenhagen survey field stars (Nordström et al., 2004; Holmberg et al., 2007) at any α_{theo} evidence several peaks. This could be due to numerical issues for the MATLAB package (Hansen, 2010). On the other hand, the result obtained from our method is very close to an isotropic axes distribution, being an expected result for $\sim$ 12000 field stars.

In Ramírez-Agudelo et al. (2013) paper, a double peak in the equatorial rotational distribution is obtained, same as our results. Nevertheless, in the MSE plot, a "gap" is derived. This is generated by numerical instabilities. The location in the stars of the Tarantula open cluster are distributed in two different locations. The $\alpha_{min} = 0.07$ is very close to an isotropic distribution of axes and a study for those separated concentration can be performed to determine if there is spin alignment in each location.

Curé et al. (2014) proved that the semi-analytical expresion for the CDF is a very good result. We extended the study of the CDF by a non-isotropic distribution axes for the projected rotational velocities and we also obtained concordant results.

Corsaro et al. (2017) demonstrated that the distribution of axes of rotating stars are not isotropically (with only 48 stars in two clusters), we contribute in the context of distributions using the Fredholm integral equation. More studies are necessary to analyze if there is a correlation between the spin alignment of a cluster and the age, metallicity, number of stars, spectral distribution, magnitude, etc. The case of α_{min} obtained in the databases of Mermilliod et al. (2009) and Corsaro et al. (2017) the values varies between -0.44 and ≥ 1

For Be field stars, every value of α_{min} shows a strong non-isotropic. Gravity darkening effects should be computed to these $v \sin i$ values of Be stars to see if there is a influence.

Since the procedure to obtain the non-isotropic distribution of axes is applicable for any database of rotating stars, MC simulations for the best fit distribution of $v \sin i$ obtained must be computed to see if the result yielded is consistent. Same as 30 Dor and the simulations given by the bimodal Maxwellian.

6.3 Other applications and future works

6.3.1 Mass ratio function distribution in binaries

Instead of the projected rotational velocity data, in binaries of exoplanet-star or/and star-star there is possible to obtain the mass distribution which depends on the constituent mass of system and the orbital inclination angle. There have been previous studies in this topic (Curé et al., 2015; Ananyeva et al., 2019), however, not in a non-isotropic description using the Fredholm integral equation. We pretend to work on this in the future with data from the NASA Exoplanet archive[3].

6.3.2 Non-isotropical modeling with 2 parameters

To add a second parameter to the non-isotropic stellar distribution axes in the Fredholm integral equation, we propose

$$H(z) = c_{\alpha,\beta}(1-z^2)^{\alpha} z^{2\beta}, \tag{6.1}$$

which results in the following Fredholm integral

$$f_{proj}(y,\alpha,\beta) = c_{\alpha,\beta}\int_y^{\infty} \frac{y^{1+2\alpha}}{x^{1+2\alpha+2\beta}(x^2-y^2)^{1/2+\beta}} f_{true}(x,\alpha,\beta)dx, \tag{6.2}$$

where

$$c_{\alpha,\beta} = \frac{2}{B(\alpha+1,\beta+1/2)}. \tag{6.3}$$

We guess that is possible to model the bimodality angle distribution from NGC 6819 in Corsaro et al. (2017), among others. This is because using only the parameter α gives an unimodality in the distribution of axes to model the non-isotropy for rotating stars while adding this new β parameter, more complex multimodal distributions can be generated.

[3] `https://exoplanetarchive.ipac.caltech.edu/`

CHAPTER 7

Conclusions

Stellar rotation is a fundamental parameter to constrain models of stellar formation and evolution. There is a wide field of research regarding stellar rotation, evolution and internal mechanism, gravity darkening, differential rotation, magnetic fields, angular momentum, convection/radiation energy transport, stellar oscillations, chemical mixing, mass-loss, rotation braking, etc. Our focus is the study of projected and true rotational velocity of stars, defined as v and $v \sin i$, respectively where v is the velocity on surface at latitude 0^o and i is the inclination angle of the stellar rotational axis with respect to the line of sight. This master's thesis is primarily divided in two sections, derivation of $v \sin i$ value via Fourier Transform (FT) method using an automated procedure for different lines and epochs (***C.1***), and the non-isotropical rotational velocity distribution for different databases of a group of stars using a Fredholm integral equation (***C.2***). In this section we summarize the investigation and conclusions.

C.1: As Doppler effects broad the intrinsic line profile for an atomic transition from a star described via a convolution, it is possible to measure $v \sin i$ data via FT technique because in high rotator stars, not only as Be stars, the broadening of the line is mainly dominated by rotation being the other effects neglectable (as micro-macroturbulence, microturbulence, instrumental errors, etc). From the new domain of frequencies of the FT, using a linear limb darkening law with a limb darkening parameter $\epsilon = 0.6$, the first zero yields the value of the pro-

jected rotational velocity (Carroll, 1933; Carroll & Ingram, 1933). We performed an automated numerical code that gives the $v \sin i$ value for some selected absorption line profiles. In our case, because we are working with Be stars, these lines are HeI $\lambda\lambda$ 4387.93, 4437.55, 4471.48, 4713.14, 4921.93, 5015.67, 5047.74, 5875.63 and 6678.15 $(\AA)$: the different window sizes to select the bandwidth of the signal from the area inside a Gaussian fit. Yet, before to work on BeSOS spectra, we perform random sampling repetitions for different velocities and synthetic noise added to the lines. Having initially five criteria to define a "good" line, namely; i) numerical fit of a Gaussian profile, ii) there is an absorption line, iii) the center of the fit is not shifted with respect to the theoretical one, iv) the noise in the continuum is not significantly and v) the dispersion of the Gaussian fit is not larger in comparison with the absorption line resolution. The simulated lines forced us to define a sixth criteria in which there is necessary to measure the standard deviation of the continuum and if it is higher than a certain threshold then is not considered as a "good" line. The procedure is applied to BeSOS database for 64 stars with a total of 314 different spectra. The results are in global agreement in comparison with Arcos et al. (2018) and Frémat et al. (2005), with some discrepancy in a few projected rotational velocities. However, our method includes 9 different HeI lines for different epochs. Alternatively to this, Levenhagen (2014) developed a C code, called ZPEKTR, that computes the gravity darkening effect for high rotational stars and we intend to implement this to model our BeSOS stars to obtain more reliable $v \sin i$ values.

C.2: Since it is possible to measure $v \sin i$ for a certain group of stars (open clusters or field stars), Chandrasekhar & Münch (1950) proposed a Fredholm integral equation, assuming an isotropical distribution of axes for rotating stars, that relates the true and equatorial rotational velocity distributions. We add a parameter α to the kernel of the Fredholm integral that models the non-isotropic distribution of axes. When the α parameter is in the range $-1 < \alpha < 0$, the values of i concentrated near to $i \sim 0^o$ when $\alpha > 0$, the same value of i is distributed close to the equator ($i \sim 90^o$) and the case $\alpha = 0$ gives an isotropic distribution of axes (with respect to the line of sight). In order to obtain the non-isotropy for a database of stars, first it is necessary to compute the Kernel Density Estimator (KDE) for the sample of $v \sin i$ using a Gaussian kernel with a bandwidth given by Silverman (1986). This function is known as $\hat{f}_{proj}(v \sin i, \alpha)$. After this, a deconvolution via Tikhonov regularization is computed (Hansen, 2010) obtaining the distribution for equatorial rotational velocities $\hat{f}_{true}(v, \alpha)$. Having this true equatorial distribution it is possible to solve the Fredholm integral equation for

a grid of α, called α_{ker} in order to obtain the best $\alpha-$ parameter for the sample. This solution is denominated $\bar{f}_{proj}(v \sin i, \alpha, \alpha_{ker})$ and is compared with $\hat{f}_{proj}(v \sin i, \alpha)$ the resulting mean square error gives the non-isotropy for the best α value as α_{min}. We performed Monte Carlo simulations and, in general terms, our numerical procedure is reliable for $\alpha < 1$, which means that there is only possible to estimate distribution of axes for inclination angles in databases that are highly concentrated near to group of stars with $i \sim 0^o$, isotropic distribution and measurably close to the equator ($i \sim 90^o$) with respect to the observer (this last measurably, see Fig. 2.5). We applied this method to different samples of stars, as low rotators field stars (Nordström et al., 2004), open clusters (Mermilliod et al., 2009; Ramírez-Agudelo et al., 2013; Corsaro et al., 2017) and Be field stars (Yudin, 2001; Zorec et al., 2016; Neiner et al., 2011; Arcos et al., 2018). For the $\sim$ 12000 samples of slow rotator field stars (F- and G-spectral type), a very close to isotropic value is encountered $\alpha_{min} = -0.03$. In open cluster samples, a large dispersion for α_{min} is obtained, between -0.44 and 1. Remembering that results for $\alpha_{min} > 1$ are uncertain, for all different Be field stars samples, this $\alpha_{min} = 1$ is obtained and more in-depth studies on measuring $v \sin i$ should be done for high rotator star samples that include gravity darkening effects. For the case of NGC 6819 in Corsaro et al. (2017), a bimodal projected stellar-spin inclination angles are observed and for our case, it not possible no model this bimodality. That is why adding a β parameter to the Fredholm integral equation it can be possible to compute more complex distributions of $v \sin i$ values and extend this study of projected and true rotational velocities for different databases.

Future works on stellar rotations are under development.

APPENDIX A

Fourier Transform

A.1 Definition

A complex function, $f(\psi)$, that satisfy the following properties:

(a) Is integrable, i.e., $\int_{-\infty}^{\infty} |f(\psi)| d\psi < \infty$,

(b) Contain only finite discontinuities,

therefore a complex FT operator ($\mathscr{F}$) can be applied for f(ψ). This transformation is defined by

$$\mathscr{F}\{f(\psi)\} = \hat{f}(\phi) = \int_{-\infty}^{\infty} f(\psi) e^{-2\pi j \psi \phi} d\psi, \tag{A.1}$$

where ψ is the time (or space) domain, ϕ is the new domain of frequencies and $j = \sqrt{-1}$. The FT of $f(\psi)$ is denoted by $\hat{f}(\phi)$, where the product of ψ and ϕ is dimensionless. The inverse FT ($\mathscr{F}^{-1}$) of $\hat{f}(\phi)$ yield

$$\mathscr{F}^{-1}\{\hat{f}(\phi)\} = f(\psi) = \int_{-\infty}^{\infty} \hat{f}(\phi) e^{2\pi j \psi \phi} d\phi, \tag{A.2}$$

resulting the same original function $f(\psi)$, being the inverse FT operator of $\mathscr{F}$.

A.2 Basic properties

Let a be a constant, $f_1(\psi)$ and $f_2(\psi)$ functions that satisfy (a) and (b), in Table A.2 the most fundamentals properties for the FT are listed

Theorem	Initial function	Fourier Transform
Linearity	$af_1(\psi) + af_2(\psi)$	$a\hat{f}_1(\psi) + a\hat{f}_2(\psi)$
Shift	$f_1(\psi - a)$	$e^{-2\pi ja\psi}\hat{f}_1(\psi)$
Similarity	$f_1(a\psi)$	$\frac{1}{\|a\|}\hat{f}_1(\frac{\psi}{a})$
Derivative	$\frac{df_1(\psi)}{d\psi}$	$2\pi j\phi\hat{f}_1(\phi)$
Duality	$\hat{f}_1(\psi)$	$f_1(\phi)$

Table A.1: Properties of FT. The first column represent the name of the property, the second column is the function in which the FT operator is applied and the third column yield the resulting function.

A.3 Convolution theorem

Recalling that $f_1(\psi)$ and $f_2(\psi)$ given by:

$$f_1(\psi) = \mathscr{F}^{-1}\{\hat{f}_1(\phi)\} = \int_{-\infty}^{\infty} \hat{f}_1(\phi)e^{2\pi j\psi\phi}d\phi, \tag{A.3}$$

and

$$f_2(\psi) = \mathscr{F}^{-1}\{\hat{f}_2(\phi)\} = \int_{-\infty}^{\infty} \hat{f}_2(\phi)e^{2\pi j\psi\phi}d\phi, \tag{A.4}$$

thus a powerful theorem in the FT context called convolution theorem can be apply, which is described by

$$f_3(\psi) = f_1(\psi - \psi') * f_2(\psi') = \int_{-\infty}^{\infty} f_1(\psi - \psi')f_2(\psi')d\psi', \tag{A.5}$$

where $f_3(\psi)$ is the resulting convolution between the point-wise product of f_1 and f_2. The eq. A.5 can be written as

$$f_3(\psi) = \int_{-\infty}^{\infty} f_2(\psi')[\int_{-\infty}^{\infty} \hat{f}_1(\phi)e^{2\pi j\phi(\psi-\psi')}d\phi]d\psi' = f_1(\psi - \psi') * f_2(\psi'), \tag{A.6}$$

and changing the order of integration the convolution gives

$$f_3(\psi) = \int_{-\infty}^{\infty} \hat{f}_1(\phi)[\int_{-\infty}^{\infty} f_2(\psi')e^{-2\pi j\phi\psi'}d\psi']e^{2\pi j\phi\psi}d\phi = f_1(\psi-\psi') * f_2(\psi'), \tag{A.7}$$

$$f_3(\psi) = \int_{-\infty}^{\infty} \hat{f}_1(\phi)\hat{f}_2(\phi)e^{2\pi j\phi\psi}d\phi = f_1(\psi-\psi') * f_2(\psi'), \tag{A.8}$$

$$f_3(\psi) = \mathscr{F}^{-1}\{\hat{f}_1(\phi)\hat{f}_2(\phi)\} = f_1(\psi-\psi') * f_2(\psi'). \tag{A.9}$$

Thus, applying the FT, we obtain

$$\mathscr{F}\{f_3(\psi)\} = \mathscr{F}\{f_1(\psi-\psi') * f_2(\psi')\} = \mathscr{F}\{\mathscr{F}^{-1}\{\hat{f}_1(\phi)\hat{f}_2(\phi)\}\}, \tag{A.10}$$

$$\mathscr{F}\{f_3(\psi)\} = \mathscr{F}\{f_1(\psi-\psi') * f_2(\psi')\} = \hat{f}_1(\phi)\hat{f}_2(\phi), \tag{A.11}$$

$$\mathscr{F}\{f_3(\psi)\} = \mathscr{F}\{f_1(\psi-\psi') * f_2(\psi')\} = \mathscr{F}\{f_1(\psi)\}\mathscr{F}\{f_2(\psi)\}, \tag{A.12}$$

$$\hat{f}_3(\psi) = \mathscr{F}\{f_1(\psi-\psi') * f_2(\psi')\} = \mathscr{F}\{f_1(\psi)\}\mathscr{F}\{f_2(\psi)\}, \tag{A.13}$$

eq. A.13 tell us that the FT of the convolution between $f_1(\psi-\psi')$ and $f_2(\psi')$ can be traduced as the product of the FT of $f_1(\psi)$ and $f_2(\psi)$.

A.4 Discrete Fourier Transform

The astronomical observations usually are periodic and discrete data samples. Also, the analytical expression of the signal function is unknown and there is necessary to recover the continuous FT into a discrete version, which is defined as

$$\hat{x}_k = \mathscr{F}\{x_n\}, \tag{A.14}$$

$$\hat{x}_k = \sum_{n=0}^{N-1} x_n e^{-2\pi jnk/N}, \tag{A.15}$$

where there are N uniformly data sample points x_n ($n = 0, 1, 2, ..., N-1$) and the discretized, $\hat{x}_k$ ($k = 0, 1, 2, ..., N-1$), represent the FT of x_n. It is important to note that this equation is represented in a matrix form by

$$\begin{pmatrix} \hat{x}_0 \\ \hat{x}_1 \\ \hat{x}_2 \\ \vdots \\ \hat{x}_{N-1} \end{pmatrix} = \begin{bmatrix} 1 & 1 & 1 & \cdots & 1 \\ 1 & e^{-2\pi j} & e^{-4\pi j} & \cdots & e^{-2\pi j(N-1)} \\ 1 & e^{-4\pi j} & e^{-8\pi j} & \cdots & e^{-4\pi j(N-1)} \\ \vdots & \vdots & \vdots & \ddots & \vdots \\ 1 & e^{-4\pi j(N-1)} & e^{-8\pi j(N-1)} & \cdots & e^{-2\pi j(N-1)^2} \end{bmatrix} \begin{pmatrix} x_0 \\ x_1 \\ x_2 \\ \vdots \\ x_{N-1} \end{pmatrix}. \tag{A.16}$$

The inverse Discrete FT for $\hat{x}_k$ is

$$x_n = \mathscr{F}^{-1}\{\hat{x}_k\}, \tag{A.17}$$

$$x_n = \frac{1}{N}\sum_{k=0}^{N-1} \hat{x}_k e^{2\pi jnk/N}, \tag{A.18}$$

and the respective matrix representation is

$$\begin{pmatrix} x_0 \\ x_1 \\ x_2 \\ \vdots \\ x_{N-1} \end{pmatrix} = \frac{1}{N}\begin{bmatrix} 1 & 1 & 1 & \cdots & 1 \\ 1 & e^{2\pi j} & e^{4\pi j} & \cdots & e^{2\pi j(N-1)} \\ 1 & e^{4\pi j} & e^{8\pi j} & \cdots & e^{4\pi j(N-1)} \\ \vdots & \vdots & \vdots & \ddots & \vdots \\ 1 & e^{4\pi j(N-1)} & e^{8\pi j(N-1)} & \cdots & e^{2\pi j(N-1)^2} \end{bmatrix} \begin{pmatrix} \hat{x}_0 \\ \hat{x}_1 \\ \hat{x}_2 \\ \vdots \\ \hat{x}_{N-1} \end{pmatrix}, \tag{A.19}$$

A.5 Fast Fourier Transform

To estimate the Discrete FT in a computer, there is necessary to make N^2 calculations, denoted by $\mathcal{O}(N^2)$. To reduce the computational time, the Fast FT is applied, which is a revolutionary method that make $\mathcal{O}(N\log_2 N)$ calculations (Cooley & Tukey, 1965; Bluestein, 1970). As an example, if there are $N = 10^6$ samples to transform, then the calculations are $\mathcal{O}(N^2) = 10^{12}$ and $\mathcal{O}(N\log_2 N) = 20 \times 10^6$. This algorithm yield an improvement of 5×10^4 times!

The FT is one of the most important theorems of the XIX century and for deeper information of the FT theorem visit Arfken & Weber (1995).

Bibliography

Abel N., 1826, Journal für die reine und angewandte Mathematik, 1, 153

Ananyeva V. I., Tavrov A. V., Venkstern A. A., Churbanov D. V., Shashkova I. A., Korablev O. I., Bertaux J. L., 2019, Solar System Research, 53, 124

Arcos C., Kanaan S., Chávez J., Vanzi L., Araya I., Curé M., 2018, MNRAS, 474, 5287

Arfken G. B., Weber H. J., 1995, Mathematical methods for physicists; 4th ed. Academic Press, San Diego, CA

Astropy Collaboration et al., 2013, A&A, 558, A33

Ballot J., García R. A., Lambert P., 2006, MNRAS, 369, 1281

Beck P. G. et al., 2012, Nature, 481, 55

Benomar O., Takata M., Shibahashi H., Ceillier T., García R. A., 2015, MNRAS, 452, 2654

Bertero M., Mol C. D., Pike E. R., 1988, Inverse Problems, 4, 573

Bi H., Boerner G., 1994, A&AS, 108, 409

Bluestein L., 1970, IEEE Transactions on Audio and Electroacoustics, 18, 451

Bouhamidi A., Jbilou K., 2007, Journal of Computational and Applied Mathematics, 206, 86

Brahm R., Jordán A., Espinoza N., 2017, PASP, 129, 034002

Brandner W., Grebel E. K., Barbá R. H., Walborn N. R., Moneti A., 2001, AJ, 122, 858

Bruning D. H., 1981, ApJ, 248, 274

Carroll J. A., 1933, MNRAS, 93, 478

Carroll J. A., Ingram L. J., 1933, MNRAS, 93, 508

Carvalho J. C., do Nascimento J. D., Silva R., DeMedeiros J. R., 2009, ApJ, 696, L48

Chandrasekhar S., Münch G., 1950, ApJ, 111, 142

Chauville J., Zorec J., Ballereau D., Morrell N., Cidale L., Garcia A., 2001, A&A, 378, 861

Christen A., Escarate P., Curé M., Rial D. F., Cassetti J., 2016, A&A, 595, A50

Cochetti Y. R., Arcos C., Kanaan S., Meilland A., Cidale L. S., Curé M., 2019, A&A, 621, A123

Collins I., George W., 1987, in Slettebak A., Snow T. P., eds, IAU Colloq. 92: Physics of Be Stars, p. 3

Conti P. S., Ebbets D., 1977, ApJ, 213, 438

Cooley J. W., Tukey J. W., 1965, Math. Comput., 19, 297

Corsaro E. et al., 2017, Nature Astronomy, 1, 0064

Curé M., Rial D. F., Cassetti J., Christen A., Boffin H. M. J., 2015, A&A, 573, A86

Curé M., Rial D. F., Christen A., Cassetti J., 2014, A&A, 565, A85

Deng L.-J., Huang T.-Z., Zhao X.-L., Zhao L., Wang S., 2013, J. Opt. Soc. Am. A, 30, 948

Deutsch A. J., 1970, in Slettebak A., ed, IAU Colloq. 4: Stellar Rotation, p. 207

Díaz C. G., González J. F., Levato H., Grosso M., 2011, A&A, 531, A143

Diaz-Cordoves J., Gimenez A., 1992, A&A, 259, 227

Domiciano de Souza A., Zorec J., Jankov S., Vakili F., Abe L., Janot-Pacheco E., 2004, A&A, 418, 781

Edmonds S. M., 1977, The Mathematical Gazette, 61, 74–75

Evans C. J. et al., 2011, A&A, 530, A108

Fomel S., 2007, Geophysics, 72, A29

Frémat Y., Neiner C., Hubert A. M., Floquet M., Zorec J., Janot-Pacheco E., Renan de Medeiros J., 2006, A&A, 451, 1053

Frémat Y., Zorec J., Hubert A. M., Floquet M., 2005, A&A, 440, 305

Fukue J., Akizuki C., 2006, PASJ, 58, 1039

Gray D. F., 2005, The Observation and Analysis of Stellar Photospheres

Grebel E. K., Chu Y.-H., 2000, AJ, 119, 787

Hansen P. C., 2007, Numerical algorithms, 46, 189

Hansen P. C., 2010, Discrete Inverse Problems. Society for Industrial and Applied Mathematics

Holmberg J., Nordström B., Andersen J., 2007, A&A, 475, 519

Howarth I. D., 2011, MNRAS, 418, 1165

Howarth I. D., Siebert K. W., Hussain G. A. J., Prinja R. K., 1997, MNRAS, 284, 265

Huang R. Q., 2004, A&A, 425, 591

Hubeny I., Lanz T., 1995, ApJ, 439, 875

Huber D. et al., 2013, Science, 342, 331

Hunter J. D., 2007, Computing in Science Engineering, 9, 90

Ilin V. B., Ivanov V. V., 1979, Soviet Astronomy Letters, 5, 152

Inc. W. R., 2020, Mathematica, Version 12.1, Champaign, IL

Ivanov V. K., Vasin V. V., Tanana V. P., 01 Jan. 2002, Theory of Linear Ill-Posed Problems and its Applications. De Gruyter, Berlin, Boston

Jackson R. J., Jeffries R. D., 2010, MNRAS, 402, 1380

Jankov S., 1995, Publications de l'Observatoire Astronomique de Beograd, 50, 75

Kaniadakis G., 2002, Phys. Rev. E, 66, 056125

Kaniadakis G., 2005, Phys. Rev. E, 72, 036108

Klinglesmith D. A., Sobieski S., 1970, AJ, 75, 175

Kopal Z., 1950, Harvard College Observatory Circular, 454, 1

Kurucz R. L., 1993, in Astronomical Society of the Pacific Conference Series, Vol. 44, Dworetsky M. M., Castelli F., Faraggiana R., eds, IAU Colloq. 138: Peculiar versus Normal Phenomena in A-type and Related Stars, p. 87

Levenhagen R. S., 2014, ApJ, 797, 29

Levenhagen R. S., Leister N. V., 2006, MNRAS, 371, 252

Lucy L. B., 1974, AJ, 79, 745

Lucy L. B., 1994, Reviews in Modern Astronomy, 7, 31

Maeder A., Meynet G., 2010, New Astronomy Reviews, 54, 32 , Proceedings: A Life With Stars

Meilland A., Millour F., Kanaan S., Stee P., Petrov R., Hofmann K. H., Natta A., Perraut K., 2012, A&A, 538, A110

Mermilliod J. C., Mayor M., Udry S., 2009, A&A, 498, 949

Mihalas D., 1964, ApJ, 140, 885

Natterer F., Wübbeling F., 2001, Mathematical methods in image reconstruction

Neilson H. R., Lester J. B., 2011, A&A, 530, A65

Neilson H. R., Lester J. B., 2012, A&A, 544, A117

Neilson H. R., Lester J. B., 2013, A&A, 554, A98

Neiner C., de Batz B., Cochard F., Floquet M., Mekkas A., Desnoux V., 2011, AJ, 142, 149

Neiner C. et al., 2002, A&A, 388, 899

Nordström B. et al., 2004, A&A, 418, 989

Ochsenbein F., Bauer P., Marcout J., 2000, A&AS, 143, 23

O'Mara B. J., Simpson R. W., 1972, A&A, 19, 167

Orellana R., Escárate P., Curé M., Christen A., Carvajal R., Agüero J. C., 2019, A&A, 623, A138

Parzen E., 1962, Ann. Math. Statist., 33, 1065

Penny L. R., 1996, ApJ, 463, 737

Pérez F., Granger B. E., 2007, Computing in Science and Engineering, 9, 21

Porter J. M., Rivinius T., 2003, PASP, 115, 1153

Ramírez-Agudelo O. H. et al., 2013, A&A, 560, A29

Reiners A., 2003, A&A, 408, 707

Reiners A., Schmitt J. H. M. M., 2002, A&A, 384, 155

Richardson W. H., 1972, Journal of the Optical Society of America (1917-1983), 62, 55

Rivinius T., Carciofi A. C., Martayan C., 2013, A&A Rev., 21, 69

Rosenblatt M., 1956, Ann. Math. Statist., 27, 832

Rowlinson J. S., 2005, Molecular Physics, 103, 2821

Royer F., 2005, Memorie della Societa Astronomica Italiana Supplementi, 8, 124

Russell H. N., 1912a, ApJ, 35, 315

Russell H. N., 1912b, ApJ, 36, 54

Ryans R. S. I., Dufton P. L., Rolleston W. R. J., Lennon D. J., Keenan F. P., Smoker J. V., Lambert D. L., 2002, MNRAS, 336, 577

Scales J., Gersztenkorn A., 1999, Inverse Problems, 4, 1071

Secchi A., 1866, Astronomische Nachrichten, 68, 63

Silverman B., 1986, Density Estimation for Statistics and Data Analysis, Chapman & Hall/CRC Monographs on Statistics & Applied Probability. Taylor & Francis

Simón-Díaz S., Herrero A., 2007, A&A, 468, 1063

Simón-Díaz S., Herrero A., 2014, A&A, 562, A135

Simón-Díaz S., Herrero A., Esteban C., Najarro F., 2006, A&A, 448, 351

Slettebak A., 1956, ApJ, 124, 173

Struve O., 1945, Popular Astronomy, 53, 201

Struve O., 1952, PASP, 67, 117

Sundqvist J. O., Simón-Díaz S., Puls J., Markova N., 2013, A&A, 559, L10

Tikhonov A. N., 1943, Dokl. Akad. Nauk SSSR, 39, 195

Tikhonov A. N., 1963, Sov. Math., Dokl., 5, 1035

Tikhonov A. N., Arsenin V. I., 1977, Solutions of ill-posed problems / Andrey N. Tikhonov and Vasiliy Y. Arsenin ; translation editor, Fritz John. Winston ; distributed solely by Halsted Press Washington : New York, p. xiii, 258 p. :

Tikhonov A. N., Goncharsky A. V., 1987, Ill-posed problems in the natural sciences

Tikhonov A. N., Leonov A. S., Yagola A. G., 1998, Nonlinear ill-posed problems, Vol. 14

van Dien E., 1948, JRASC, 42, 249

Van Rossum G., Drake Jr F. L., 1995, Python tutorial. Centrum voor Wiskunde en Informatica Amsterdam, The Netherlands

Vanzi L. et al., 2012, MNRAS, 424, 2770

Vinicius M. M. F., Zorec J., Leister N. V., Levenhagen R. S., 2006, A&A, 446, 643

Virtanen P. et al., 2020, Nature Methods, 17, 261

Walborn N. R., Barbá R. H., Sewiło M. M., 2013, AJ, 145, 98

Wand M. P., Jones M. C., 1994, Kernel Smoothing, Chapman & Hall/CRC Monographs on Statistics & Applied Probability No. 60. Chapman & Hall, Boca Raton, FL, U.S.

Wes McKinney , 2010, in Stéfan van der Walt , Jarrod Millman , eds, Proceedings of the 9th Python in Science Conference, p. 56

Yudin R. V., 2001, A&A, 368, 912

Zorec J., Frémat Y., Cidale L., 2005, A&A, 441, 235

Zorec J. et al., 2016, A&A, 595, A132